Prototyping Adhesively Bonded Metal-Composite Hybrid Structures for Aircraft Interior Applications.

by

Shuo Xu

A Thesis Submitted in Partial Fulfilment of the Degree of Master of Engineering

Auckland University of Technology

Auckland, New Zealand

November 2021

Supervisor: Dr Marcel Schaefer

Abstract

This research explores the application of adhesively bonded CFRP-aluminium hybrid structure for aircraft interior application. A concept of using an adhesively bonded hybrid structure to replace the original full aluminium structure (fastener joining method) was established. The current structure will be built by 6061 T6 aluminium alloy and the T700 carbon fibre reinforced polymer. The new joining method uses epoxy adhesive to bond them together since the CFRP cannot be welded, and drilling holes will decrease the strength of the parts.

This is the support structure of the air attendant seat used in commercial aircraft. This project requires building a prototype test demonstrator to conduct tensile tests, and the test demonstrator is to simulate the aircraft's air attendant seat’s support structure. The experiment aims to investigate the hybrid structure's performance and further provide development suggestions through the experiments. A total of three test demonstrators were built for conducting the tensile test. Since the build of the test demonstrator was not related to any standard, three demonstrators can enhance the result accuracy. Strain gauges were used to monitor the strain change during the experiments.

The experiment result indicates that the concept is reliable for further research since the aluminium and the CFRP can withstand high loads. The adhesive layer cracked before reaching the minimum design load, but none of the CFRP tubes loosened from the joints after the experiments. The adhesive thickness of the joints was 0.2 mm, and the experiment results showed that the thickness could be further reduced as long as the parts can be bonded in a stable connection. The structure's performance has mainly relied on the parts, not the adhesive. The failure mode of the joints was mainly an adhesive failure that occurs on the aluminium surface, which indicates the surface treatment method of the aluminium needs to improve. The SolidWorks FEA has been applied to the study, and the results suggested the structure deformation pattern and the CFRP tube strain pattern can be used as references. The aluminium strain

simulation failed since the simplified structure cannot simulate the actual setup in the experiments.

This project suggests that future research can be focused on the aluminium parts surface treatment, adhesive layer thickness, and the joint depth for CFRP tubes. The NDT exam method and the suitable parts replacement and maintenance methods should also be researched.

Contents

Attestation of Authorship

I hereby declare that this submission is my own work and that, to the best of my knowledge and belief, it contains no material previously published or written by another person (except where explicitly defined in the acknowledgements), nor material which to a substantial extent has been submitted for the award of any other degree or diploma of a university or other institution of higher learning.

Signature:

Acknowledgements

Thanks to my supervisor, Marcel Schaefer, for his guidance and mentoring. I learned a lot under his supervision. He is always kind to provide suggestions and assistance. I appreciate this research opportunity with him.

Thanks for the assistance from the AUT technicians. They helped me a lot through the project. There is no way I can finish this project without them. And I learnt a lot from them as well.

Thanks to the AIM Altitude for providing such a great research opportunity. And thanks for all the help from the PhD student Ardeshir Saniee.

Thanks for all my family and friends' support during my study. I can't achieve this without their help.

List of Figures

List of Tables

Chapter 1 Introduction

1.1 Project background

This project was a joint program of Auckland University of Technology, University of Auckland, AIM Altitude, funded by the MBIE. AIM Altitude is an aerospace design and manufacturing company focusing on interior aircraft applications. The company focus on not only commercial orders but also military and defence. They widely use composite materials in their designs and products.

The main object of the program is to develop and improve the supporting structure for attendant seats. Figure 1 demonstrates the common air attendant seat. The seat is fixed on the support structure behind the galley wall. Figure 2 shows the attendant seat's installation positions and the attachment's layout. This drawing represents the support structure behind the galley wall. Figure 3 displays the traditional design used in the company, built with full aluminium reinforcements and joints by rivets; the attendant seat is fixed on the aluminium reinforcements directly by fasteners (Maxime, 2019).

Figure 1

The air attendant seats are attached to the gally wall

Figure 2

Cabin attendant seat attachment spacing

Figure 2 is removed due to the figure contain confidential material.

Figure 3

The current full aluminium structure for the attendant seat

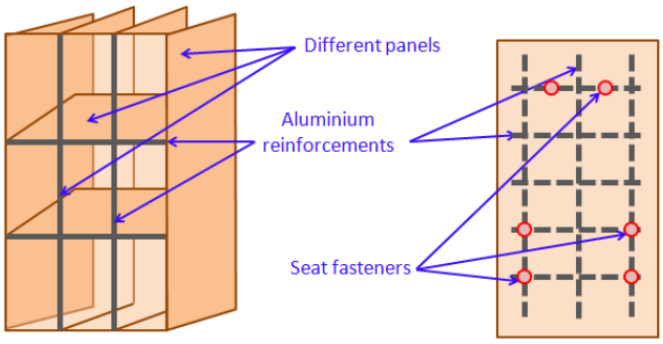

The company wishes to replace the original full aluminium structure with a new metal composite hybrid. The new joint design should have better or equal mechanical properties, lighter weight, and lower cost than the previous model. The new design will use aluminium and carbon-fibre reinforced polymer tubes, joining together by the adhesive bonding method instead of welding or fastening. Adhesive bonding is widely used in the industry and draws the attention of engineers and scientists. The similar material joined together by the adhesive bonding method is well-understood and with

mature testing protocols. But this project involves bonding two dissimilar materials, the CFRP and the aluminium alloy. The dissimilar material adhesive bonding's application in aerospace, automotive and wind energy is increasing these days. But still have lots of challenges in this area of applications. (Loutas et al., 2019)

This project is part of a large program, and the main focus is to design and build a new test demonstrator based on the concept designed by a previous student. The demonstrator structure will be produced by metal and circular composite parts (aluminium alloy and carbon fibre reinforced polymer). The aluminium alloy and CFRP will connect by the adhesive bonding method (using standard industrial grade epoxy glue). The previous project established a concept design of the hybrid structure. The test demonstrator requires more improvement and verification before building the prototype. The project aims to investigate the performance of the new aluminium-CFRP joints of whether the newly designed aluminium-CFRP hybrid joints structure can economically and mechanically outperform the origin aluminium structure design and investigate the flow of the structure.

1.2 Previous design concept

Maxime (2019) established the concept design, as shown in Figure 4. The primary structure was combined by four aluminium joints and twelve CFRP tubes. The four cubic metal joints represent attachment point 1,2,7,8, shown in figure 2. Each aluminium joint contained four holes to join the CFRP tubes and one tap hole to connect with an eyebolt. This concept well describes the shape of the original structure. Four loading points will be set on the four aluminium joints, representing points 1,2,7 and 8 in figure 2.

Figure 4

The previous concept design of the adhesively bonded aluminium-CFRP hybrid structure

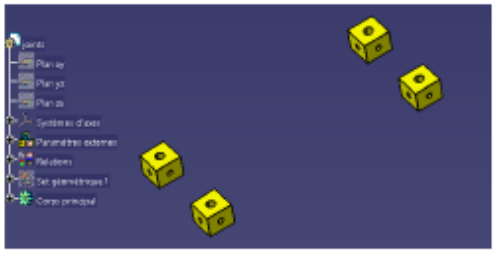

(a) Aluminium joins

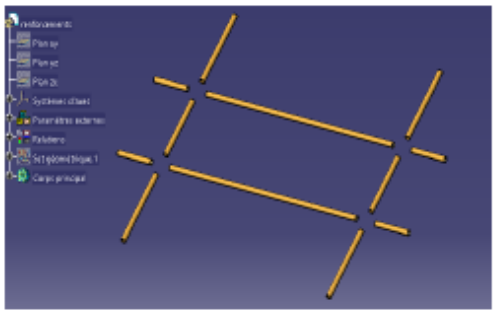

(b) CFRP reinforcements

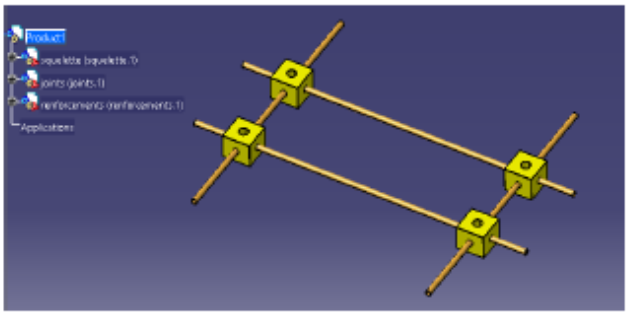

(c) Assembly

Figure 5 illustrates the completed test demonstrator. Four eyebolts and one paper panel will connect the aluminium-CFRP hybrid structure. The test load will apply to those four eyebolts directly. And the paper panel was to simulate the surface panel of the galley wall. The paper panel used in this project is the same as the company used in the real aircraft; the paper panel has a honeycomb structure.

Figure 5

The complete concept setup of the test demonstrator

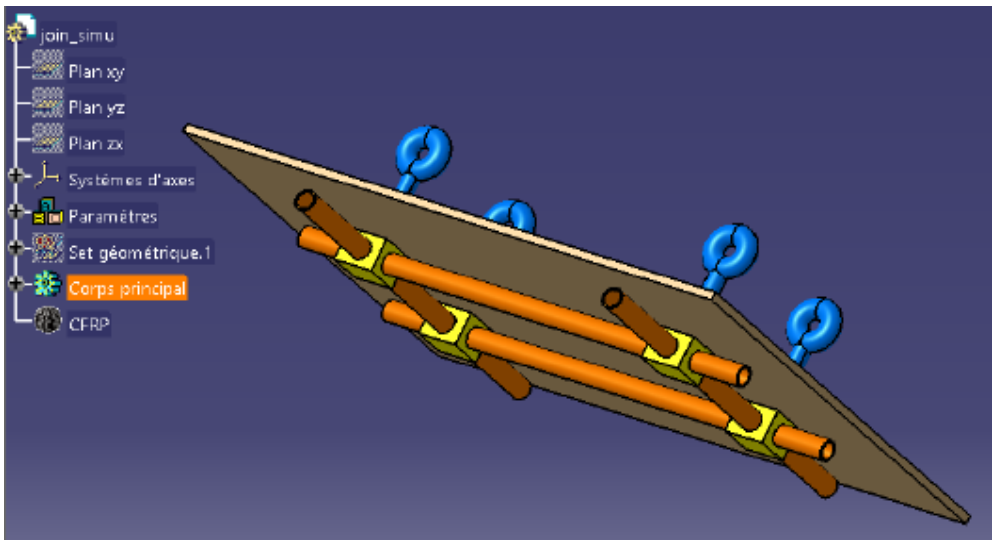

Figure 6 demonstrates a complex full test structure concept developed by Maxime. Eight CFRP tubes are connected with eight L-shaped joints. These joints were bolted on an intermediate plate bolted on the test platform by four C-shaped joints. The hybrid joints must withstand at least 14323.3 N.

Figure 6

The completed test structure concept

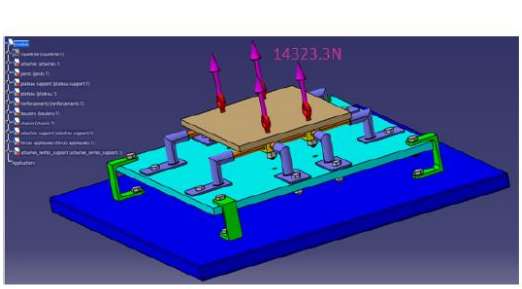

(a) Face view

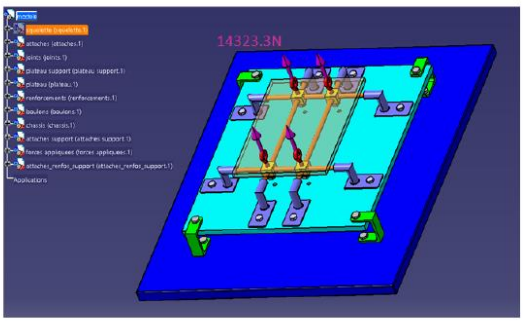

(b) Top view

Figure 7 shows a refined concept that is shown in figure 4. The intermediate plate was removed to save cost and simplify the final test structure.

Figure 7

The final test structure concept

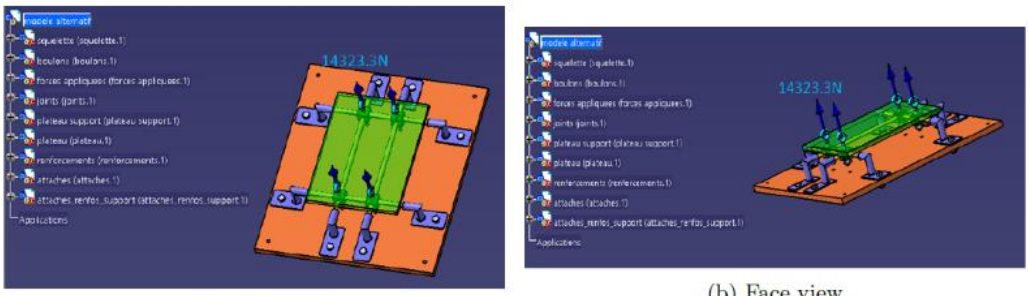

(a) Top view

(b) Face view

The initial concept well represents the company's original design. The majority of the structure will stay unchanged. So, only the parts size and detailed design will be changed during this project. But the test plan and final test full assembly are too complicated and hard to achieve in reality. In Figure 5, When loads apply to the four eyebolts, only the eight short CFRP tubes and joints around the test samples will undertake loads. So, the test method won't fit the joint's design purpose. The final test structure plans in figure 6 and figure 7 are complicated. Even the final concept simplified the overall structure, but the holding parts are hard to manufacture. Therefore, the test plan and final test layout will be redesigned (Chapter 3 explains the detailed analysis).

1.3 Research objectives

As mentioned in chapter 1.1, this project will focus on building a new test demonstrator and conducting physical pull-out tests for the demonstrator. Three identical test demonstrators will be produced to increase the test's accuracy and reduce the error.

Four steps are required before building the test demonstrators.

1. The validation process for the previous concept. The CFRP tubes and aluminium joints' dimensions need to be re-checked. The re-checked contents include the demonstrator's dimension and parts design.
2. Refine the test demonstrator if possible.
3. Re-develop the test method and structure layout to conduct the physical test better. The previous test method is too complex to execute.
4. Select or build a suitable test platform.

The four steps are re-checking the previous design and refining the concept to better fit into the actual testing environment.

In general, the research objectives of this project are:

1. Physically built three demonstrators and conducted tensile tests.
2. Investigate the adhesively bonded hybrid structure's performance and whether worth continuing development.
3. Observe the structure behaviour after the tests.
4. Identified the joints' failure mode of the bonded joints section.
5. To make further development suggestions based on the experiment results.

Figure 8 shows the test platform layout, including the test frame, actuator, and data acquisition setup (controller). Clear protectors were placed between the test platform and the controller.

Figure 8

Test platform layout and experiment setup

Chapter 2 Literature review

The adhesive bonding method has a long-recorded history. Plywood has been using the adhesive bonding method since 1905, but the earliest wood layer bonding could track back to 3500 B.C. Wood was joined by using animal glue (Kalpakjian, 2001). The first large-scale adhesive-bonding application in manufacturing aircraft's load-bearing parts was in World War II (Kalpakjian, 2001). The adhesive bonding method is developed in aircraft manufacturing and continues to develop in other engineering fields, such as marine, aerospace, vehicles, military, wind energy and infrastructure industries (B.Mikhail, 2009).

2.1 Aluminium and CFRP

Aluminium alloy components and carbon fibre parts are the primary material in this project. Aluminium alloy has a relatively low density and a better corrosion resistance than steel (E.M. Petrie, 2007). It is widely used in industries such as aerodynamics and marine application. Carbon-fibre composite is a polymer matrix composite. CFRP is the most commonly used high-performance fibre material in non-fibreglass polymer-matrix composites. It has high strength, moduli, and high-temperature oxidation; the elevated temperature will not easily influence its mechanical properties; it has excellent moisture and chemical resistance at room temperature (E.M. Petrie, 2007). CFRP is not a homogenous material since its mechanical properties depend on fibre orientation (Hassan, 2018). CFRP materials have higher strength along the longitudinal axis (X-axis) than aluminium alloy. Sanders (2001) states

The aluminium used in this project is 6061 T6 alloy, widely used in aircraft, yachts, and other vehicle applications. It was first developed in 1935 and named ''Alloy 61S'' (Stephen, 1993). Sanders (2001) states the 6061 alloy is a precipitation-hardened material and the major alloying elements are silicon and magnesium. This alloy has a good mechanical performance and good weldability. The composite tubes' material will use T700 laminates. This composite material has high specific strength and better

performance during different temperature environments (Wei, 2015). It is widely used in the weight reduction of aircraft applications (Schwartz, 1997). Table 1 displays the T700 CFRP's strength properties (Hassan, 2018). Table 2 displays the T6061-T6 aluminium alloy's strength properties (Hsu, 2016). The CFRP's mechanical properties along its longitudinal axis are far higher than T6061-T6 aluminium alloy. The tensile stress is seven times higher, and the compression stress is three times higher. But the weight of CFRP is only 56.4% of T6061-T6. The application of the hybrid structure can reduce the total weight. The CFRP's cost is higher than aluminium. But the total cost can be reduced because it requires less material to achieve the loading requirements when applied in the right direction. Therefore, the aluminium-CFRP hybrid structure can reduce weight and cost but maintain the required loading ability. Boyd (2004) stated an adhesively bonded hybrid structure application in a French warship. The primary purpose of using an adhesive-bonded hybrid structure is to reduce the total weight of the hull armour and structure and increase the loading capacity.

Table 1

T-700 CFRP properties (Hassan, 2018)

Property	Value
Fibre volume fraction (%)	60.2±1.5
Denisty (kg/m^3)	1570
Orthotropic Elasticity	
Young Modulus X (GPa)	132
Young Modulus Y (GPa)	10.3
Young Modulus Z (GPa)	10.3
Poisson's Ratio XY (GPa)	0.25
Poisson's Ratio YZ (GPa)	0.38
Poisson's Ratio XZ (GPa)	0.25
Shear Modulus XY (GPa)	6.5
Shear Modulus YZ (GPa)	3.91
Shear Modulus XZ (GPa)	6.5
Orthotropic Stress Limits	
Tensile Stress X (MPa)	2100
Tensile Stress Y (MPa)	24
Tensile Stress Z (MPa)	65
Compression Stress X (MPa)	1050
Compression Stress Y (MPa)	132
Compression Stress Z (MPa)	132
Shear Stress X (MPa)	75
Shear Stress Y (MPa)	75
Shear Stress Z (MPa)	75

Table 2

T6061-T6 aluminium alloy properties (Hsu, 2016)

Properties	Value
Young's modulus	68.9 GPa
Poisson's ratio	0.33
Mass density	2784 Kg/m^3
Static yield stress	300 MPa

2.2 Joining method

According to the American Welding Society (AWS), the typical engineering joining methods can divide into three major categories, welding, mechanical fastening, and adhesive bonding (Kalpakjian, 2001). Mechanical fastening involves fasteners applications such as using rivets, bolts and nuts. Welding is normally classified into three types: Fusion welding, solid-state welding, Brazing and Soldering. Adhesive bonding has an excellent stress distribution and could use for thin parts joining and dissimilar materials. The fastening method has good repairability. Welding has superior strength to adhesive bonding (Petrie, 2007). The adhesive-bonding joining method uses a filler material (such as rubber or polymer) between two surfaces (Wegmanand, 2012). The mechanical fastening joining method needs to create holes to perform. These holes reduce the strength of the materials and introduce stress concentration; the fastening way can damage the composite materials' laminar structure (Petrie, 2007). Mechanical fastening is not an ideal joining method for this project. And the geometry of the concept design indicates mechanical fastening is not appropriate. Welding has excellent strength performance compared to adhesive bonding. Abdullah et al. (2012) tested steel welded and adhesive bonded T-joints. Figure 9 shows the experimental results that the weld joints between steel are eight times stronger than the adhesive bonding joint method (epoxy adhesive). But the experiment is done under the same material joints. Dissimilar welding still faces many challenges and is already widely applied in the industrial area.

Figure 9

Adhesive joints and weld strength of steel T-joints (Abdullah et al. 2012)

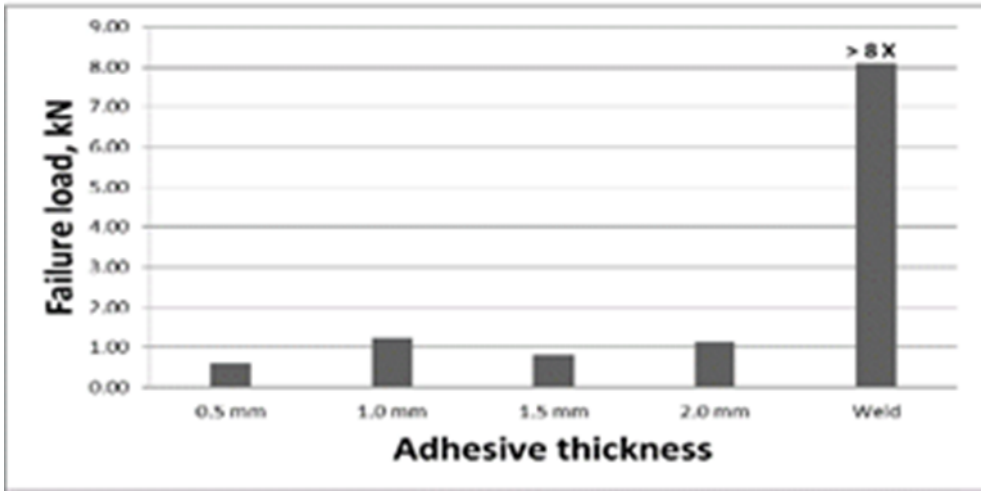

According to Nguyen et al. (2017), they successfully welded (TIG welding) the 304 stainless steel and A6061 aluminium alloy. But the conditions to achieve this are harsh, and the process is quite strict. Many factors must be well researched for each application, or it can lead to failure. Another disadvantage of applying dissimilar welding to this research is the two primary materials' weldability is weak. The traditional welding process cannot weld the carbon fibre since the carbon is hard to melt, and welding can weaken the strength of the aluminium and other light metals such as titanium and magnesium (Petrie, 2007). Dawei et al. (2018) improved welding and resistance welding can join CFRP and metal materials. Figure 10 demonstrates one of the samples. A thin layer of metal covers the CFRP before the welding process. Titanium and zirconium often act as the brazing filler. The CFRR-metal joining usually adopts vacuum brazing as a joining method. But the cost of brazing is expensive. Melting metals require excessive heat, and the joints typically result in irregular stress distribution (Dawei et al., 2018). Resistance welding, induction heated joining, and ultrasonic welding can manufacture aluminium and CFRP joints (Dawei et al., 2018). But most successful experiments that successfully welded CFRP and Aluminium used sheet metal. And the equipment and material costs are high.

Figure 10

Brazing of CFRP and titanium or niobium alloy (Dawei et al. 2018)

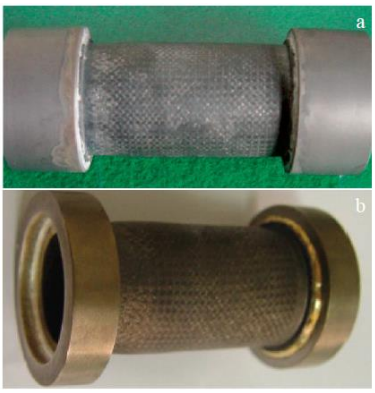

Balle et al. (2011) successfully welded aluminium sheets with CFRP using ultrasonic welding. Figure 11 displays the ultrasonic spot-welding system and the specimen used. A layer of adhesive between the aluminium and the CFRP sheets is required to conduct welding. The welding process melts the adhesive layer and bonds the CFRP and aluminium sheets. The ultrasonic spot weld was used in this application, but the process is still similar to adhesive bonding with high-end tools. And this system does not suitable for larger and thicker parts rather than thin sheets.

Figure 11

Ultrasonic welding and its specimen (Balle et al. 2011)

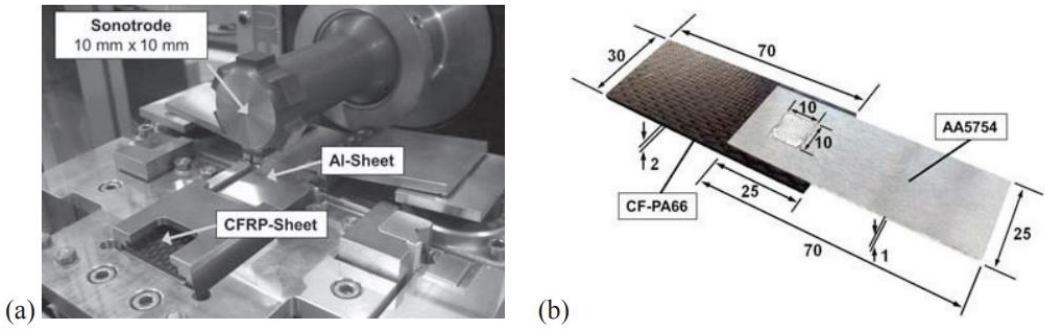

. 1. (a) Advanced ultrasonic spot welding system (b) Specimen geometry for Al/CFRP-joints

Note. (a) Advanced ultrasonic spot-welding system. (b) Aluminium-CFRP joints specimen.

Figure 12 shows the laser beam joining method that joined the aluminium sheet and CFRP with titanium wire loops (Woizeschke et al., 2013). The equipment and process are expensive and complicated. Before joining, the titanium wire loops had to be planted into the aluminium sheet. Then enlaced the titanium wire loop with carbon fibre roving. The last step is installing the structure with resin. Evolving this technology means more costs on buying equipment and training or hiring new employees. And it is mainly focused on joining CFRP with sheet aluminium metal at this stage.

Figure 12

Laser beam application of joining aluminium sheet and CFRP with titanium wire loops (Woizeschke et al. 2013)

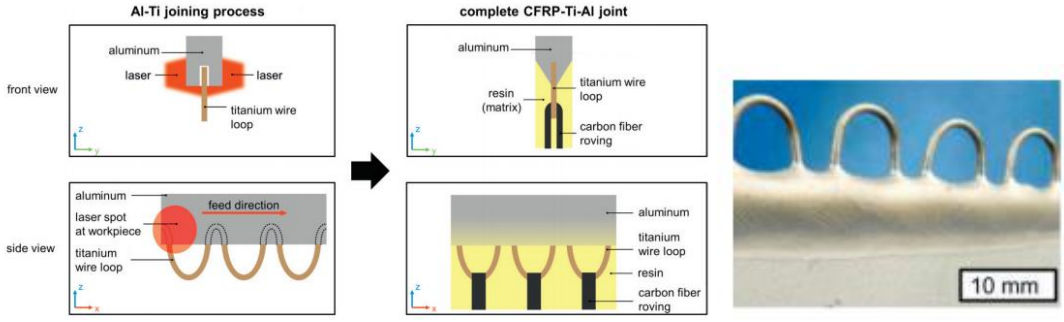

(a) (b)

Note. (a) The joining processes. (b) The titanium wire loop's concept drawing.

One of the essential purposes of this research is to reduce costs. Buying new equipment and bringing new complex technology would significantly increase the budget, and more training for workers or experienced labours is required. The overall cost will increase. Adhesive bonding's price would be less high than the welding and fastening method. Its manufacturing steps require less procedure than a fastening joining. It also has a better fatigue strength than the riveted joint (Petrie, 2007). Figure 13 displays a fatigue chart of adhesive joints and riveted joints. The chart indicates the adhesive-bonded structure of aluminium alloy has a better fatigue strength under shear load (Petrie, 2007). Galvez et al. (2017) used adhesive joints to improve the bus structure's fatigue ability. The adhesive bonding method has a unique advantage over the other two primary joining methods (welding and fastening), but it also has some

challenges at the moment. Loutas et al. (2019) described that similar material adhesive joining is well-understood with mature test protocols. However, the dissimilar joining is still under challenges such as geometrical and residual thermal stresses.

Figure 13

Fatigue chart of adhesive joints and riveted joints (Petrie, 2007)

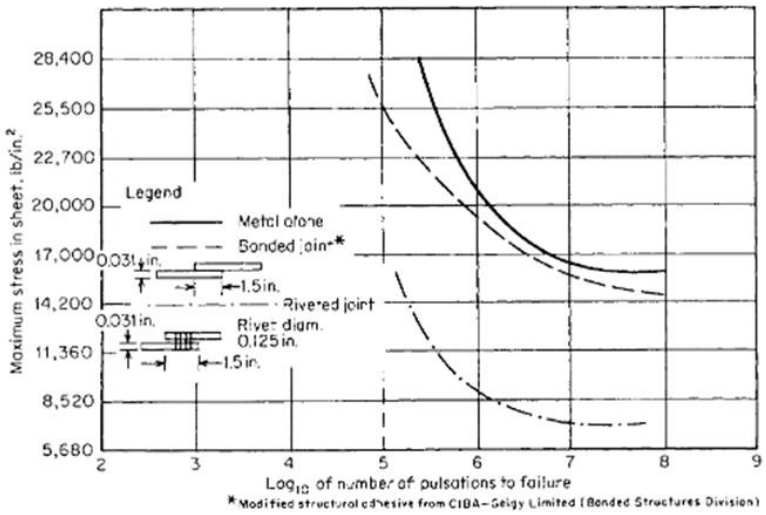

2.3 Application

Composite-metal adhesive-bonded is a typical application of hybrid structure in civil and construction. David et al. (2007) used high modulus CFRP strips to reinforce the steel structure. The CFRP strip has strong mechanical properties, and its tensile modulus is twice of steel. The application of adhesively bonded CFRP could provide better structural stiffness and to further reduce the deflection. The thickness of the CFRP can be minimized and provide an economical upgrade to avoid reconstruction and mass modification. This project used the adhesive bonding method to join the CFRP strips and the steel structure beam. Surface preparation is essential to the adhesive bonding method since an unsuitable preparation method can significantly influence the bonding strength. The surface preparation method must be well researched before making samples. In David et al. (2007)'s project, grit blasting was the surface treatment for steel structure surface preparation and peel-ply for CFRP strips, and it is one of the most common surface treatment processes in metal surface treatment. Figure 14 demonstrates the steel structure's surface preparation and adhesive bonding processes. Figure 14 (a) shows that the technician used a handheld blasting device with PPEs. In figure 14 (b), clamps were used in the adhesive bonding process to ensure the CFRP strips were successfully attached to the steel structure before the adhesive was fully cured.

Figure 14

The surface treatment and the adhesive bonding process (David et al. 2007)

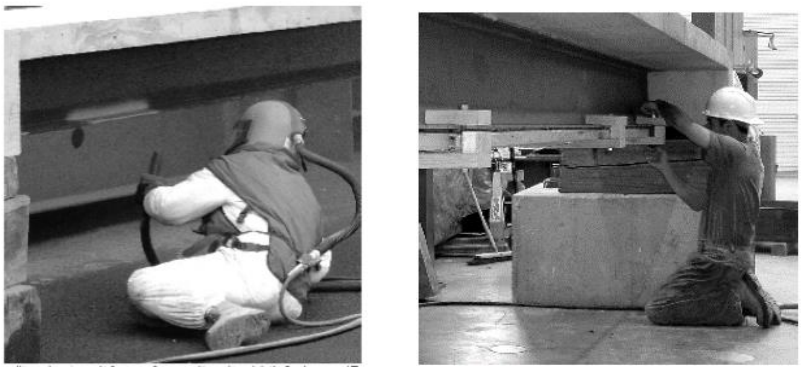

(a) (b)

Note. (a) Grit blasting process. (b) The CFRP strips were bonding to the steel structure.

Boyd et al. (2004) state the French Navy uses a hybrid structure for helicopter hangers. The hybrid structure was built with FRP panels, balsawood, and steel. Figure 15 shows the hanger of the French navy frigate, the hybrid structure's position, and its structural layout. The hybrid structure was located at the side of the helicopter hanger's panel and was joined to the weather deck by the steel reinforcement. The steel reinforcement is directly bonded with the FRP hard composite panels. It did not penetrate the fabric too far since the more extended penetration can cause higher stress concentration. The primary purpose of the adhesive-bonded hybrid structure is to reduce weight and manufacturing process.

Figure 15

The French frigate's helicopter hanger and the hybrid structure hanger (Boyd et al. 2004)

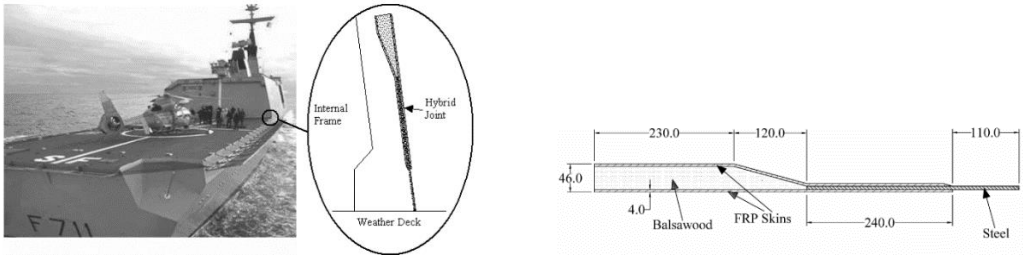

(a) (b)

Note. (a) Frigate helicopter hanger. (b) The adhesively bonded hybrid structure geometry.

Galvez et al. (2017) illustrate research that used the adhesively bonded metal-composite structure to improve the bus frame's fatigue life. This hybrid joint aims to enhance the fatigue life of the structure; the rigidity of the common welding method makes the steel structure have a low fatigue life cycle. Figure 16 (a) identified the crack location of the bus frame. Cracks appeared near the rear door. The welding has a stronger strength than adhesive bonding, but the fatigue life is lower than adhesive joints (Petrie, 2007). Figure 16 (b) demonstrates the new adhesively bonded hybrid structure. The steel frame discarded welding in its high fatigue risk part and adopted

adhesive bonding. The CFRP joints were bonded to the joining section of two steel parts. This structure has a higher elasticity to reduce rigidity and minimize fatigue.

Figure 16

The bus frame and the new design drawings (Galvez et al. 2017)

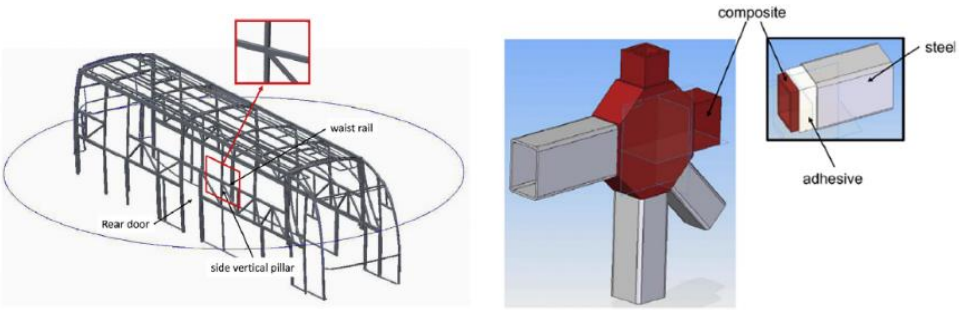

(a) (b)

Note. (a)The adhesively bonded hybrid structure will replace the bus frame and the section. (b) The CAD joining of the new hybrid structure in research.

James (2019) demonstrates a recent injection bonding technique to join CFRP with a metal frame, mainly used in the automobile industry (Figure 17). This technique is similar to the research from Galvez et al. (2017). The adhesive used for this technique is the polyurethane-based adhesive. Its high modulus provides good stiffness, and the high elongation provides good energy absorption and flexibility; these properties can easily manage linear thermal expansion. The adhesive bonding method can also reduce the chance of making a hole on the components that can cause unstable laminate and reduce strength further; adhesive bonding can also reduce the process and cost to seal the hole to prevent them from corrosion (James, 2019).

Figure 17

A recent injection bonding technique to join CFRP with a metal frame (James, 2019)

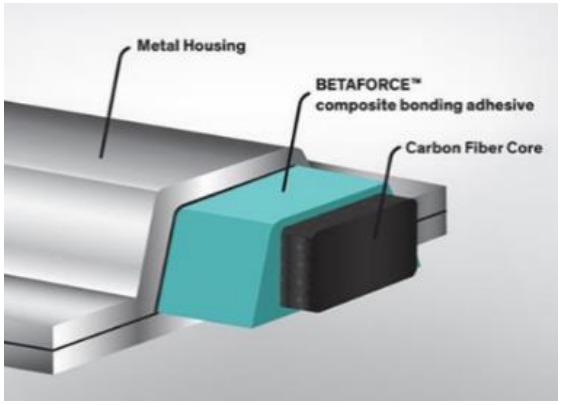

The application examples of the adhesively bonded hybrid structures are widely used in various engineering industries such as civil, marine and transport. The main purpose of using adhesively bonded hybrid structures is to improve mechanical performance, enhance fatigue life, and reduce weight and manufacturing processes.

2.4 Adhesive bonding test method

In this project, the test demonstrator will undergo a physical pulling test. The purpose is to investigate the test demonstrator's actual performance. This section introduced some basic testing techniques.

Figure 18 (a) illustrates a system described by the ASTM D897 standard (Mikhail, 2009). Two parts join together by the adhesive and use tensile tests to examine the sample. This test aims to determine the optimum adhesive thickness in a particular application and the practical value of the adhesion. Figure 18 (b) displays another similar test structure, the butt joint (Mikhail, 2009). It is based on standard ASTM D2094. The bonding face of the rods must be machined to avoid burrs that may affect the adhesive layer. But lots of reports showed this method is not reliable. The stress distribution in the adhesive is not uniform, and most failures usually occur at the centre. The failure is most likely cost by the edge effect, not the tensile load (Mikhail, 2009). This joint type is rarely used for evaluating adhesive, and the sample preparation is more complicated than the single-lap joint.

Figure 18

Two standard adhesive test specimens (Mikhail, 2009)

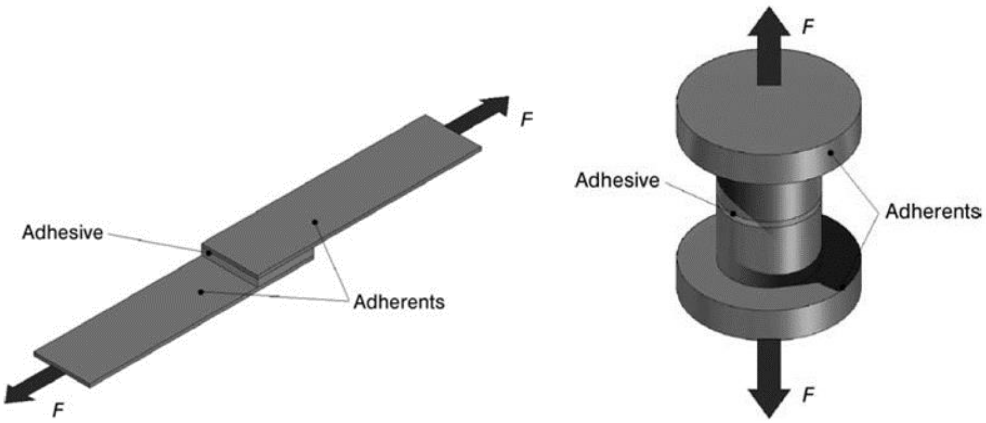

(a) (b)

Note. (a) Single-lap adhesive joints. (b) Butt adhesive joints.

The tensile test will be the primary method to test this project's mechanical properties of the aluminium-CFRP joints. Davis et al. (2004) state that tensile testing is the fundamental engineering test method and material science test method. The testing samples will test under tensile load until they fail. The tensile testing could provide materials' ultimate tensile strength, elongation, breaking strength, and reduction in area. The universal testing machine is the most common device used in the market. The machine uses two crossheads; one for fixing the testing samples and length adjustment, and the other for applying a tensile force to the sample. These machines usually drive with hydraulic power or electromagnetically power. Figure 19 (a) shows a standard tensile test machine (Industrial Heating, 2002). The test demonstrator can not fit into this kind of test machine. A larger test platform or machine will be required. Figure 19 (b) demonstrates a test platform used for a large-scale structure, and this test platform is used by Xi'an Jiaotong-Liverpool University (Popwil, n.d.). A huge actuator was attached at the centre of the test frame, which can conduct the tensile test for oversized structures. A similar and less complicated test platform can be prepared to conduct the static loading test.

Figure 19

Testing machine and facility

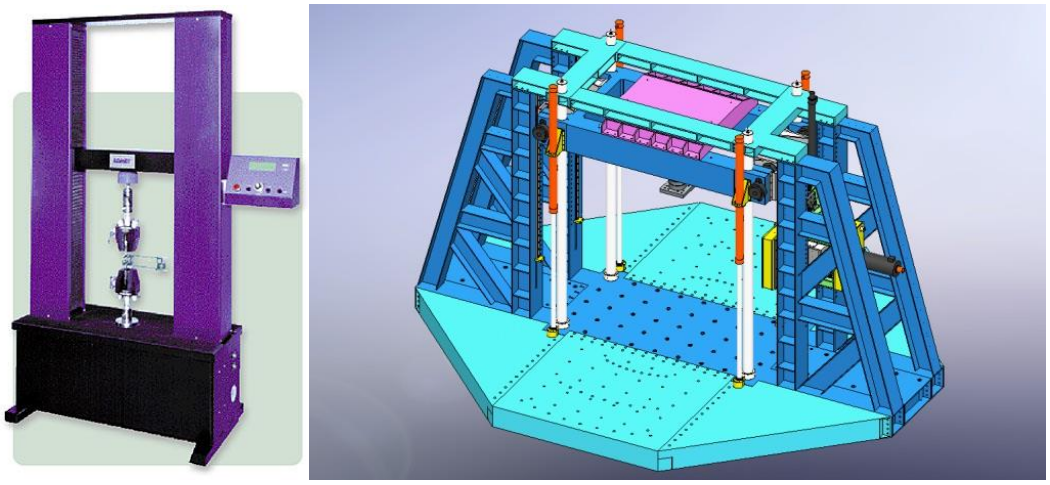

(a) (b)

Note. (a) The standard tensile test machine (Industrial Heating, 2002). (b) The 3D drawing of a large-scale test platform(Popwil, n.d.).

2.5 Optimal adhesive layer thickness for Epoxy type

Adhesive layer thickness is important to the bonded joint's strength, influencing the bonding strength and the joints' mechanical properties (Arenas et al., 2010). Therefore, finding the right adhesive thickness is important to this research.

The adhesive thickness is usually from 0.05 to 0.2mm; the general applications typically are 0.1 mm (Kalpakjian, 2001; Petrie, 2007). But the different adhesives (liquid, paste, solution, powder, emulsion, and film) and different designs can influence the actual thickness. Figure 8 displays the result of four adhesive layer thicknesses under loading tests (Abdullah et al., 2013). The results indicate that 1 mm thickness has the best loading capacity among the other three thicknesses (0.5 mm, 1.5 mm, and 2 mm). Therefore, the thickness of the adhesive layer is important to the bonded joint structure. The adhesive layer thickness to its loading capacity is not linear, and any existing formula can not calculate the results (Alner et al., 1965). So, the optical thickness will rely on experiment results and other study materials.

The epoxy-type adhesive will be used in this experiment, and the adhesive thickness will be based on the following research results.

Figure 20 illustrates an experiment investigating the epoxy adhesive's optimal thickness when bonded with an aluminium alloy (Kahraman et al. 2008). This project investigated the mechanical performance of the aluminium single lap joints with two-part epoxy adhesive. The range of thickness was from 0.03 mm to 1.3 mm. The result shows that the 0.2 mm thickness has the highest strength, around 23 MPa.

Figure 20

Adhesive joint strength under different layer thicknesses (Kahraman et al. 2008)

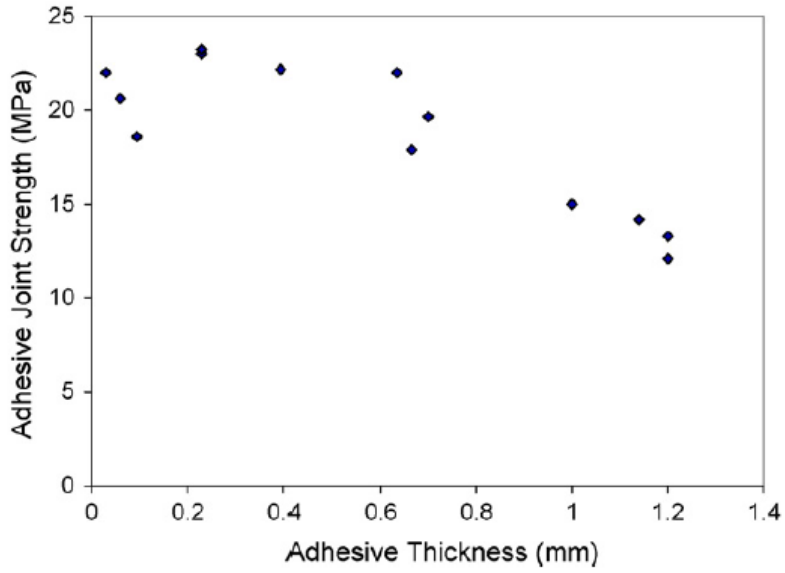

Figure 21 shows another group of epoxy-based adhesive thickness tests (Carlberger et al., 2010). This experiment tested the epoxy adhesive layer thickness from 0.1 mm to 1.6 mm. And the result indicates the 0.2 mm layer thickness has the best performance among all the others. It withstands the highest stress.

Figure 21

Adhesive joint strength under different layer thicknesses (Carlberger et al. 2010)

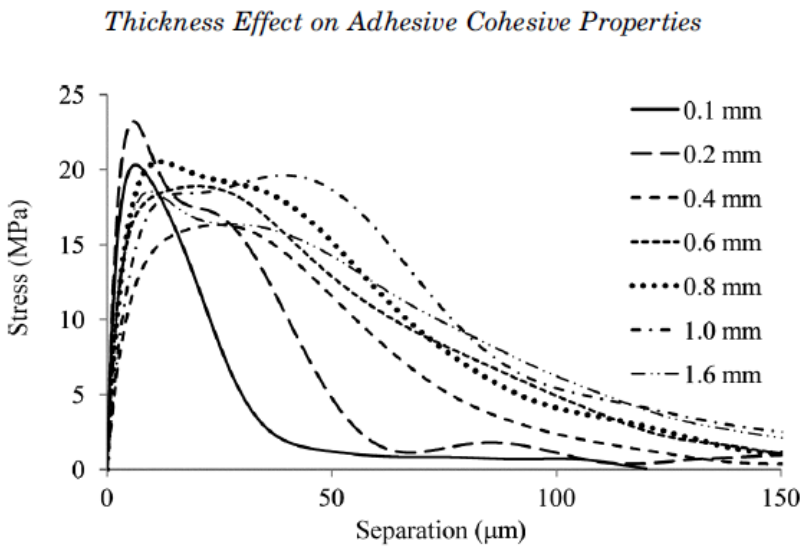

Figure 22 demonstrates an adhesively bonded hybrid structure of aluminium and CFRP (Imanaka et al., 2018). The adhesive used for this joint was the epoxy type, and the adhesive layer thickness applied to this joint was 0.2 mm. In another study by Brandtner-Hafner et al. (2019), 0.2 mm adhesive layer thickness was selected for a similar adhesive bonding test for the aluminium block.

Figure 22

An adhesively bonded aluminium-CFRP hybrid structure joint (Imanaka et al. 2018)

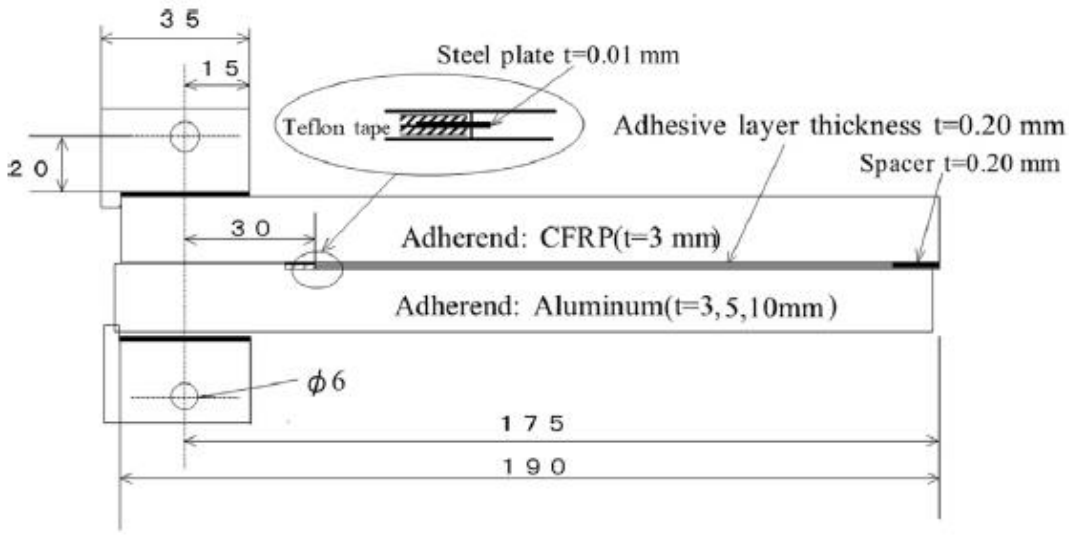

Figure 23 shows a research result of epoxy adhesive performance with different thickness layers (Huntsman Corporation, 2007). The strength of the joints started to drop from 0.4 mm to 1 mm. The optimal layer thickness is around 0.2 mm.

Figure 23

Experiments results of the epoxy adhesive under different thicknesses (Huntsman Corporation, 2007)

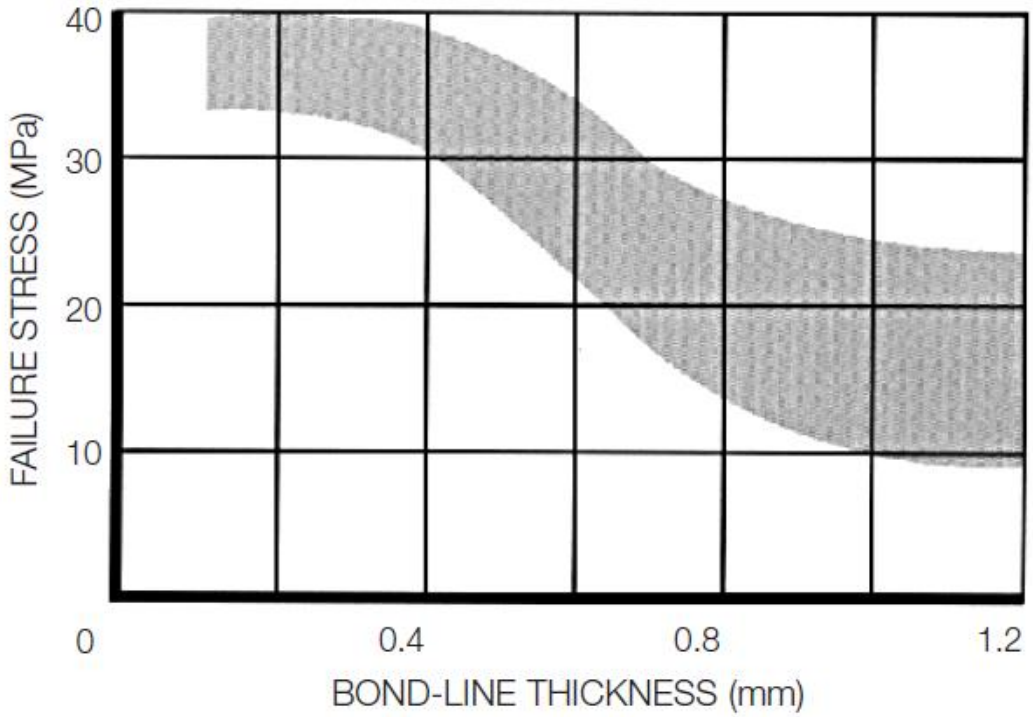

Epoxy adhesive will be used during this project. Multiple research had been studied to better design the adhesive layer thickness in the test structure. A total of four epoxy adhesive research papers indicated that 0.2 mm is the optimal thickness for the epoxy adhesive layer. Therefore, the adhesive thickness for the test structure will be 0.2 mm.

2.6 Adhesive failure mode

Figure 24 demonstrates an adhesion bond and the three most common types of adhesive failure mode (Ebnesajjad et al., 2014). The first failure mode (a) is the adhesive failure. The second failure mode (b) is the cohesive failure in the adhesive layer. And the third failure mode (c) is the cohesive failure that occurs in the adherend. The adhesive failure mode occurs at the joining section of the adhesive and one of the adherents, and it is an interfacial bond failure between them. The cohesive failure mode occurs at the adhesive layer representing the layer failed to remain bonded with each other, but the adhesive remains covered on the adherends' surface. The cohesive failure in the adherend occurs at the adherents, but the adhesive remains bonded with all the adherents.

Figure 24

An example specimen with three common adhesive failure modes (Ebnesajjad et al. 2014)

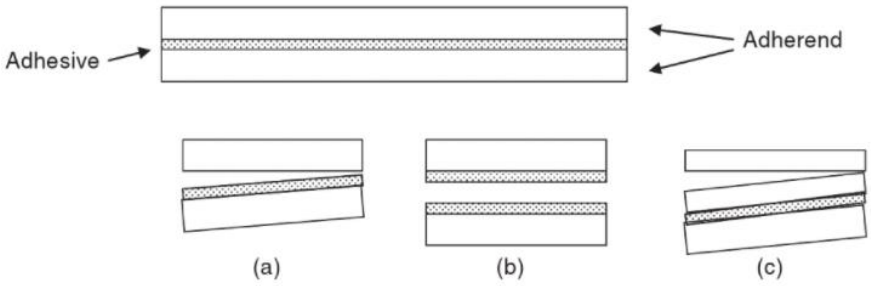

Mittal (2012) states that failure often happens in a mixed mode, which means more than one failure mode might occur simultaneously. The mixed mode is usually described in percentage; for example, 70% cohesive failure and 30% adhesive failure. This percentage is determined by the area percentage of the failure modes that occurs on the same surface. The failure mode determination is an important process for the design development process. This action improves the joints' structure and further saves budget and time. The failure mode with a 100% cohesive failure is the ideal mode, representing that the joint has reached its maximum strength. Some joints' combinations may fail with adhesive failure mode, but these joints may perform better

than a similar structure with a weaker adhesive than a cohesive failure mode. The joints' performance is more critical to the adhesive failure mode. But it is still important to determine whether the failure was caused by improper surface treatment of a weak adhesive bonding (Ebnesajjad et al., 2014).

2.7 FEA application

FEA is getting more popular and common in the engineering industries. It can help engineers and scientists accelerate their research and provide more references. But its reliability is not always robust and reliable. Hsu et al. (2014) used ANSYS to analyse adhesive bonded single-lap joint stress distribution. The ANSYS simulation is robust for single-lap joint stress distribution simulation and non-linear failure with different materials based on the research results. De Moura et al. (2013) used SolidWorks and ABAQUS to simulate the adhesive joints. SolidWorks cannot direct the simulation of the adhesive joints. The SolidWorks' Spring Connector Function was used to simulate the adhesive joining section. And the results are acceptable according to the research conclusion. FEA method can be considered in the later stage before conducting the actual experiments.

2.8 Strain gauge application

Beer et al. (2015) state that deformation is an important factor commonly used in engineering design and analysis. And the amount of deformation material experienced due to an applied force is called strain (NI,2020). Figure 25 shows a concept figure of the strain. The strain is a ratio of material deformation under loading to its original material length (Ling et al., 2021). Equation 2.8.1 introduce the strain's relation to the deformation and the original material length (Beer et al., 2015)

Equation 1 (2.8.1)

$$\epsilon = \frac{\Delta L}{L}$$

Figure 25

The strain is a ratio of deformation of the material under loading to its original material length. (NI,2020)

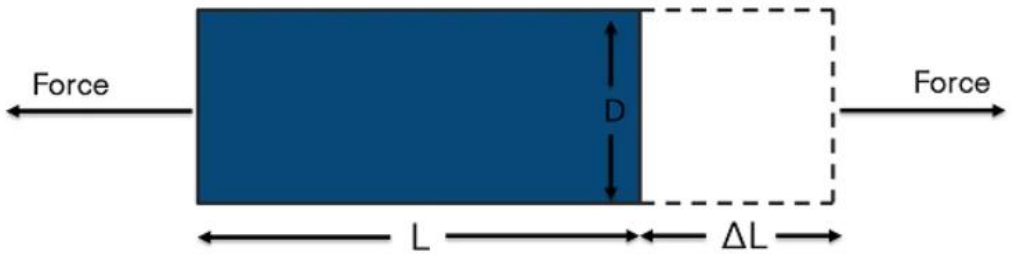

The strain has to be monitored during the experiments further to analyse the test demonstrator's performance and behaviour. An electric sensor can be used to help to monitor the strain, which is called a strain gauge. Lord Kelvin first found that the electrical conductor can make resistance change when stretched, and then Edward Simmons and Professor Arthur C. Ruge developed the first wired strain gauge (Window et al. 1982). Figure 26 demonstrates the basic diagram of the wire resistance type strain gauge (Bolton, 2015). The wire resistance strain gauge is assembled by the metal wire, metal foil, and semiconductor placed on a thin film.

Figure 26

The electrical resistance strain gauges' parts diagrams (Bolton, 2015)

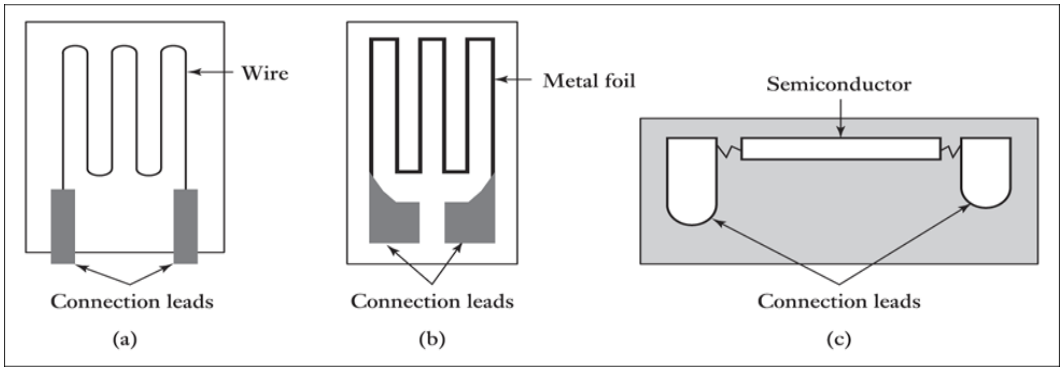

Note. (a) Strain gauge's metal wire. (b) Strain gauge's metal foil. (C) Strain gauge's semiconductor.

The electrical resistance strain gauge can detect the strain change by monitoring its resistance change, and the strain is a ratio of change in resistance to its original resistance (Bolton, 2015). Equation 2.8.2 describe the strain-resistance relationship, and the G in the equation is the constant of proportionality, normally called a gauge factor.

Equation 2 (2.8.2)

$$\in = \frac{\Delta \mathrm{R}}{RG}$$

Figure 27 displays a circuit diagram of the Wheatstone bridge circuit (Karuppasamy et al., 2019). This circuit can measure the unknown electrical resistance with high sensitivity (Stout, 1960). This bridge circuit was invented by Samuel Hunter Christie in 1833 and subsequently improved by Sir Charles Wheatstone in 1843, and it is popularly known as the Wheatstone bridge (Karuppasamy et al. 2019). The Wheatstone bridge is being used wildly in industry and research applications. It can be plugged into the computer through a multichannel system to transmit and store large quantities of data (Karuppasamy et al., 2019).

Figure 27

Standard Wheatstone bridge circuit diagram (Karuppasamy et al. 2019)

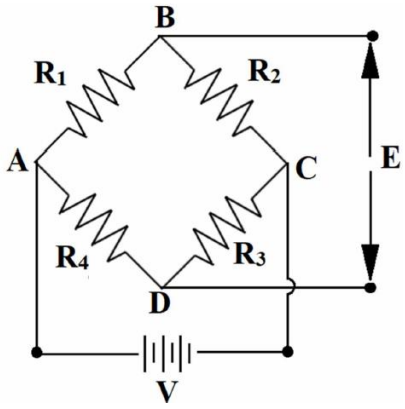

There is three main strain gauge configuration in the current applications, the quarter bridge configuration, the half-bridge configuration, and the full-bridge configuration.

Figure 28 demonstrates the basic structure of the quarter bridge configuration I (Karuppasamy et al., 2019). One of the resistance arms is replaced by an active strain gauge. This configuration can measure both bending and axial strain change of the part. This configuration has a major disadvantage: its accuracy can be affected by the temperature. This configuration should be avoided use in a place with significant temperature change. Figure 29 shows a way to eliminate the temperature effect, which is to attach a dummy strain gauge, and this is the quarter bridge configuration II (Karuppasamy et al. 2019). The dummy strain gauge will not bond to the test samples. The resistance ratio can eliminate the active and dummy strain gauge experienced with the same temperature and temperature.

Figure 28

Standard quarter bridge configuration I (Karuppasamy et al. 2019)

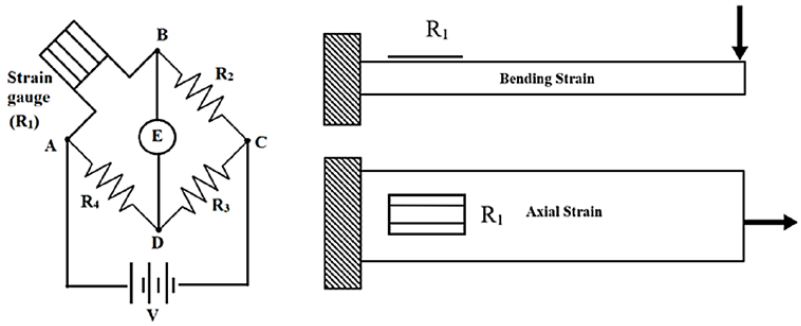

Figure 29

Standard quarter bridge configuration II (Karuppasamy et al. 2019)

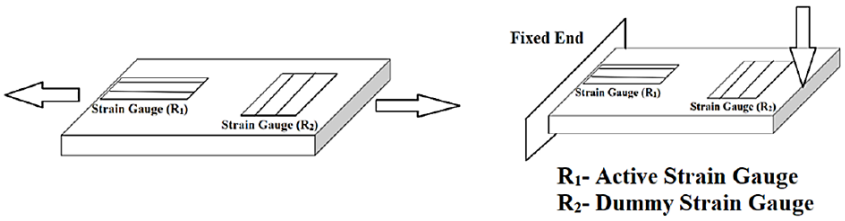

Figure 30 shows a basic configuration of the half-bridge circuit (Configuration 1) (Karuppasamy et al. 2019). This configuration uses two active strain gauges, and they are placed at the top and the bottom of the test sample. It can only measure bending strain. Each strain gauge can read one measurement of the tensile or compressive strain. The top strain gauge R1 reads the tensile strain, and the R2 reads the compressive strain (Karuppasamy et al., 2019). Figure 31 demonstrates another configuration of the half-bridge circuit (configuration II) (Karuppasamy et al., 2019). This configuration looks like the quarter bridge setup in figure 29. But the strain gauge R2 is an active strain gauge that bonds on the specimen. The R2 can be used to measure the Poisson's ratio for the axial loading application. The half-bridge performs better than the quarter bridge (Bolton, 2015).

Figure 30

Standard half-bridge configuration I (Karuppasamy et al. 2019)

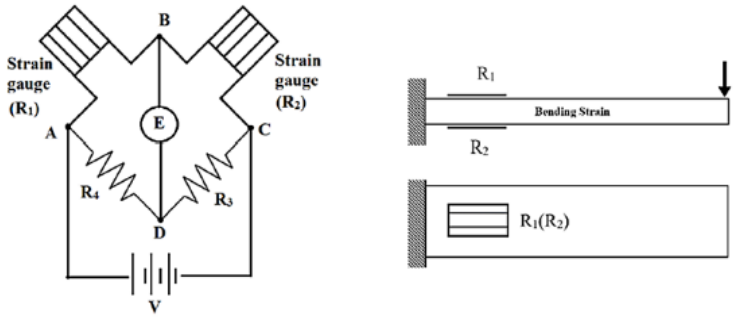

Figure 31

Standard half-bridge configuration II (Karuppasamy et al. 2019)

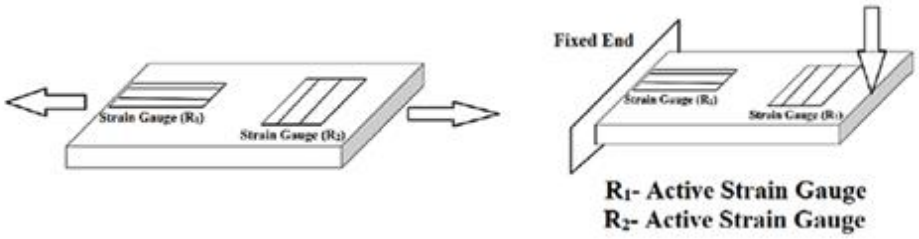

Figure 32 demonstrates three basic configurations of the full-bridge circuits (NI, 2020). All four arms are connected with active strain gauges in the full-bridge configuration. The full-bridge configuration I and II can only measure bending strain, and the third configuration can only measure the axial strain. Only configurations II and III can measure the Poisson effect. The full-bridge configuration is hard to be influenced by the temperature compared to the quarter bridge. It has better accuracy when compared to the other two strain gauge configurations (Karuppasamy et al., 2019).

Figure 32

Standard full-bridge configuration (NI, 2020)

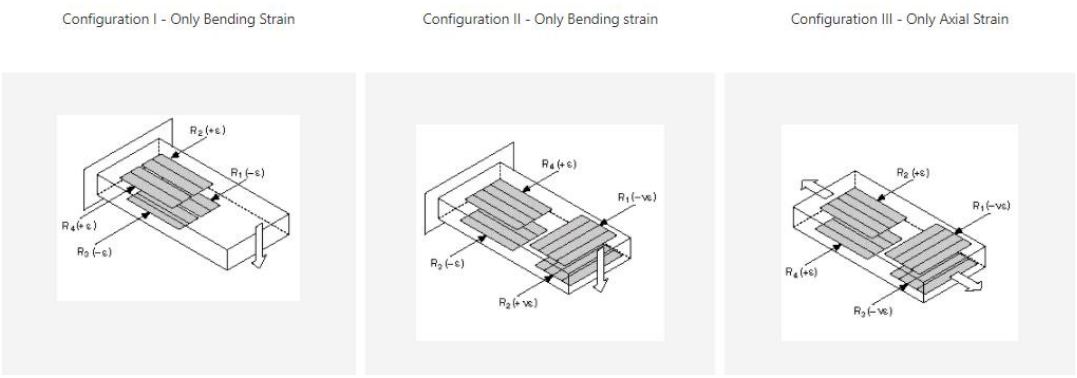

Table 3 summarises all the bridge configuration's measuring abilities. The strain on the aluminium joints and CFRP tubes will be measured during this experiment. Quarter bridge and half-bridge configurations can satisfy the experiments' bending and axial strain requirements, and fewer strain gauges are needed compared to the full-bridge configurations. The quarter bridge configuration will be used on the aluminium joints since this experiment will not happen in a rapidly changing temperature environment. The CFRP tubes will mainly be under bending load; quarter bridge and half-bridge configurations can measure bending strain. The half-bridge configuration II will be used on the CFRP tubes to monitor the strain change to provide accurate results.

Table 3

All bridge configuration's force measuring ability

Bridge type	Bending Force	Axial Force
Quarter bridge configuration I	Yes	Yes
Quarter bridge configuration II	Yes	Yes
Half-bridge configuration I	Yes	No
Half-bridge configuration II	Yes	Yes
Full bridge configuration I	Yes	No
Full bridge configuration II	Yes	No
Full bridge configuration III	No	Yes

As mentioned above, the Wheatstone bridge circuit can be plugged into the computer to store the monitored data (Karuppasamy et al., 2019). The computer's data are normally the circuit's output voltage. Calculations are required to convert the voltage

data to strain data. Figure 27 shows the standard Wheatstone bridge circuit (Karuppasamy et al., 2019). The following circuit calculation equations are from Khan et al. (2001).

The voltage across R1 and R4 are Vab and Vad.

Equation 3 (2.8.3)

$$\mathrm{Vab} = \frac{\mathrm{R2}}{R1 + R2} V$$

Equation 4 (2.8.4)

$$\mathrm{VaD} = \frac{\mathrm{R4}}{R4 + R4} V$$

The E represents the voltage output of the bridge circuit.

Equation 5 (2.8.5)

$$E = Vab - Vad = \frac{\mathrm{R1R3} - \mathrm{R2R4}}{(\mathrm{R1} + \mathrm{R2})(\mathrm{R3} + \mathrm{R4})} V$$

When the bridge is balanced, the voltage output will be zero. To achieve a balanced circuit, R1R3 – R2R4 will be zero.

Equation 6 (2.8.6)

$$R1R3 = R2R4$$

A balanced connection is important to the Wheatstone bridge circuit. The strain gauge generates a signal by the resistance change when it is deformed. When the strain gauge detects any change, the measuring device will capture a clear signal output. Thus, the circuits became unbalanced. Then, the voltage output can be back-calculated to the strain data. Equation 7 displays the strain calculation equation for quarter bridge configuration. Equation 8 displays the strain calculation equation for the half-bridge configuration. These equations only require voltage output (Vout), voltage input (Vin) and the gauge factor (Gf) to calculate the strain data.

Equation 7 (2.8.7)

$$\varepsilon = \frac{4\,\mathrm{Vout}}{Gf\ Vin}$$

Equation 8 (2.8.8)

$$\varepsilon = \frac{2\,\mathrm{Vout}}{Gf\ Vin}$$

2.9 Research Gaps

Chapter 2.2 states the advantages and disadvantages of general joining methods when applied to CFRP and aluminium alloy. Welding and fastening have defects on aluminium and CFRP joining. The welding is expensive and hard to conduct, and the fastening method will damage the CFRP's mechanical properties. But the adhesive bonding method won't affect the materials' properties and has a uniform stress distribution. And it won't face any corrosion problems.

Chapter 2.3 describes some typical applications of CFRP and metal by adhesive bonding methods. The application examples of the adhesively bonded hybrid structures are widely used in various engineering industries such as civil, marine and transport. The main purpose of using adhesively bonded hybrid structures is to improve mechanical performance, enhance fatigue life, and reduce weight and manufacturing processes. But adhesively bonded hybrid structure applications barely support loads directly because the adhesive's strength is normally smaller than the welding or fastening methods (Abdullah et al., 2012). Therefore, this project is suitable for further expanding the application of adhesively bonded metal-composite materials.

Chapter 3 Method

3.1 Previous design concept summary

This section is to introduce the previous design concept in more detail.

Figure 33 shows the general structure size of the attendant seat attachment. The demonstrator will simulate the attachment 1, 2, 7 and 8, as shown in the red rectangular area in figure 33. These four points are the main points used to connect the attendant seat. The four aluminium joints of the demonstrator are to simulate these four points. The original structure is a full aluminium structure at this location. The sizes shown in figure 3 are in inches and will transfer to the millimetre later to suit the New Zealand standard and are easy to manufacture when in SI unit.

As described in AIM Altitude's product manual. From AIM Altitude's document
A Material Variability Factor (MVF) of 1.15 is further incorporated into the minimum static strength requirement for a Type C fitting of 2,800 lbs and a type a fitting of 2300 lbs. Per Boeing D6-55441 Section 1.8.3, an MVF is incorporated to account for process and material variation in cases of single-unit testing. As the test coupons combine composite and metallic material, an MVF of 1.15 is considered conservative. The minimum test load is based on the type C attachment, 3220 lbs. This load equals 14330 N (See appendix A1 for detailed calculation steps).

Figure 33

The cabin attendant seat attachment layout from AIM Altitude

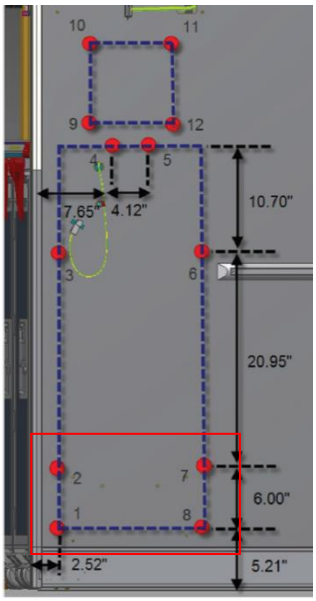

As shown in figure 34, the demonstrator is mainly assembled by CFRP tubes and cubic shape aluminium joints. The demonstrator consists of four aluminium joints and twelve CFRP tubes (two long and ten short tubes). The four aluminium joints represent the four attachments described above. And the CFRP tube is used to connect all four joints. The aluminium joints and the CFRP tubes will be bonded together by adhesive, and the joints should withstand at least 14330 N load.

Figure 34

Concept hybrid structure

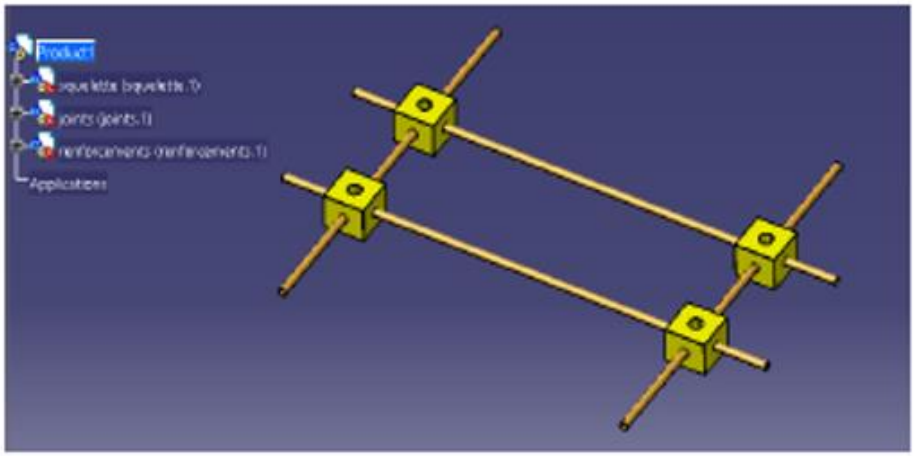

Figure 35 illustrates the concept of aluminium joint design. Figure 35 (a) shows that the top hole is a tapped hole used to connect the eyebolts. The big holes in figure 35 (b) are to join with the CFRP tubes.

Figure 35

Original aluminium joint block concepts design

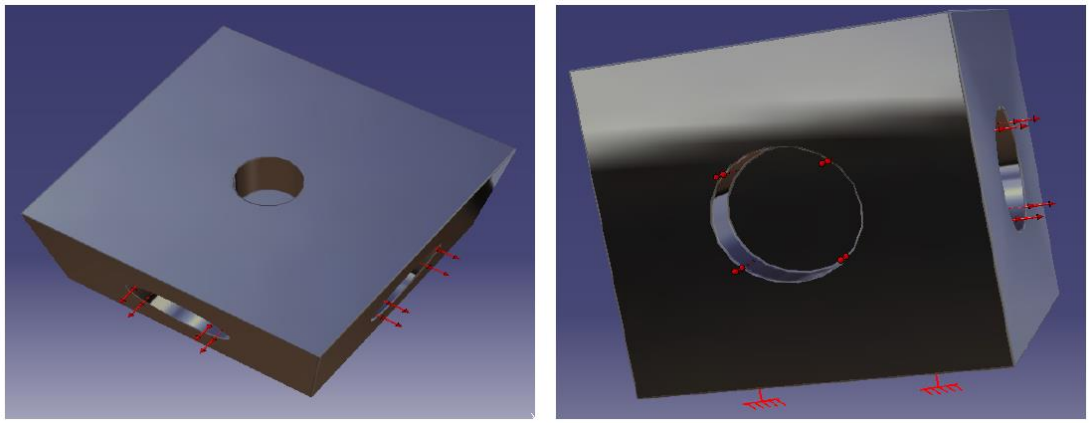

(a) (b)

Figure 36 shows the dimension of the aluminium joint. The side of the aluminium joints is 80 mm (s), the height is 60 mm (h), and the depth of the CFRP joining hole is 10 mm (d).

Figure 36

Original aluminium joint block concepts design's dimensions

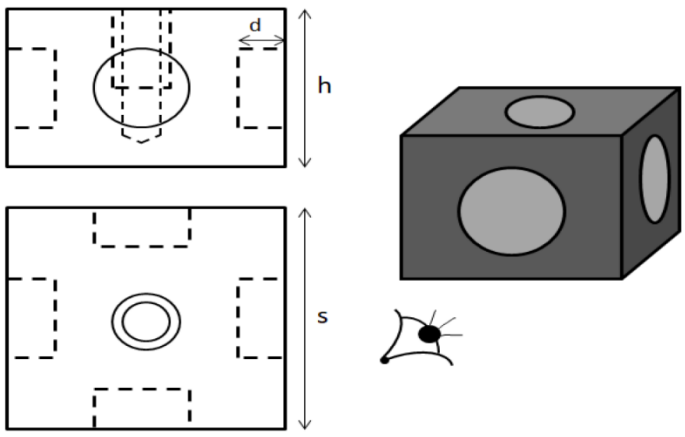

Figure 37 shows four eyebolts that will connect to the aluminium joints directly. The load will apply to these eyebolts, and each eyebolt will withstand at least 14330 N. They will screw into the aluminium joints' top tapped holes.

Figure 37

Four eyebolts used to connect with the pulling machines

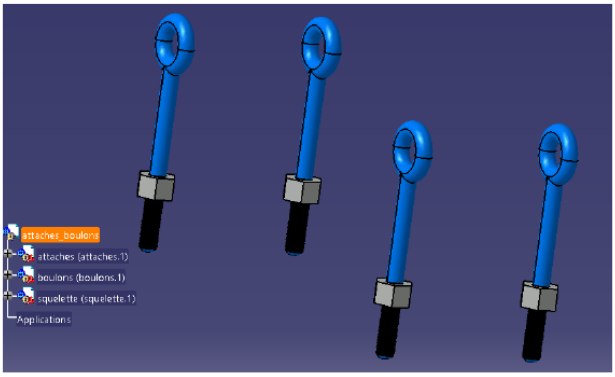

Table 4 displays the dimension data of the two CFRP tubes. There are two types of tubes, but the only difference is the length difference. The diameter of the two tubes is the same.

Table 4

The original CFRP tube design

	Outer diameter	Inner diameter	Thickness	Length
Short tube	30 mm	20 mm	5 mm	152 mm
Long tube	30 mm	20 mm	5 mm	365 mm

Figure 38 shows the holding parts used to hold the test demonstrators. The holding parts will fix to the test platform or test machine by fasteners.

Figure 38

Original concept design's holding parts for holding the test demonstrators

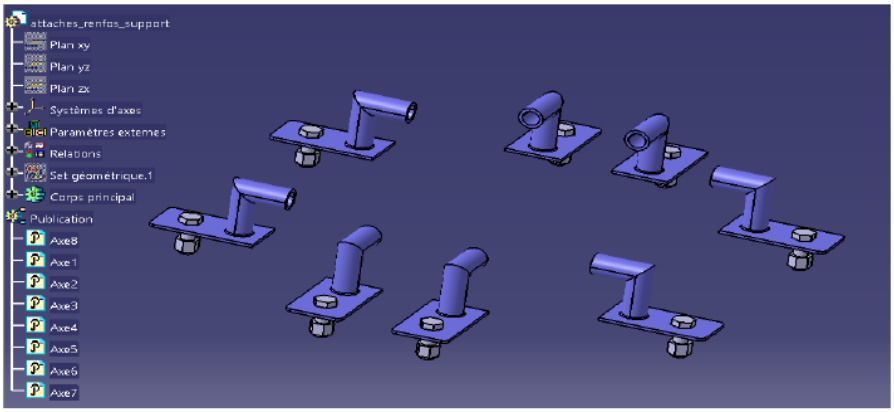

The first steps of the project are to verify the previous concept design. Parts that need to be re-checked are listed as follows:

1. The aluminium joints' dimension.
2. The CFRP tubes' dimensions.

The aluminium joints and the CFRP tubes need to be re-checked to examine whether they can withstand the minimum loading requirements (14330 N).

3.2 Verification, design and development

3.2.1 CFRP tube's verification

Figure 33 indicates that the length of the rectangular shape structure is 14.38 inches (point 2 to point 7 and point 1 to point 8), around 365 mm. And the short side is 6 inches, around 152 mm (point 2 to point one and point 7 to 8). The previous design's tube length was based on the distance between the attachment points. The aluminium joint's length had not been considered in the design. The CFRP tubes' length needs to be reduced to form a test demonstrator that has a closer dimension to the company's original design. The aluminium block's size is 80 mm x 80 mm x 60 mm and with four 10 mm holes.

Figure 39 demonstrates the new test demonstrator's configuration. The long tube's size was reduced to 305 mm from 365 mm to accomplish the length between two attachment points on the long side to meet 365 mm requirements. The short side was reduced to 92 mm from 152 mm to accomplish the length between two attachment points on the long side to meet 152 mm requirements. There will be only two CFRP tubes in the design, the 305 mm long tubes and the 92 mm short tubes. The reason that it only uses two types of tubes is to reduce the structural complexity. Only two types of backup parts need to be prepared, damaged parts can be replaced easily, and it could further reduce the chance of the wrong installation because two parts were too close.

Figure 39

CAD drawings of a new test demonstrator's configuration

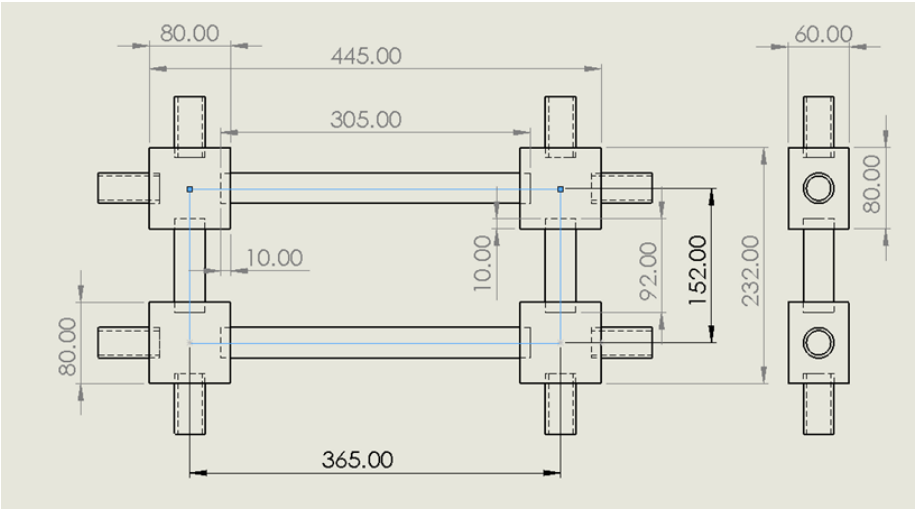

Figure 40 demonstrates the first modified design and the original concept's difference. The left structure is the original concept, and the right is the modified design. The first modified design is smaller than the original concept, reducing the test demonstrator's material cost and weight. From the original concept, the blue rectangular shape indicated the actual attachment points' position and the new design also has a closer layout to the company's original design.

Figure 40

CAD drawings comparison between the original concept and the modified design

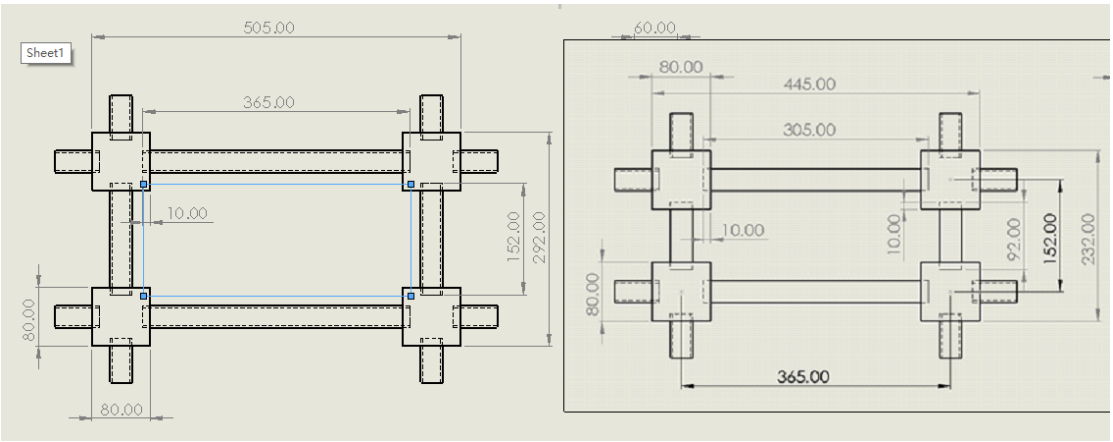

Note. The left CAD drawing is the original concept, and the right drawing is the modified design.

Appendix A2 describes detailed calculation steps of the CFRP tubes' verification. During the initial stage, the verification mainly relied on hand calculations. Table 5 displays the CFRP tubes' basic mechanical properties. The data was retrieved from the supplier and the CES EDU Pack. The CFRP tube is mainly under bending force. Therefore, tensile and compression will be the main force application. Based on the initial calculation, the tensile stress applied to the CFRP tubes is 36.5 (the applied load is 14330 N). The shear force results will be the same as the tensile strength since the cross-section area are the same. Both of the stress are smaller than the material strength. Therefore, the original CFRP tube design is safe to use (The factor of safety is 4). The original tube size remained unchanged to provide a better shear strength since the shear force direction is the weakest side of the CFRP tube.

Table 5

CFRP tubes properties

Young's modulus	86.4 GPa
Tensile strength	738 MPa
Shear strength	45 MPa

3.2.2 Aluminium joints design and verification

Aluminium joints in the original concept were connected with eyebolts. The eyebolts were screwed into the tapped hole on the aluminium joints. The first development for the aluminium joints is to modify the tapped holes into the clear-through non-threaded hole. This modification is because the clear-through hole is easier to manufacture and could provide a larger tolerance. Therefore, a hex nut will secure the eye bolt on the aluminium joints.

The minimum required test load of the test demonstrator is 14330 N, which is 1461 kg. From the supplier's catalogue, M8 eye bolts have a load capacity of 1800 kg, higher than the minimum required test load. The factor of safety is 1.23 (See Appendix A3 for all the calculations related to the bolt selection). An M10 eye bolt with a breaking load of 2400 N was selected, and the new safety factor is 1.64. The M10 bolt's tensile strength is 500 MPa, and the cross-section area is 58 mm^2. So, the tensile stress applied to the bolt is 247 MPa, smaller than the bolt's strength. The factor of safety is around 2. An estimate of deformation is around 0.138 mm of the M10 eye bolt under 14330 N loads. The calculation results suggest the M10 eye bolt is safe during the experiments.

Bolt hole size selection was based on ASME B18.2.8 (ANSI, 2017). There were three types of fit classes which were normal, close, and the lose class. The normal fit class was selected. The nominal drill size for the M10 bolt application is 11 mm with a tolerance of 11.27 mm (See Appendix A4).

The aluminium joint's original design size was 80 mm x 80 mm x 60 mm. A verification process needs to be processed. And to finalize the dimension of the aluminium joints to check whether they can stand the test loading or could be further reduced in size to save budget. (See Appendix A5 for all the calculations below).

The first step is to check the tensile stress. The test load will apply to the wash of the eyebolt. A standard M10 washer has an outer diameter of 21 mm with a 10 mm inner diameter. Therefore, the cross-section area is around 267.82 square millimetres (2.6782×10^{-4} m^2). The minimum test load is 14330 N. So, the tensile stress applied to the aluminium joint is 53.5 MPa. The 6061 T6 aluminium's yield strength is 300 MPa. The safety factor is 5.6, which is reliable enough for the experiment.

The second step is to check the shearing stress applied to the aluminium joints. The cross-section of the shearing area is equal to the sum of two rectangular areas. The long side of the rectangular area is the height of the aluminium joints, which is 60 mm. The short side of the rectangular area is the width of the wash, which is 11 mm. Therefore, the total shearing area is 7920 mm^2 (7.92×10^{-3} m^2). The minimum test load is 14330 N. So, the shearing stress applied to the aluminium joints is 1.8 MPa. The shearing stress is very small. It will not have a strong influence on the aluminium joints.

The third step is to check the deformation of the aluminium joints. The load will apply from the bottom of the aluminium joints and at the washer's position. To calculate the aluminium joints' deformation, the structure can be simplified to a hollow cylinder with the same height as the aluminium joints and the same bottom area of the washer. The washer's area is 2.6782×10^{-4} $m^{2,}$ and the height of the aluminium joints is 60 mm. The 6061 T6 aluminium's Young's modulus is 75.6×10^3 MPa. Therefore, the deformation is 0.0424 mm. The deformation is small, and the aluminium joints' deformation checking process can be ignored in future development.

3.2.3 Aluminium joint parts development

Figure 41 displays the current aluminium joint's dimension. The joining holes are only 10 mm deep. The aluminium joint's side dimension is 80 mm x 80 mm. With only four 10 mm depth holes in one aluminium joint, lots of the material will be wasted. And at this stage, the influence of the hole depth was still unknown. This test demonstrator is the first prototype to undergo physical experiments, and the design can be overdesigned. Based on Pisharody et al. (2019), the large bonding distribution area will have stronger strength. So, the assumption is that the larger the adhesively bonded area, the stronger the strength. The holes on the aluminium joints will be extended as much as possible, but the aluminium joints' dimensions will not be increased to avoid further increased cost and weight. The longer the joining hole depth, the larger the adhesively bonded area, and the better the stability of the joint structure.

Figure 41

The CAD drawing of the aluminium joints with 10 mm depth holes

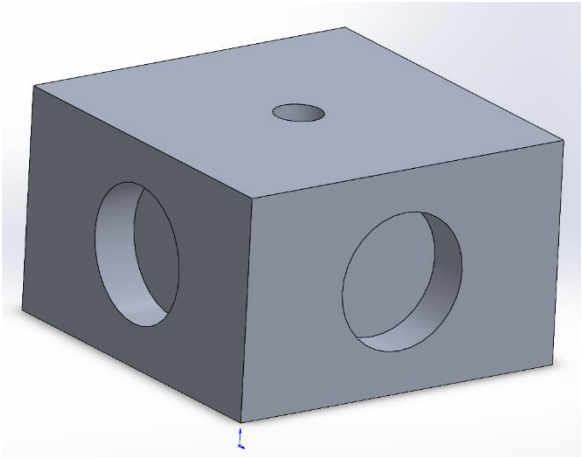

Figure 42 shows a concept aluminium joint that with clear through holes. This concept can maximise the hole depth. But this concept will increase the manufacturing process. It will be hard to bond the CFRP tubes into the right position. If one CFRP tube is bonded to the wrong position, it will influence an accurate configuration of the whole structure. The test demonstrators may not be able to secure the test platform accurately, which will cause additional steps to fix the installation parts, such as the

screw holes position. Therefore, the holes cannot be designed to clear through configuration. They must have solid ends to prevent the physical influence between the CFRP tubes, and the solid end holes can ensure the CFRP tubes will be bonded to the right positions.

Figure 42

The CAD drawing of the aluminium joints with clear through holes

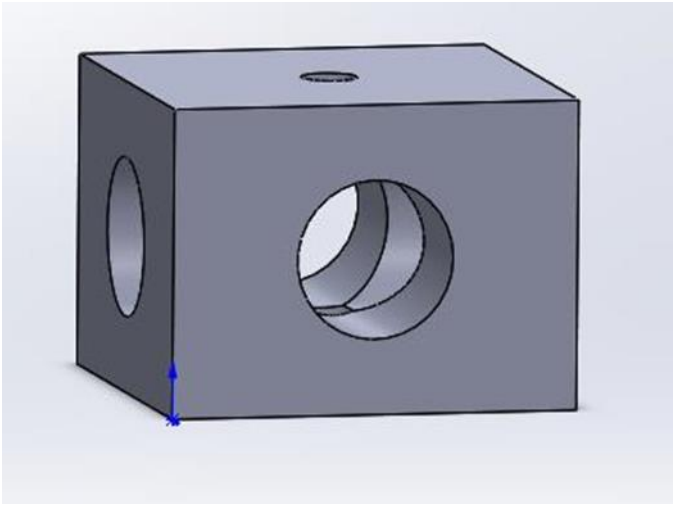

Figure 43 demonstrates the maximum available hole depth. The depth of the hole must be smaller than 24.6 mm. Otherwise, the CFRP tubes will influence each other during the assembly process. The CFRP tubes should avoid making any physical contact with each other tubes.

Figure 43

The CAD drawing of the aluminium joints with 24.6 mm depth holes

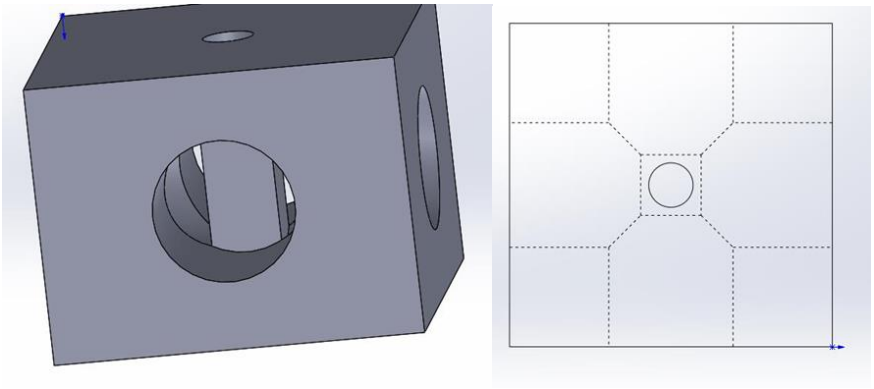

Figure 44 demonstrates a new concept design. There will be four holes in the aluminium joints. The depth of the holes was 20 mm. To further maximize the use of the hole depth, the hole depth was increased to 23 mm.

Figure 44

The CAD drawing of the aluminium joints with 23 mm depth holes

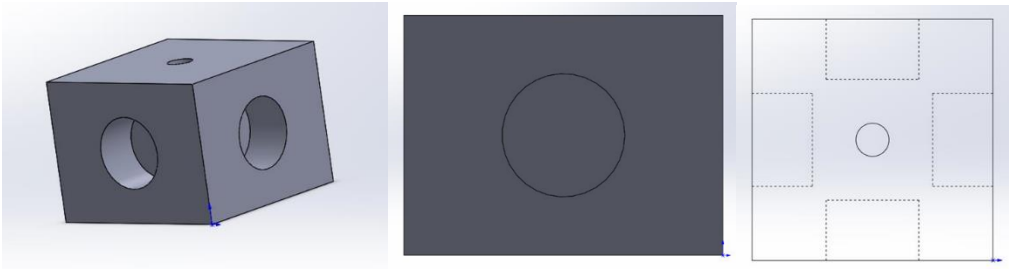

The initial adhesive layer thickness recommendation was 0.3 mm to 0.5 mm. The CFRP tubes' outer diameter is 30 mm. So, the hole diameter must include the adhesive thickness and the CFRP tube dimension. To have a hole design that can bear a maximum tolerance of 0.1 mm, the 0.4 mm adhesive was selected. The hole diameter was 30.8 mm. In this case, the adhesive layer will still be in the 0.3 mm to 0.5 mm range when the hole diameter is 30.7 or 30.9. Therefore, the hole diameter was designed to be 30.8 mm. The new study shows that epoxy has an optimal thickness of 0.2 mm (see chapter 2.5). To fit this thickness, the hole diameter was decreased to 30.4 mm.

The CFRP tubes have a diameter of 30 mm, smaller than the 30.4 mm holes. Figure 45 demonstrates the gravity that will make the CFRP tube drop and attach to the bottom of the hole. There are two serious problems, the first one is the CFRP tubes cannot be located at the centre, and it will cause an unevenly distributed adhesive thickness. Therefore, the next step is to refine the design to ensure the CFRP tubes can maintain the centre of the holes and the 0.2 mm adhesive thickness.

Figure 45

The CFRP tube drops and attaches to the bottom of the joining hole

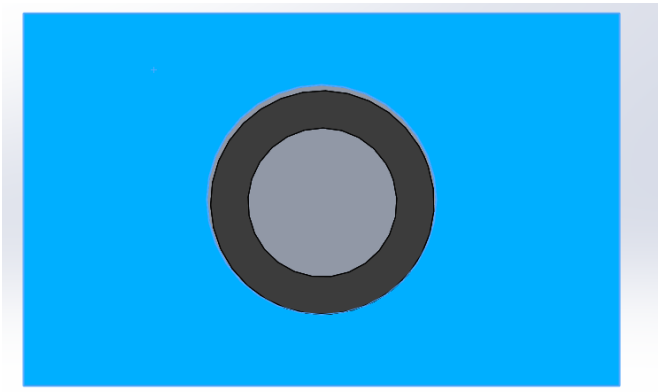

Figure 46 (a) demonstrates a new joint design. This joint has a 5 mm depth bottom section with a 30 mm diameter, similar to the CFRP tubes' diameter. The tube can be inserted into the bottom hole, and this structure can hold the CFRP tube tight and provide further bending support to the CFRP tubes. Figure 46 (b) shows a top holding part to provide additional support to the CFRP tubes to ensure the tubes can be located at the centre of the joining holes. Three rectangular shape parts will join the aluminium joints at the section near the surface. The holding parts will be 3D-printed. A round ring-shaped holder replaced the complex structured holder to simplify the design further, as shown in figure 47 (a). Figure 47 (b) shows that a larger round section near the top of the hole needs to be extruded to fit this holder. The ring shape holder will be 3D-printed.

Figure 46

New joints design

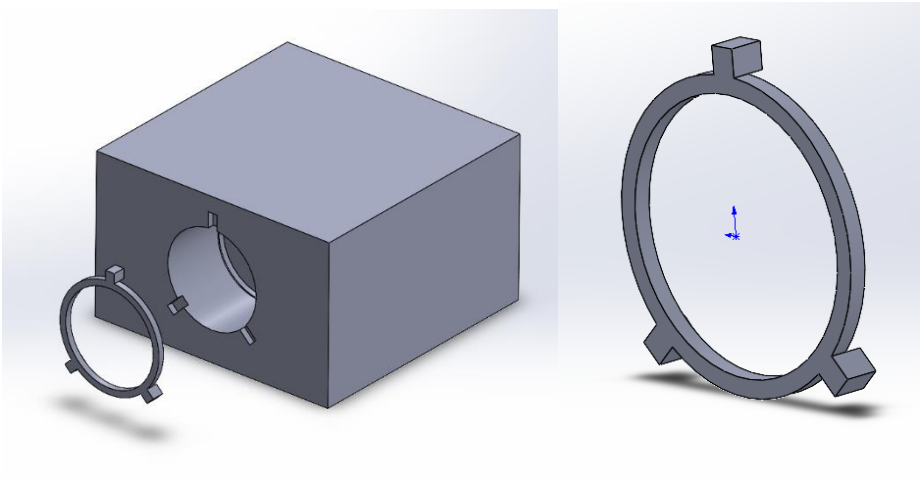

(a) (b)

Note. (a) The new joint design layout. (b) The top holding part in the new joints design.

Figure 47

The simplified joints design

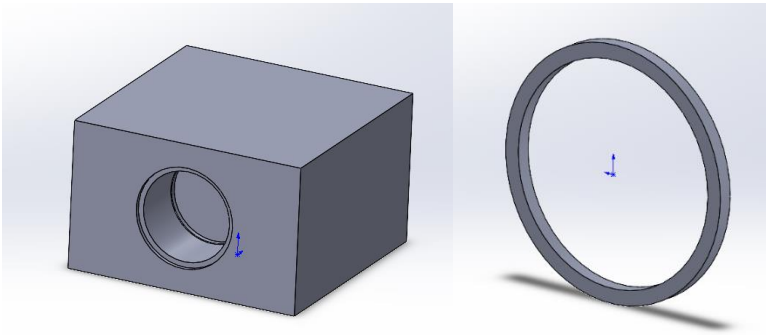

(a) (b)

Note. (a) The simplified joints design layout. (b) The top holding part in the new joints design.

The new joint involves two designs to ensure the CFRP tubes will be located at the centre of the joining holes. One is at the bottom of the hole, and another is at the top. So, four points will hold one CFRP tube between two joints. Based on the theory of two points form one straight line, only one design is needed to hold the CFRP tubes. Figure 48 demonstrates only the bottom hole design had been selected as the remaining

design. This design does not require additional parts to support the CFRP tubes and can provide additional bending support to the tube. This design is enough to increase the structure's strength and stability.

Figure 48

The CAD of the bottom hole holding section

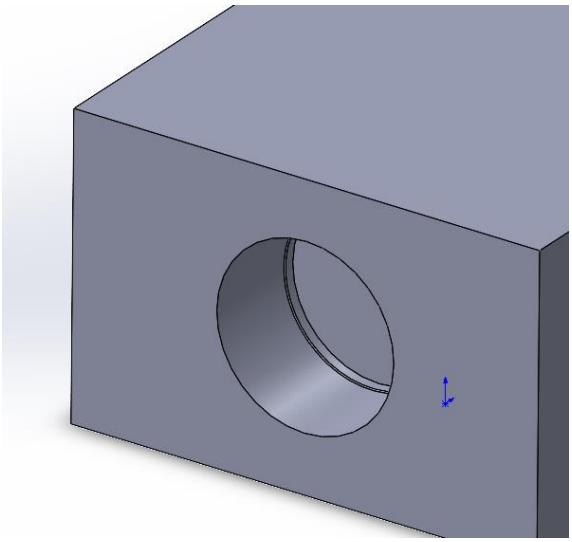

The new bottom hole is 5 mm in-depth, and the diameter is 30 mm, the same as the CFRP tubes. Figure 49 shows a chamfered design on the bottom hole's edge. This chamfer design aims to make the CFRP tubes' joining process easier. The chamfer can let the CFRP tube slide into the hole smoothly and avoid to stuck on the flat edge.

Figure 49

Chamfer design at the edge of the bottom hole section

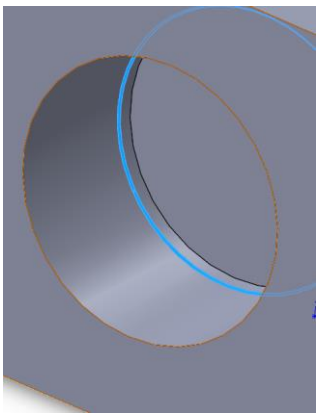

During the assembly process, the adhesive and air cannot be trapped at the bottom of the joining hole. The CFRP tube's position will be influenced if the air and the adhesive are trapped at the bottom. The tube will have some distance to the bottom, which will change the structure length and decrease the accuracy of the overall dimensions. For example, the trapped adhesive increases an additional 2 mm to structure length. Other parts may not be aligned. An additional design is needed to ensure the trapped air and excess adhesive can be squeezed out. Figures 50 exhibits a small pathway design. This design aims to ensure the excess adhesive or trapped air can be belched out from the bottom. When the CFRP tubes are pushed into the bottom hole, the air and the adhesive will be flushed out from these small pathways. This can ensure no additional objects are trapped at the bottom.

Figure 50

A small pathway is designed to ensure the trapped adhesive can be squeezed out

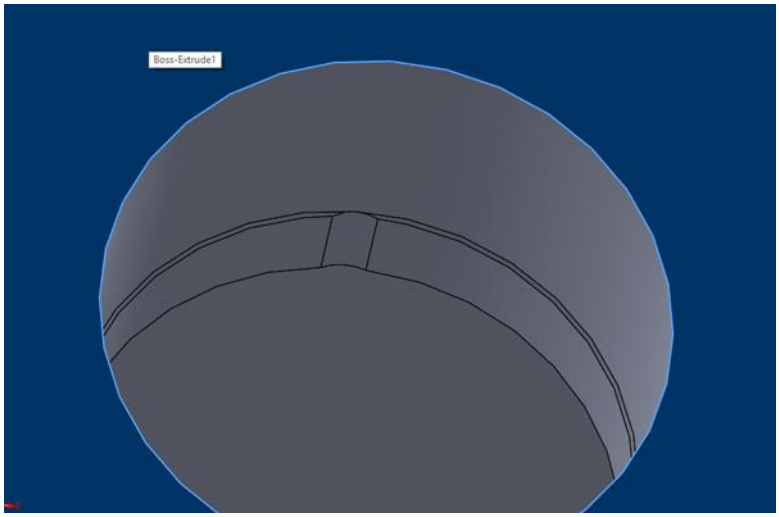

Since the aluminium joint holes dimension was changed from 10 mm to 23 mm, the CFRP tubes need to increase their size to maintain the original structure dimension. The joining holes' depth increased by 13 mm, meaning each CFRP tube needs to increase by 26 mm. So, the long CFRP tubes were increased to 330 mm. Its size should be 331 mm long; the reason to cut 1 mm is to simplify the CFRP tube preparation and the checking process. Only 1 mm short won't influence the overall structure. The short tubes increased to 120 mm and are 2 mm longer than the length

needed to increase by 26 mm (118 mm). 120 mm is easier to check and prepare compared to the 118 mm tubes, and a 2 mm difference won't cause a huge influence on the test demonstrators. Figure 51 shows the test demonstrators' dimensions at this stage.

Figure 51

The final test demonstrators' dimension at the current stage

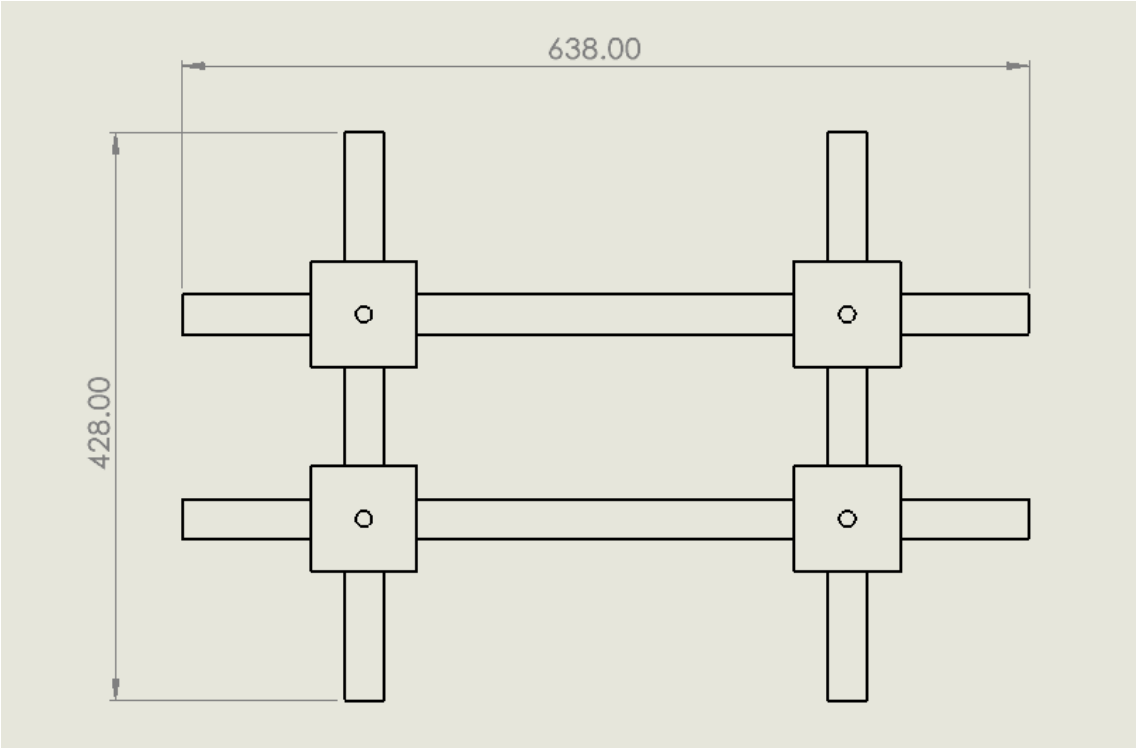

3.2.4 Plug design

Plugs are needed to seal the CFRP tubes. The purpose is to ensure the sealed tube can push all the adhesives out from the bottom hole. Because the CFRP tubes are hollow, the adhesive may remain in the CFRP tubes' hollow section. The bonding area may not have enough adhesive remaining. This process ensures all the adhesives are evenly applied to the joining section and will not remain inside the CFRP tubes. Once the CFRP tubes are sealed, the CFRP tubes can squeeze out all the adhesive and make sure the adhesive is fully applied to the bonding section. Figure 52 demonstrates three different plug designs. All the parts are 3D printed.

Figure 52

CAD drawings of three types of plugs for sealing the CFRP tubes

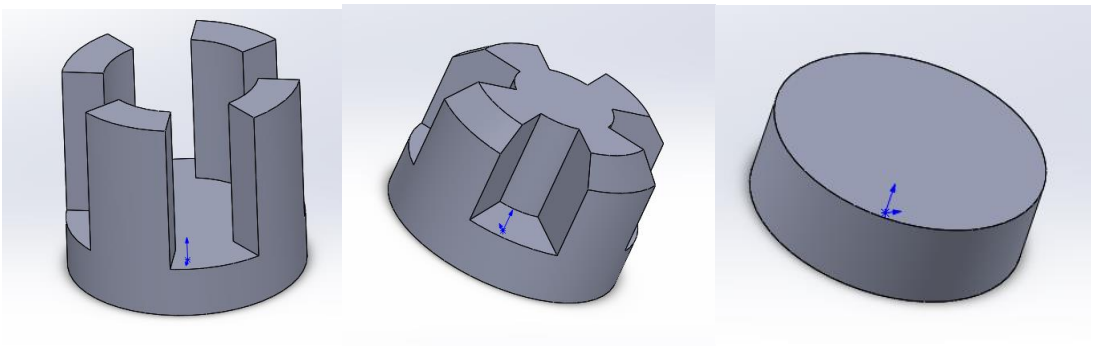

(a) (b) (c)

Figure 53 shows the 3D printed plug parts. The plugs were bonded to the yellow glass fibre tubes. The glass fibre tube dimension was smaller than the CFRP tubes. The experiment aims to test the plugs' sealing ability.

Figure 53

3D printed test parts

Two bonding methods were conducted. The first one is to insert the plug and then apply the adhesive to seal the gaps. The second one is to apply adhesive on both sides of the tubes and the plugs. Then assemble them.

Figure 54 shows four samples were tested by adding water into the tube. Samples 1 and 2 used method one, and samples 3 and 4 used method two. Sample 2 is leaking. Sample 3 was leaking too, but the leak was from a hole in the tube body. Figure 55 shows the leak was stopped when the facture was fixed.

Figure 54

Samples 1, 2, 3 and 4 (From left to right)

Figure 55

The small hole on sample 3 that caused the leaking was fixed

The plug design can ensure the adhesive will not enter the CFRP tubes' hollow section. The adhesive can be pushed out and applied evenly on the bonding surface. All three types of plugs were tested. The results show the simple round shape plug is sufficient for the job.

Figure 56 shows the final plug parts for the CFRP tubes. It is 3D-printed. The outer diameter is designed to be slightly larger than 20 mm with a 5 mm thickness. The PLA plastic can be squeezed into the hollow inner section of the CFRP tubes without additional adhesive. The plug can join the CFRP tube tightly.

Figure 56

The CAD drawing of the final plug design

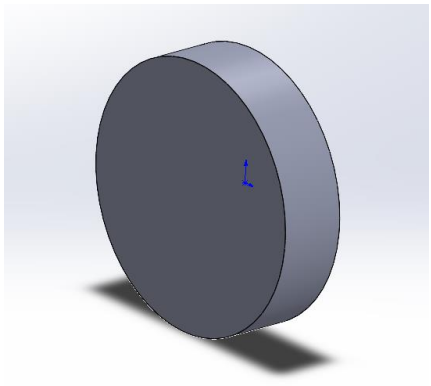

3.2.5 Test demonstrator holding plan

The test demonstrators are required to fix onto the test machine or platform. Holding parts are needed to secure the test demonstrators. Figure 57 shows the original design's holding part. It is built with one L-shape tube structure holder and a metal plate. The L-shape is welded on the thin metal plate, and the holding parts are secured to the test platform by a bolt. The CFRP tubes of the demonstrators will directly connect to the L-shape tube. The L-shaped holding parts are hard to manufacture due to their complex shape. The purpose of the L-shape tube is to hold the CFRP tubes. A simpler part can replace the L-shape to achieve its purpose.

Figure 57

The original holding parts design

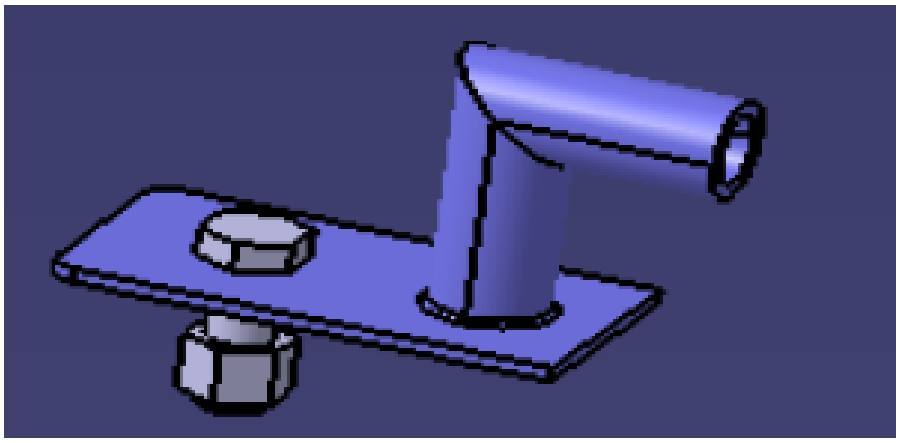

Figure 58 demonstrates a new concept of holding parts. The L-shaped tube was replaced by a rectangular-shaped metal bar with a round head and a 30 mm hole to connect the CFRP tube. The bar-shaped holder was also welded to a thin metal plate, and it will secure by four screws. The four screws can provide better stability when compared to the original concept, which only has one bolt. Figure 59 demonstrates the test demonstrator that the new holder holds.

Figure 58

New holding parts design

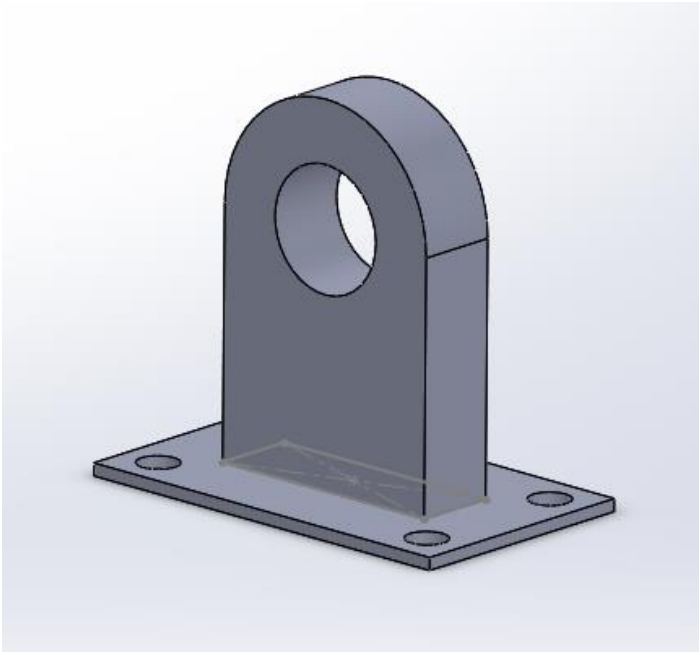

Figure 59

New test demonstrator setup

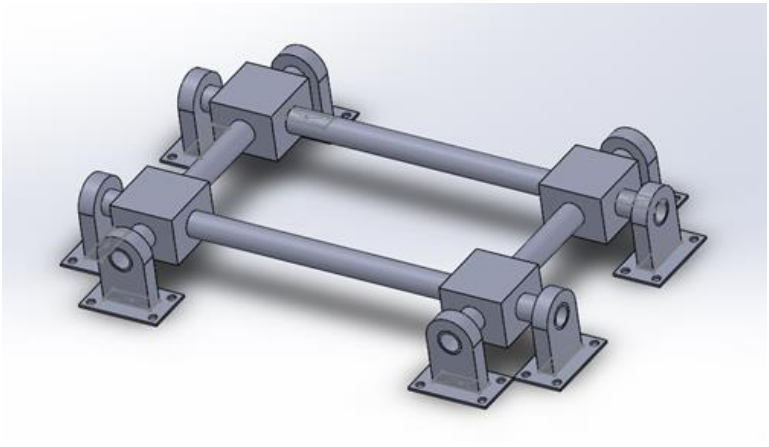

But this concept still has some disadvantages. The first one is this design requires three types of materials. The aluminium plate and two types of aluminium alloy bars. And the holding parts require too many steps to finish. The holding parts need to be welded on the plate. This process is quite complex and must be done manually. The accuracy of the parts is hard to guarantee. And the weld strength must be tested before conducting the experiments.

The ideal design is to use the same material used by the aluminium joints, which can be processed in a similar manufacturing method. The aluminium joints will be manufactured at the university workshop's CNC machine. To reduce the manufacturing steps and to reduce the material list complexity. The final concept has been developed, as shown in figure 60. This design's holding parts are the same as the aluminium joints, except it only has one hole to joint with the CFRP tubes. The aluminium joints and the holding parts can be manufactured based on the same types of raw material. This design doesn't need manufacturing steps other than CNC machining; only one main program is needed to manufacture all the aluminium parts. A long bolt will secure the holding block. And the size of the bolt will use M12 size. The previous section proves the M10 eye bolt can withstand the minimum test load. This section can skip the checking process because the M12 bolt has a better mechanical performance than the M10 eye bolt. Figure 61 demonstrates the test demonstrator and the holding parts' final concept design. The bolt hole on the aluminium holding blocks is 13.5 mm, and the design was based on the standard (ASME) (see Appendix A4).

This design further reduces the manufacturing steps and the complexity of the part. Further product development will base on this concept.

Figure 60

The final concept design of the aluminium holding blocks

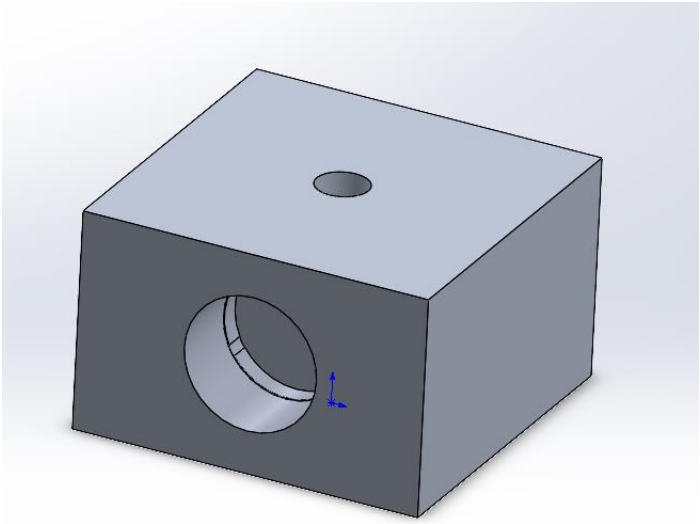

Figure 61

The complete final test demonstrator's concept design

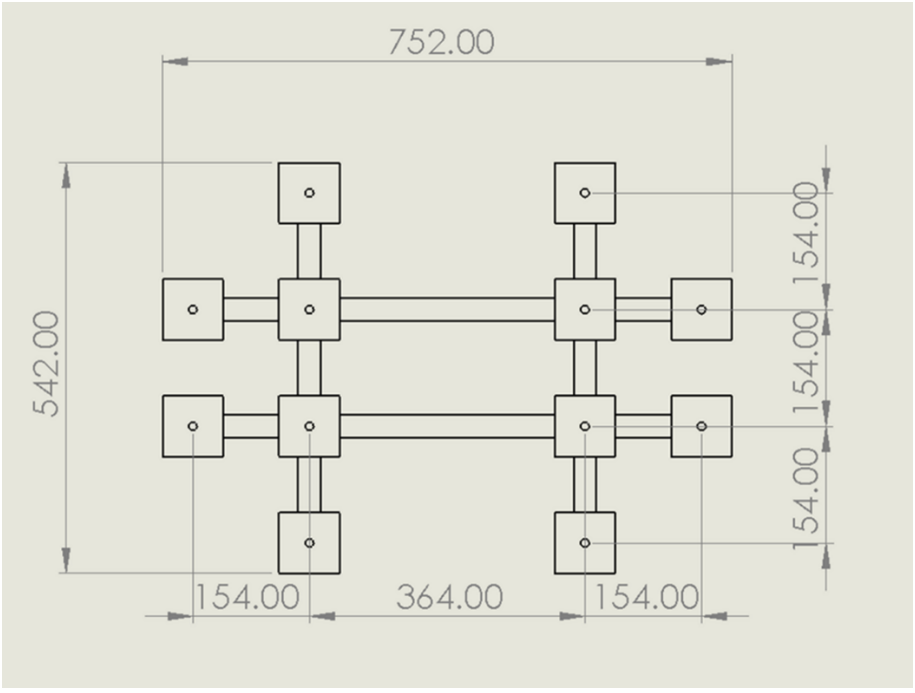

3.2.7 Test method plan change

Figure 62 demonstrates the test plan in the original design concept. The structure was under four identical pulling forces in four aluminium joints. A honeycomb paper panel is attached to the test demonstrator. The paper panel in this experiment will be the same as the company uses in the real product. The purpose of attaching a honeycomb paper panel is to simulate the effect of the kitchen wall panel on the galley wall. The paper panel may provide additional strength to the overall structure but won't significantly influence the overall bonded joint strength during the experiment.

Figure 62

The original test plans

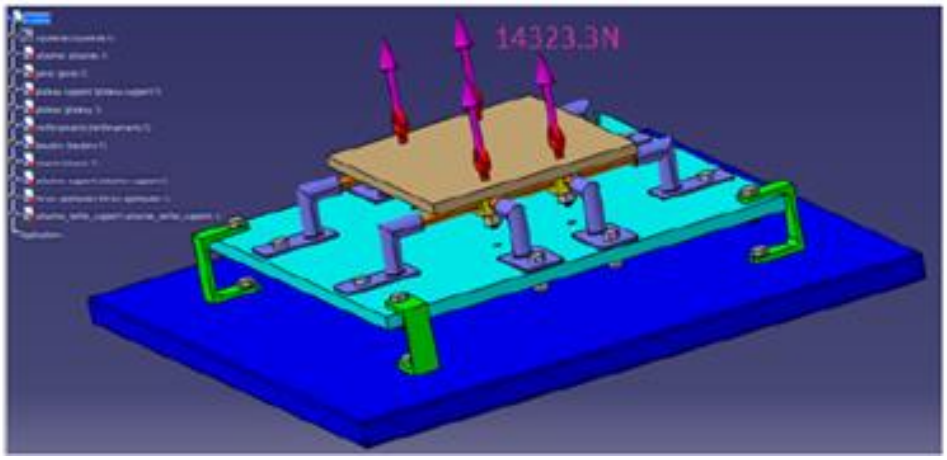

Figure 63 illustrates all the loads applied to the short CFRP tubes (Marked in red). The four CFRP tubes in the centre did not take any loads.

Figure 63

All the loads applied to surrounding short CFRP tubes (Marked in red colour)

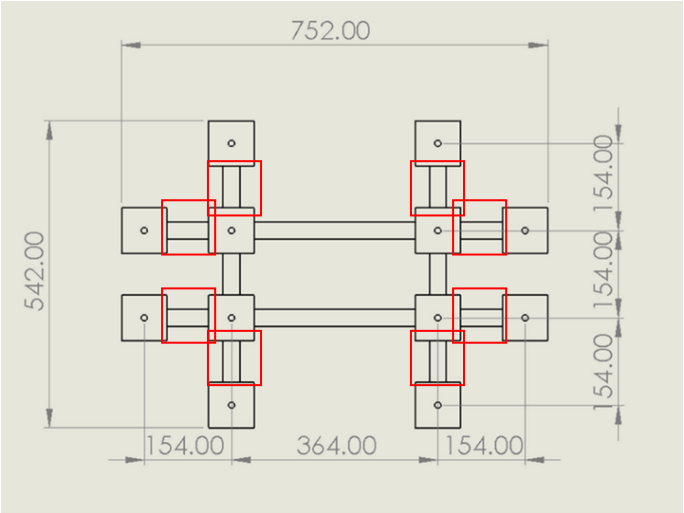

The main purpose of this experiment is to test the concept of the adhesively bonded hybrid joint structure. The current testing plan may not provide a reasonable analysis because half of the CFRP tubes are under zero loading conditions. Four CFRP tubes joining the aluminium joints must undertake loadings to analyse the hybrid joint structure's performance better. Figure 64 illustrates a new plan which only pulls at one eye bolt. Three normal M10 eyebolts can only replace the other three to hold the honeycomb paper panel.

Figure 64

New test layout

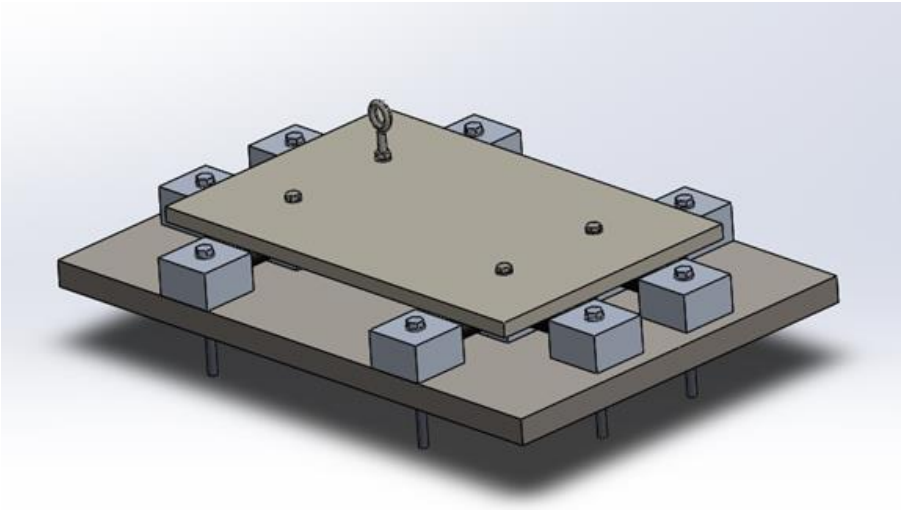

Figure 65 shows the new load distribution. The load will mainly apply to the red and blue areas. Other parts will still bear some load, but smaller than the tubes in red and blue colour areas. The assumption is that the two short CFRP tubes (blue colour) will bear the most loads.

Figure 65

New load distribution figure

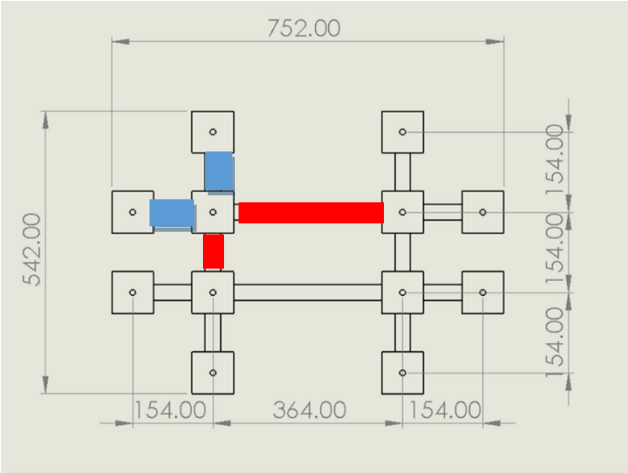

3.2.8 New test demonstrator deformation verification

The new design of the test demonstrator needs to be checked before starting the manufacturing process. This section is to verify the structure's stability. Figure 66 displays a simplified structure for the test demonstrator's deformation calculation. Only the parts surrounding the pulling points are included in the calculation. The structure had been treated as four cantilever beams; each beam's length is from the aluminium joints to the pulling points. All the calculations were based on the four CFRP tubes that will have the same deformation. Therefore, the three short CFRP tubes will bear most of the load. The calculation result shows that the deformation will be acceptable at 0.524 mm (See Appendix A6). The actual deformation during the experiments will be higher than the calculation results because the material may contain flow (Callister et al., 2018).

Figure 66

The simplified structural drawing for calculation

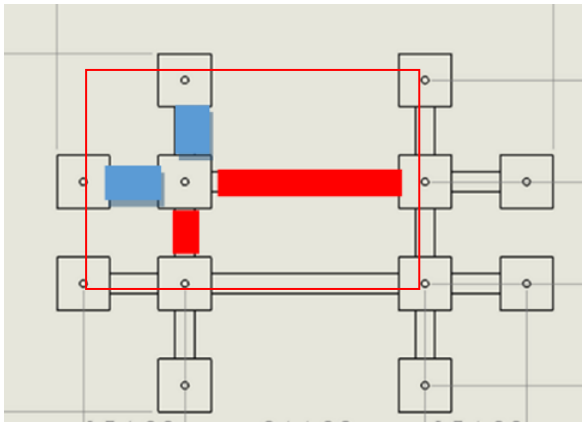

Figure 67 illustrates the FEA analysis results. The deformation of the structure is 0.8 mm. The deformation of the CFRP tubes is not the same, and the long CFRP tube has the largest deformation. But the results were close.

Figure 67

FEA analysis of the structure deformation

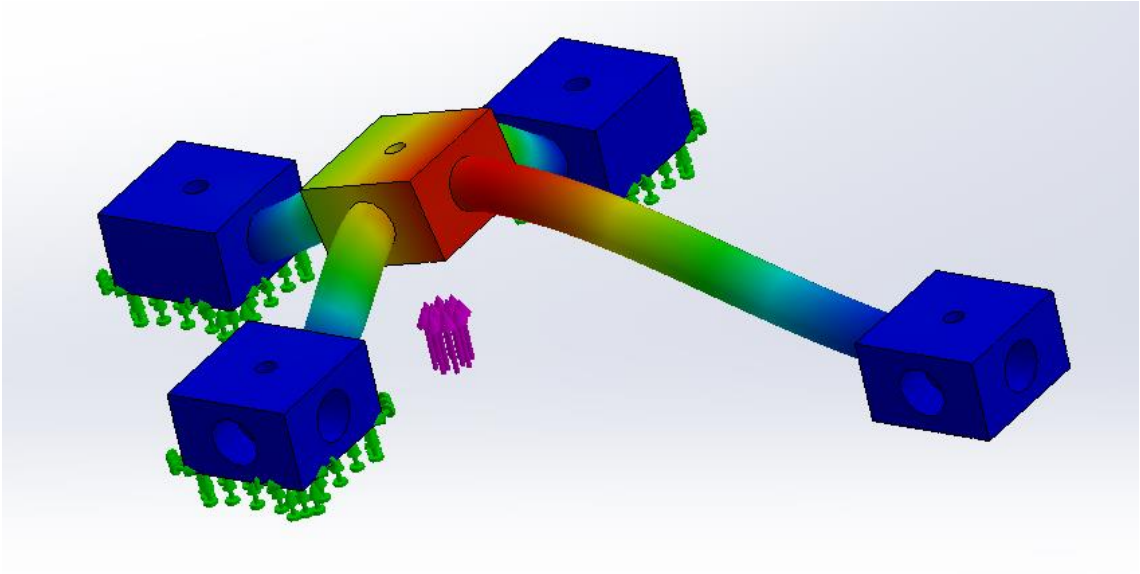

3.2.9 Slot design

The test demonstrator will be placed on a steel plate. To make the test demonstrator have a large tolerance that will fit on the steel plate. The bolt holes on the aluminium holding blocks were changed to slots. Figure 68 shows the new slot design and the new test demonstrator setup. The slot design can increase the chance that all three test demonstrators can fit in the same position.

Figure 68

The final design of the aluminium holding blocks

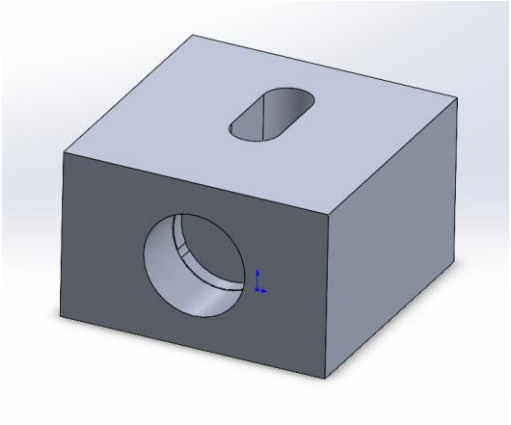

3.2.10 Aluminium material ordering and re-design

The final concept contains twelve aluminium parts that are 80 mm x 80 mm x 60 mm. The required aluminium alloy material for this test demonstrator is 6061 T6. From the supplier's stock, the minimum standard aluminium flat bar size that suits for manufacturing of the current aluminium parts is 101.6 mm x 76.2 mm. To manufacture the current aluminium parts, roughly 38% of aluminium will be wasted during the manufacturing process. The size of the aluminium joints should be further reduced to reduce material waste and cost. The 80 mm x 80 mm cannot be reduced because these two sides must provide as long as possible for bonding with the CFRP tubes. At the current stage, the effect of the bonding length on the structural strength was still unclear. For better bonding strength, the current bonding area shall remain unchanged. Therefore, the only part can be changed is the height of the aluminium parts. The

current height of the aluminium joints and the holders is 60 mm, and the CFRP tube outer diameter is 30 mm. Figure 69 demonstrates a CAD drawing of the aluminium joints. There is a 15 mm distance from the aluminium joints' top and bottom to the CFRP tubes. Based on the previous FEA analysis results, the aluminium's minimum height requirement is 40 mm (Maxime, 2019). But there are only 5 mm from the top and the bottom of the aluminium joints to the CFRP tubes. The aluminium joints may not hold the CFRP without a break, and there is no suitable standard material for this size's manufacturing. Table 6 displays the available material list, and the available flat bar only has three sizes. The smallest's width is only 38.1 mm, which is smaller than 40 mm. The best option is to use the 50.8 mm one, and the aluminium joints' height can be reduced to 50 mm. The 40 mm height joints are still required to be manufactured from the 50.8 mm. It will waste more materials and has a lower strength. Therefore, the aluminium height is better to reduce to 50 mm and use the 101.6 mm x 50.8 mm aluminium flat bar. The cost of the materials can be further reduced to 70% of the 76.2 mm flat aluminium bar.

Figure 69

CAD drawing of the aluminium joints

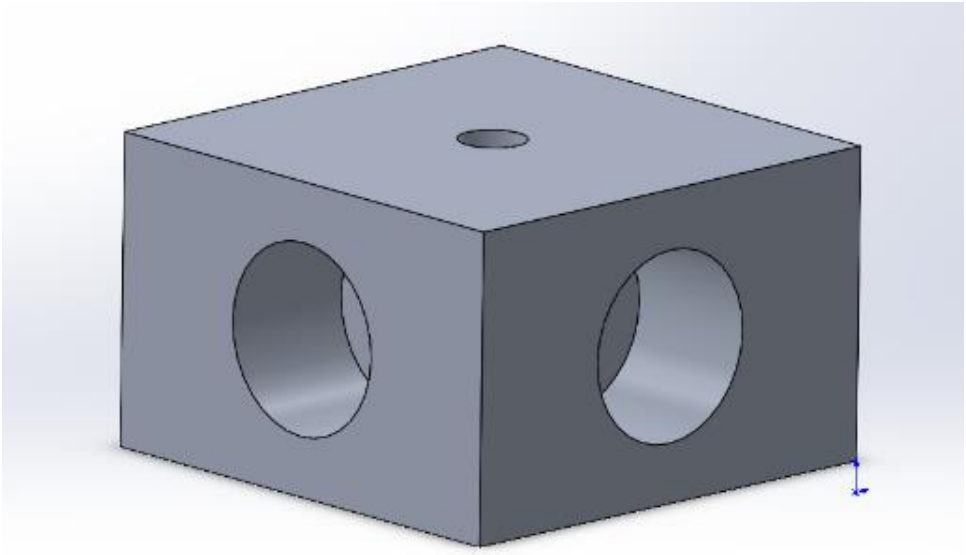

Table 6

The available flat bars information.

Die Number	A (mm)	B (mm)	R (mm)	Mass (kg/m)	Perimeter (mm)
EF3810	101.60	38.10	0.40	10.450	280
EF1016	101.60	50.80	0.40	13.990	305
EF0762	101.60	76.20	0.40	20.760	356

Figure 70 indicates the geometry of the flat aluminium bar, the A-side is 101.6 mm, and it can be used to manufacture the 80 mm side of the aluminium joints. And the B side is 50.8, and it can be used to manufacture the 50 mm height of the aluminium joints. The length of the raw material is based on the number of aluminium joints required. A total of three test demonstrators are needed, which means a total of 36 aluminium joints need to be manufactured. The remaining side of the aluminium joints is 80 mm, plus 10 mm for cutting. Manufacturing each aluminium joint requires a 90 mm raw aluminium fat bar length. Thirty-six aluminium joints require a 3240 mm length of the raw material. An entire aluminium flat bar is 3660 mm long, slightly longer than the test demonstrators require. So, the entire bar can be purchased, and the rest of the material can be treated as backup material in case of manufacturing error.

Figure 70

Aluminium flat bar geometry figure

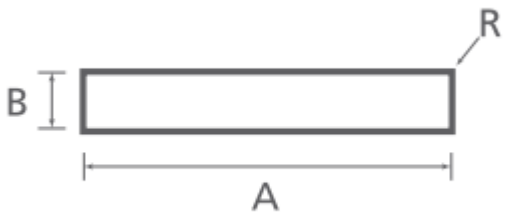

3.3 Manufacturing and assembly

This section introduces the manufacturing and assembly process. Figure 71 shows the aluminium joints were under manufacturing process. The CNC machine manufactured all the aluminium parts. Figure 72 shows the manufactured aluminium parts.

Figure 71

The aluminium parts were manufacturing by the CNC machine

Figure 72

The manufactured aluminium parts

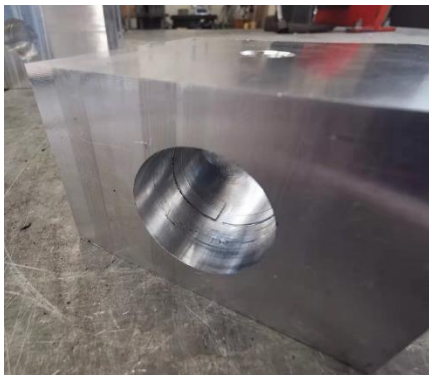

3.3.1 Adhesive bonding and surface treatment

The adhesive that will be used in this project is toughened epoxy adhesive. This adhesive is designed to bond composite materials and aluminium alloy. There were two types of adhesives, the HPR 5 and the HPR 25. Both two types of adhesives have liquid adhesive and two-part adhesive forms. The main purpose of the HPR 5 is to apply on the thin film region or a primer before applying another adhesive. The HPR 25 exceed the requirements of ASTM D1002, which is stronger than the HPR 5. Therefore, the HPR 25 was selected.

Table 7 describes the general information of the HPR 25 epoxy adhesive. There were two colours, black and white. The white colour was selected because the white colour paste can have a strong contrast to the silver aluminium joints and the black CFRP tubes. If some fractures show up in the adhesive layer, the white colour could make it clearer to present. Since the HPR 25 is a two-part adhesive. Part A is a clear paste, and part B is a white paste. The mix ratio is 4:1, and the adhesive requires four parts of part A and one part of part B. The pot life after the two parts is mixed is around 35 min. The adhesive should only prepare what is needed within the timeframe; otherwise, the adhesive will be wasted. The failure strength of the adhesive is around 15.9 MPa, and the failure mode described by the supplier is mixed (80% adhesion and 20% cohesion).

Table 7

HPR 25 epoxy adhesive's basic information

	HPR 25
Physical state	Black or White paste
Specific gravity (g / ml)	1.1
Viscosity (at 25 degrees Celsius)	5500
Mix ratio (pph)	25 pph
Mixed viscosity	140000
Pot life (100 g at 20 degrees Celsius)	35 min
Typical cure cycle	Seven days at room temperature
Ultimate performance cure cycle	6 hours at 6 degrees Celsius
Failure stress	15.9 MPa
Mode of failure	80% adhesion and 20% cohesion

Note. Typical properties and not to be construed as actual specifications

PPH = parts per hundred parts of resin

Figure 73 demonstrates the post-cure curve at different temperatures. The adhesive requires seven days to be fully cured at room temperature and only 24 hours in an environment higher than 40 degrees Celsius. The university's furnace is too small to store the test demonstrator, and the structure can only be kept at room temperature and let the bonded frame wait for seven days. The bonded parts can be moved around after being cured for one day. So, the experiment will be carried out after at least seven days of the last bonding process to ensure the adhesive structure can reach its optimal strength.

Figure 73

HPR 25 HDT progression with various cure cycles

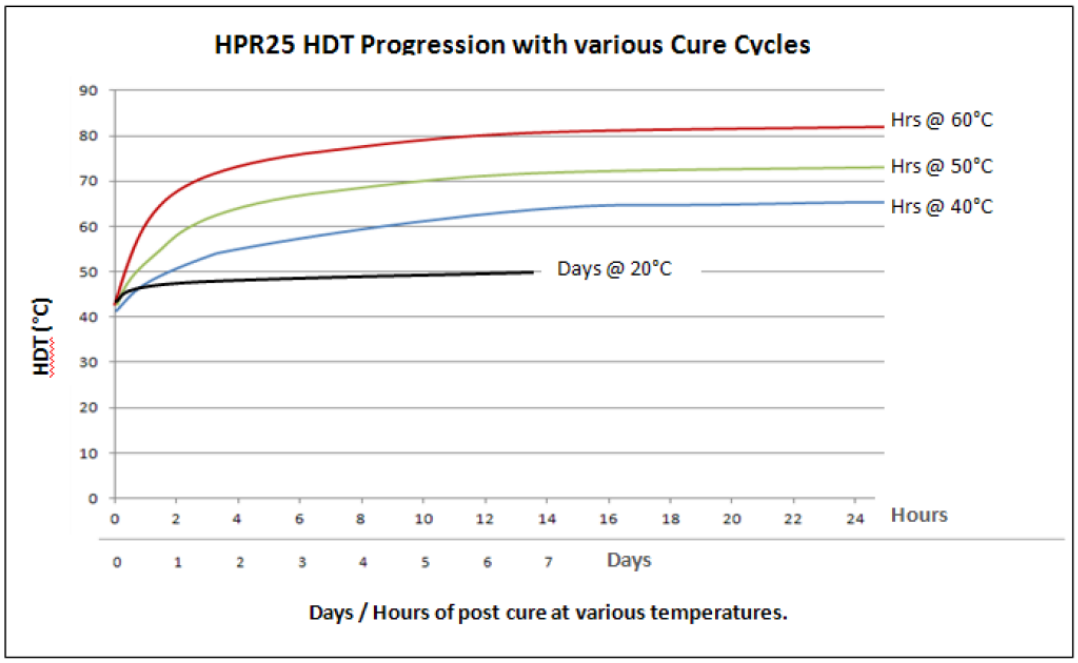

Figure 74 shows the adhesive was applied to some aluminium scraps for adhesive trials. Plastic spoons were used to take out the adhesive. The coloured wooden sticks were used to mix the adhesive. And the mixing process was undergone in the plastic containers. Brushes were used to apply adhesive on the aluminium joints at the beginning. But the trials showed the brush is not suitable for the job. The adhesive all sticks on the brush and won't be able to apply to the surface. The adhesive would move from the front of the brush to the back of the brush. The brush type is more suitable for using the liquid-type adhesive. After comparing brushes and wooden sticks, the wooden sticks were suited to apply the adhesives to the test demonstrators. Because the wooden stick is more solid, the stick can arrange the adhesive on the surface. Anything solid would be okay here.

Figure 74

Adhesive trial samples

The surface treatment process must apply to the CFRP tubes and the aluminium parts. The CFRP tubes conducted a sanding process, and the purpose was to change the bonding area to a matt finish. The sanded parts can provide a better bonding ability. Figure 75 shows all the CFRP tubes were drying after the washing process. The dust that remained on the CFRP tubes needed to be cleaned.

Figure 75

The CFRP tubes were drying after the washing process

During the assembly, the first surface treatment step is to use the 220 grid sandpapers to polish the surface of the parts. This step aims to remove the dirt and other substance on the product surface. And the aluminium parts' surface has a thin oxidation layer. The oxidation layer will reduce the adhesive shear stress (M.H. Khan et al., 2016). Therefore, the oxidates must be removed before bonding. During the CFRP tubes' sanding process, water must be applied to the sandpaper to prevent the carbon dust from floating around. Carbon fibre is harmful to the human body. Appropriate PPE, such as gloves, safety goggles, and N95 grade masks, must be worn. The oxidation layer must be removed before applying the adhesive since the oxidation layer will significantly reduce the bonding strength. The second step is to clean the sanded surface by using ethanol. The ethanol is safe to use and will vaporize fast. This step aims to wash out all the dust and powders caused by the sanding process. The adhesive must apply to the joints immediately after vaporising the ethanol because the aluminium surface will oxidate fast and re-form another oxidation layer. The treated surface must remain untouched after the treatment process to avoid further contamination.

3.3.2 Test demonstrator assembly.

Figure 76 shows a large engineering square assembled by two aluminium beams. The beams were holden by the G-clamps on the workshop bench. A metal 90-degree engineering square was used to assist the two beams in forming a 90-degree angle. This setup can help the test demonstrators maintain an approximately 90-degree angle of each part. And the additional G-clamps can be used to hold the bonded parts on the aluminium beams during the curing process.

Figure 76

A large engineering square assembled by two aluminium beams

The surface treatment process must be applied during the assembly process before bonding all the parts. Figure 75 shows the first assembly process. The first groups of products are six sets of the long-bonded structure formed by two aluminium joints, two aluminium holding blocks, two short CFRP tubes and one long CFRP tube.

Figure 77

The first assembly process

Figure 78 shows two sets of long structures built first for the trial production. Four clamps clamped them onto the aluminium beam to keep them straight and prevent the bonded parts from loosening before the adhesive was fully cured.

Figure 78

The trial production

Figure 79 shows the rest of the four long structures had been clamped onto the aluminium beam. The clamp must not be set to as tight as possible. The excess clamping force would cause the structure to deform before the structure was fully cured. The first two trail structures have a small deformation at one of the joints, around one degree off the horizontal axis. The bonded structure must be examined carefully after the clamping process. A wooden hammer was used to help adjust the bonded structure during the clamping process. It can knock down the deformed parts, and the strength of the clamp needs to be adjusted to let the bonded structure maintain a 90-degree angle. The bonded parts need to be cured at least one day before being touched and moving around.

Figure 79

The rest of the four long structures were built

Figure 80 shows the second assembly process. The second process is to connect two long bonded structures with two short CFRP tubes. A total of three sets of the structure were built and clamped together.

Figure 80

The second assembly process

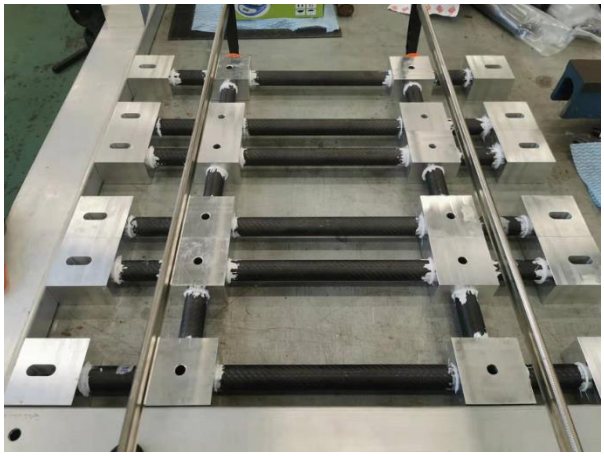

Figure 81 shows the third assembly process. Two side aluminium holding blocks were bonded to the structure built in assembly process two. Due to the available bench area limitation, only two structures were built at first.

Figure 81

The third assembly process

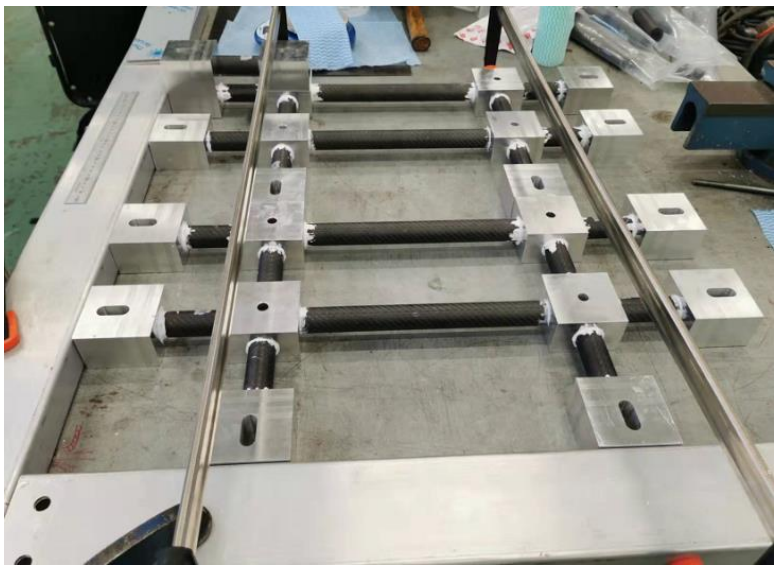

Figure 82 shows the final assembly process. All the parts were bonded together. Only one structure was allowed to process each time, and the structure was allowed to remove after at least one day. Then, allow the last built structure to be placed safely for seven days before putting them onto the physical experiment.

Figure 82

The final assembly process

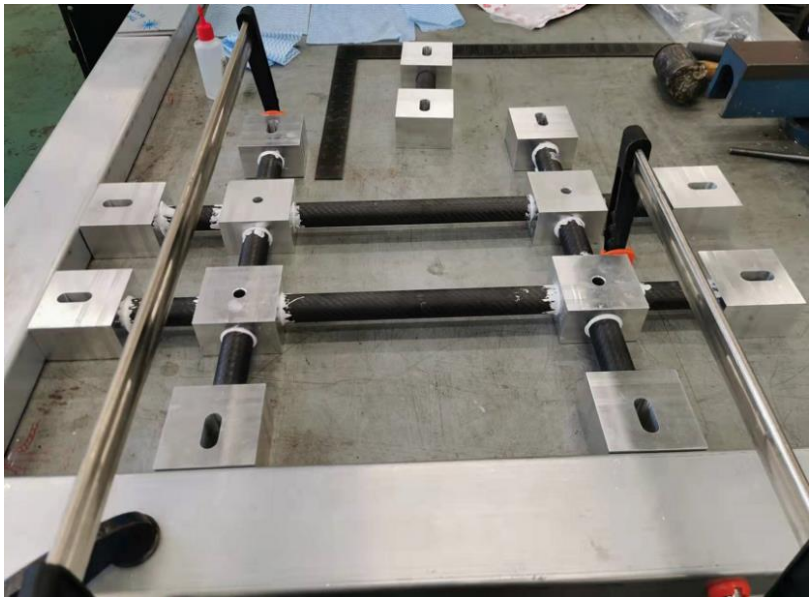

3.4 Test facility setup

The test demonstrator's size is too large to fit in the standard tensile test machine. Thus, a test platform must be established to conduct the physical tests. The test platform requires a larger frame and actuator to operate. Figure 83 shows an available yellow frame. The frame's height is four meters. Figure 84 shows the actuator used to conduct the pulling-up test. The actuator is hydraulic powered, and its loading capacity is 250 kN which is higher than the required test loads (See Appendix C1 for detailed actuator data). Figure 85 demonstrates the brief assembly CAD drawings. The CAD drawings show the actuator's attaching points and the yellow frame's position.

Figure 83

Four meters yellow frame

Figure 84

The actuator will be used in the experiments

Figure 85

The CAD drawing of the actuator's position on the yellow frame

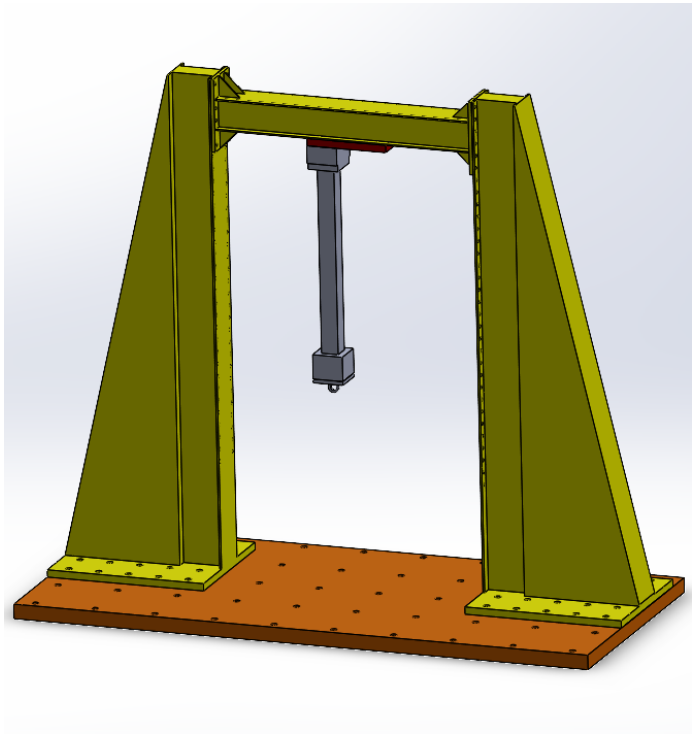

The test demonstrator must attach to a base structure since it cannot directly attach to the ground. Figure 86 displays the parts used to support the test demonstrators. It is built with two red column structures and two red plates. Two red plates are secured to

the red columns by the M36 bolt and nuts. An additional adopter plate is required to hold the test demonstrators.

Figure 86

The base structure

Because the test demonstrator's pulling point is not located at the centre, the position of the adopter plate and the actuator must be calculated carefully. Figure 87 shows the adopter plate's dimension. The steel adopter plate's dimension is 850 mm x 528 mm x 20 mm. It will provide enough space to attach the test demonstrators. Based on the calculation of the minimum thread length of the M12 screws, 18 mm is required (See Appendix 7). The minimum standard steel plate is 20 mm; it can meet the safety requirement. No additional surface treatment process is required because the adopter plate can only hold the test demonstrators. The material of the steel adopter is G250 steel. The test demonstrator will be secured to the eight M12 tapped holes. Four large rectangular hollow sections provide free space for the installation of aluminium joints, nuts and bolts. The hollow section's area is much larger than the aluminium joints. The purpose is to leave enough space for the installation process. If the three test demonstrators' M12 bolt positions cannot fit into the same location, new M12 tapped holes need to be prepared. The current hollow section area can satisfy the test demonstrator if it is required to shift to the left or right for a new position. The test demonstrator's pulling point is located at the centre of the base structure.

Figure 87

The CAD drawing of the steel adopter plate

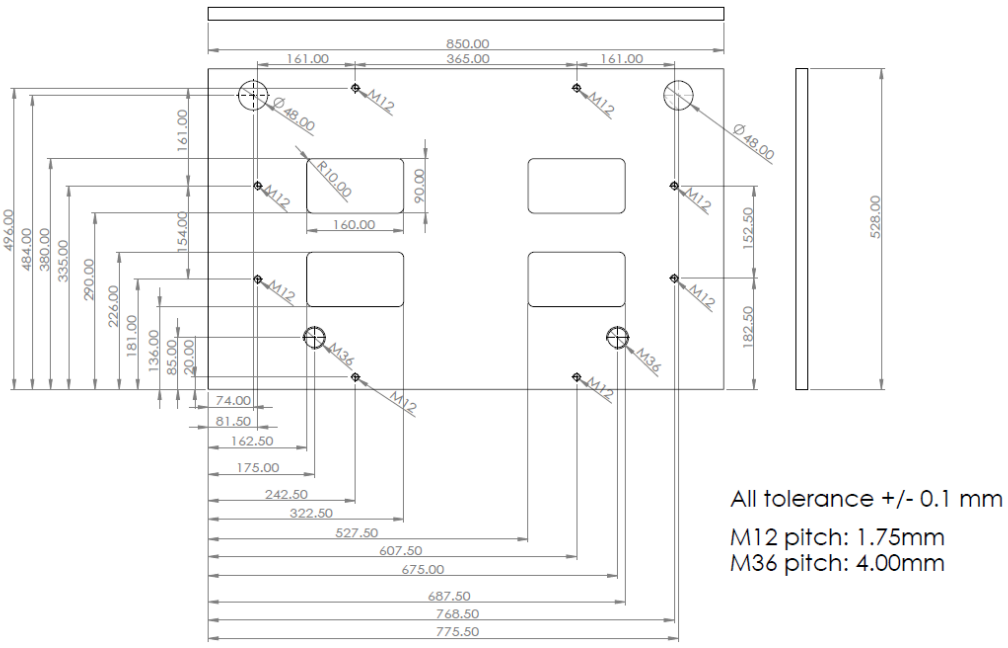

Figure 88 shows the steel adopter plate's attaching plan. The m36 tapped holes and the M48 clear through-holes are used to connect with the base structure. The M36 tapped holes are closed to the test demonstrator's attaching points, and the nut will influence the test demonstrator's installation. So, the bolt was changed to a threaded rod, which will be secured by a nut at the bottom of the base structure. M42 threaded rods will be used to secure the base structure and the steel adopter plates. Since this hole's position won't affect the test demonstrator's attaching position, they don't require a tapped hole, and the nuts can be placed at the surface of the adopter plate. Sufficient clear space is provided to tighten the M42 bolts and other parts.

Figure 88

The CAD drawing of the steel adopter position

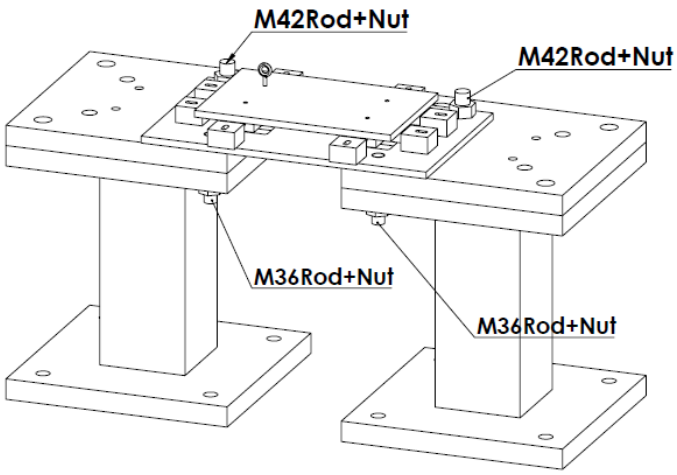

The actuator needs an additional steel plate to connect an eyebolt to pull the test demonstrator. Shackles and steel chains will be used to connect the actuator and the test demonstrators. Figure 89 shows the steel plates that will attach to the actuator. The dimension of the steel plate is 250 mm x 250 mm x 32 mm. All five threaded holes are M24 size with a 3 mm pitch. The standard bolt used to hold adopter plates onto the actuator is the M24 bolt. The eyebolt in the centre was also selected as an M24 bolt to reduce the manufacturing process. Only one type of threaded hole is needed on the entire plate. The M24 eyebolts exceed the current test's loading requirements and can be used in other projects once this project is finished. The 32 mm thickness of the steel plate provides sufficient threaded length to fit the M24 eyebolts.

Figure 89

The CAD drawing of the steel plate

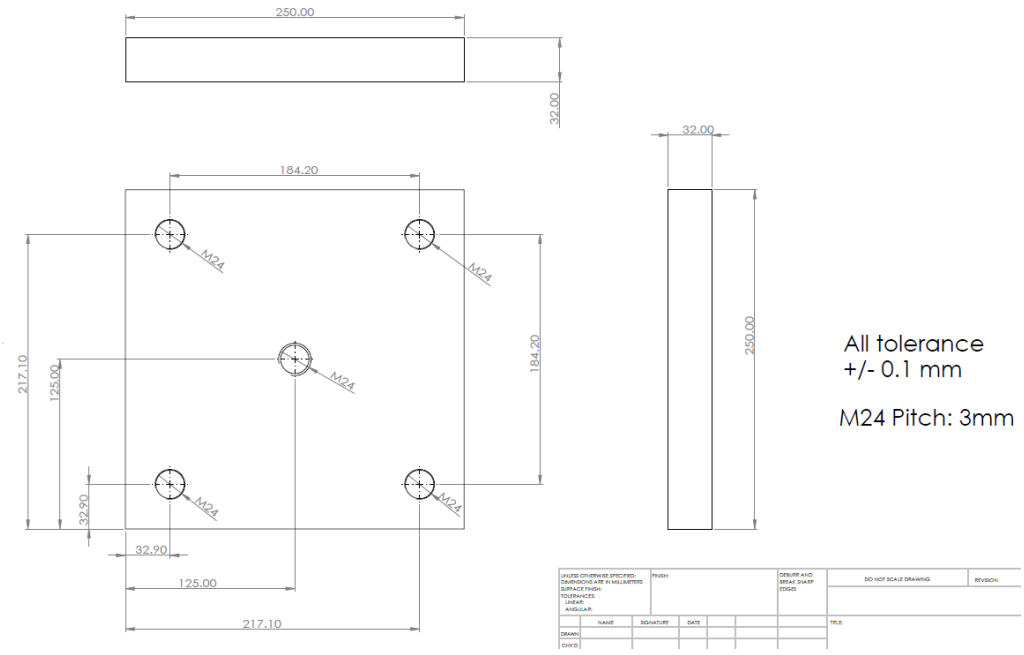

Figure 90 demonstrates the final test platform setup plan. The glass protections are required to protect people from splashed pieces during the experiments.

Figure 90

The final experiment setup

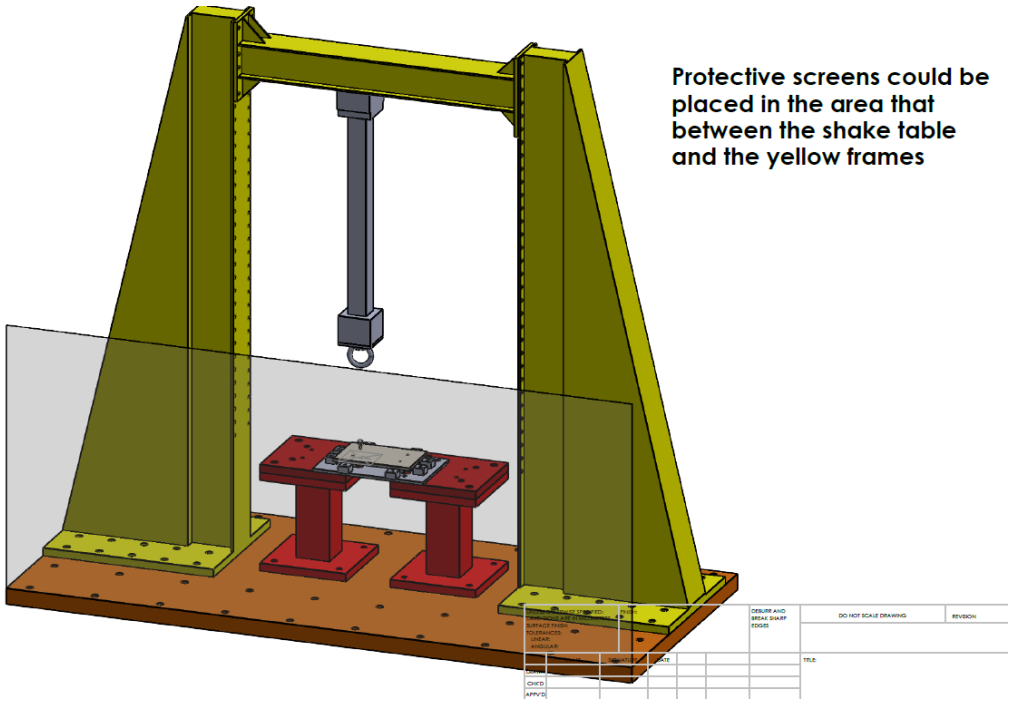

3.5 Strain gauges setup

This section illustrates adding strain gauges to measure the adhesive-bonded hybrid structure's strain during the physical test. The strain gauges will be set on the aluminium joints and the CFRP tubes. The main purpose is to monitor the strain change during the tensile test. The strain gauge configuration used on the test demonstrators includes the half-bridge strain gauge configuration and the quarter bridge strain gauge configuration.

Plan 1: Use Rosette strain gauges. Figure 91 indicates a standard rosette strain gauge configuration. It is assembled by three standard strain gauges placed on the same film. Three strain gauge represents three directions, 0-degree, 45-degree and 90-degree angles. Even the rosette strain gauges contain three strain gauges on the same film, and they still need to form three quarter bridge connection to monitor all the strain gauges. This setup's only benefit is simplifying the connection process for multi-direction requirements, and the entire setup can be bonded only once instead of three separate strain gauges.

Figure 91

Rosette strain gauge for axial strain setup.

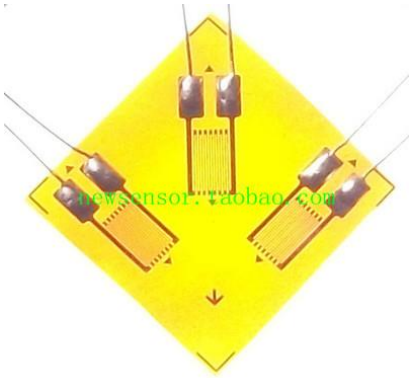

Two rosette strain gauges will be placed on the aluminium joints. Figure 92 shows the position of the rosette strain gauges. All the blue rectangular figures below represent the rosette strain gauges' position.

Figure 92

The rosette strain gauges will be placed in the blue area

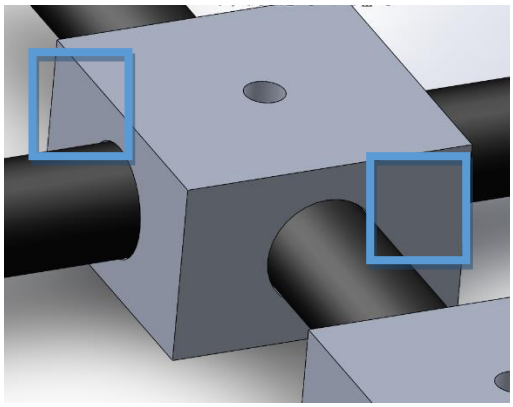

Vishay Precision Group (2014) states that the standard application uses 120 Ohms with a 3 mm gauge length to measure the aluminium joints. 350 Ohms is recommended in most cases if they are available for selection. But the rosette strain gauges only have 120 Ohm types available from the supplier, and smaller resistance means less accuracy. Therefore, a second plan is built to provide a better monitor result.

Plan 2: Use linear strain gauges. Since the standard rosette strain gauge is the same as attaching three separate strain gauges in the same direction, three linear strain gauges can be used to form a rosette configuration. The installation process is more complicated than using one rosette strain gauge. But 350 Ohms strain gauges with 6 mm gauge length can provide better accuracy for the monitored results. Figure 93 shows three standard 350 Ohms strain gauges from a rosette strain gauge setup.

Figure 93

Use three linear strain gauges to form a rosette setup

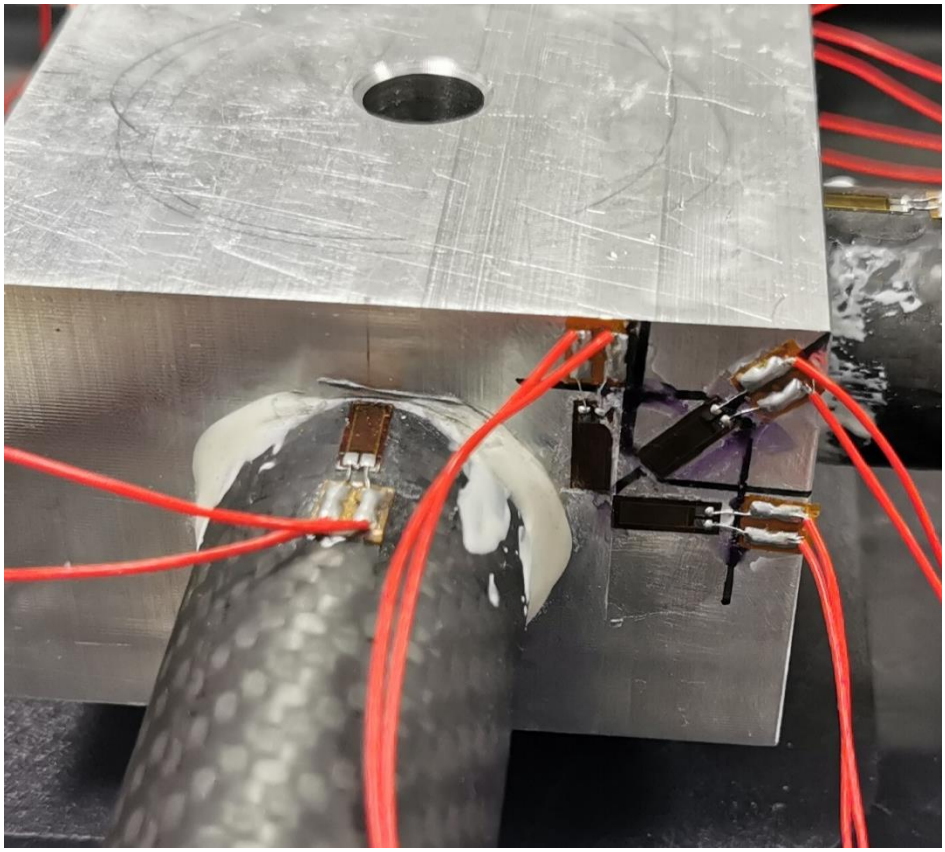

The standard application of strain gauges is 120 or 350 Ohms with a 3 mm gauge length. Usually, using longer strain gauges for non-homogeneous materials such as concrete and composite materials is recommended. Some manufacturers specified using a 5 mm or 6 mm strain gauge for composite materials measurements. The longer gauge length will provide less noise and better accuracy. Furthermore, 350 Ohms strain gauge performs better than 120 Ohms and is recommended to measure composite materials. In this case, the strain gauges used on the CFRP tubes will be the same as those used on the aluminium joints. Only one type of strain gauge is required. Table 8 displays the detailed information on the selected strain gauge. The 350 Ohms with 6mm, gauge length strain gauge was selected.

Table 8

The detailed strain gauge information

Model	BF350-6AA		
Size	Basal size	mm	10 x 4 mm
	Wire grid size	mm	6 X 2 mm
Basal material			Phenolic-epoxy
Sensitive to grid material			Constantan
Resistance	The nominal value of tolerance	Ω	350.1±0.2Ω
	The average devition	Ω	≤0.4Ω
The use of temperature			(-30℃-80℃)
Gauge factor and dispersion			2.11±1% (20.-2.2 ±1%)
Thermal output	Heat output coefficient	um/m/℃	≤2
	Scores of average heat output	± um/m	≤30
Greenhouse strain limit		um/m	20000
Greenhouse insulation resistance		MΩ	10000
Mechanical lag		um/m	1.2
Strain limit			2%
Fatigue Life			≥ 10^7 (±1000)

In the first strain gauge set-up plan, four half-bridge strain gauges will be placed in the CFRP tubes, as shown in Figures 94 and 95. Each configuration will include two strain gauges, one attached to the top of the CFRP tube and the other one will be placed at the bottom position. This plan is to measure the points where the largest deformation may occur. When the CFRP tubes were under pulling up force, they were treated as the cantilever in the initial analysis. The cantilever is fixed by one end, and the other side is a free end under loading. When the beam breaks, it will break at a location near the fix-end point. The half-bridge configuration can be changed to three quarter-bridges to reduce cost, and the quarter bridge can satisfy the basic requirement for measuring bending. However, the half-bridge strain gauges are more sensitive than quarter-bridge strain gages and have a better temperature advantage.

Figure 94

Half-bridge strain gauge setup (top view)

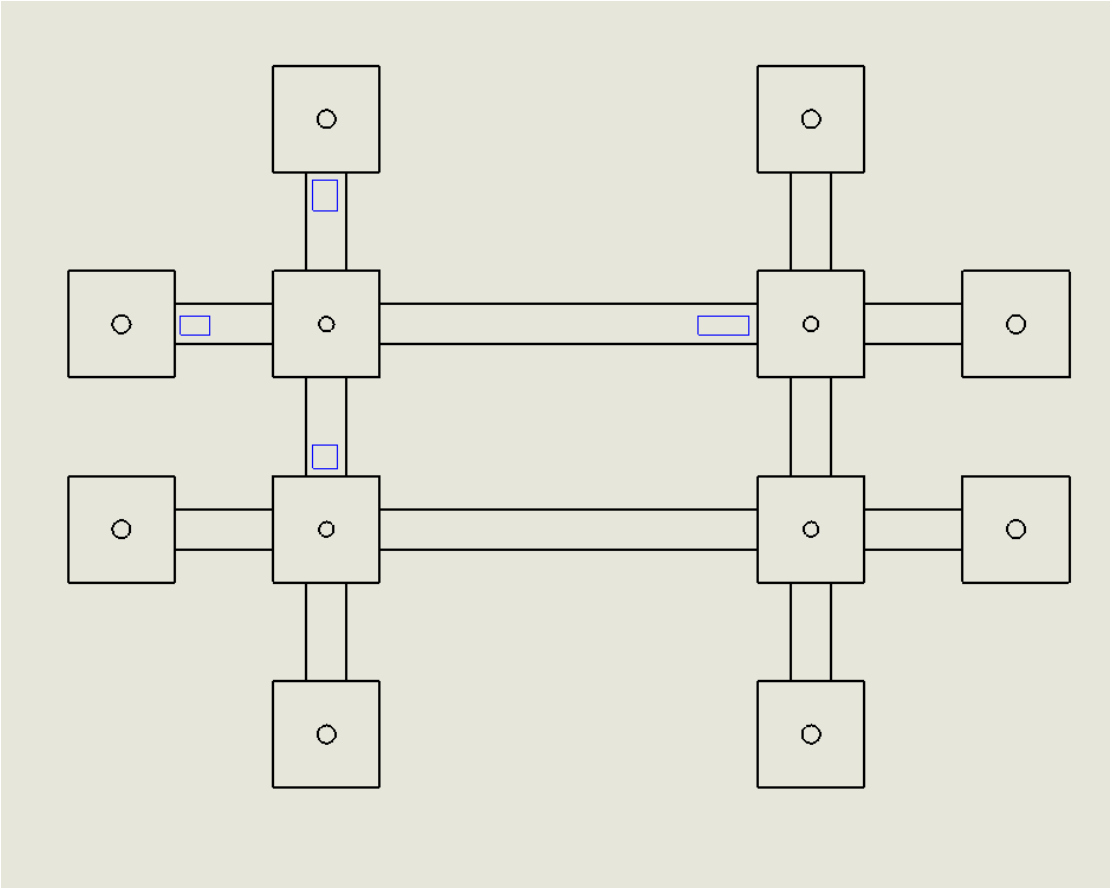

Figure 95

Half-bridge strain gauge setup (side view)

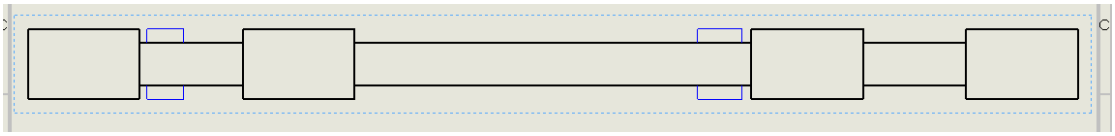

But the free end in the structure is bonded with the aluminium joints. The complete structure is much more complicated than a cantilever. If the CFRP tubes break in the experiment, they might break at the position shown in Figure 93 and close to the joint block under load, shown in figure 96. More positions should be monitored to provide more results.

Figure 96

New measure plan

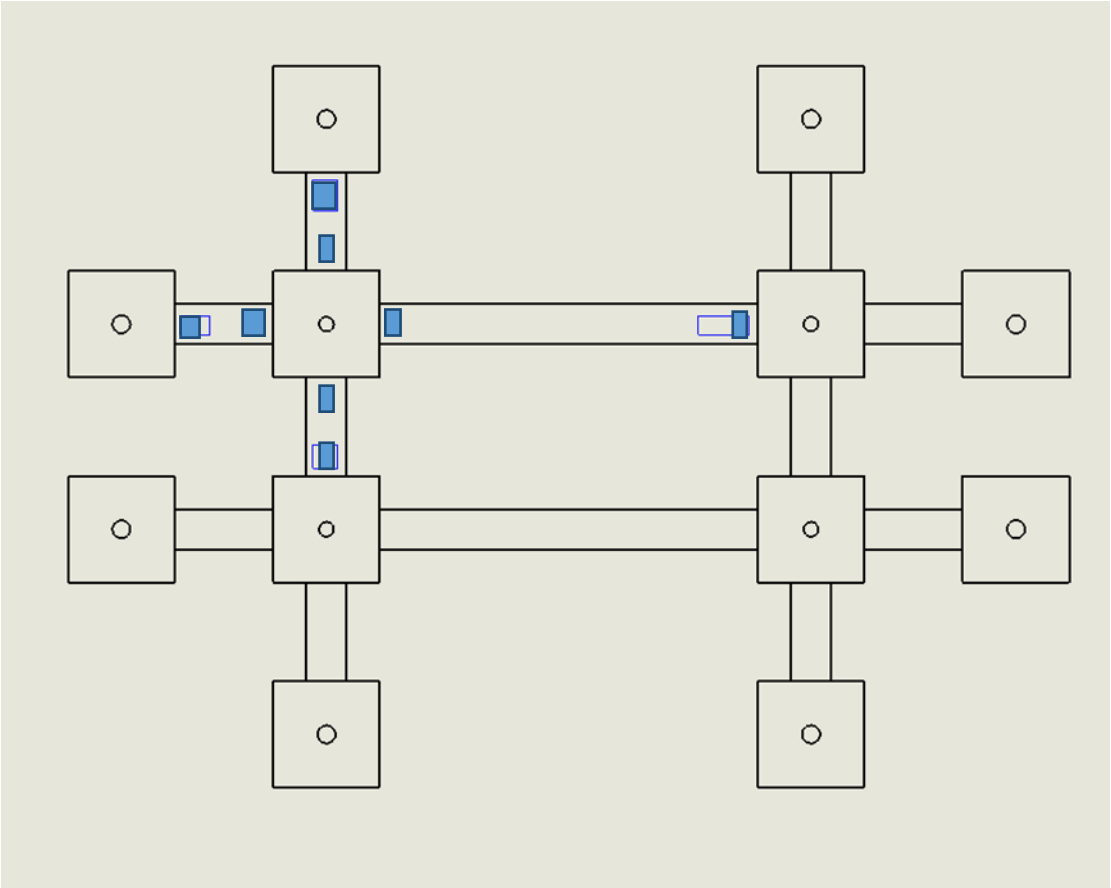

Figure 97 displays the final plan's configuration of the CFRP tubes, modified based on the second plan. The only difference was two strain gauges were moved to the red rectangular position. The reason for making this change is to investigate the behaviour of the structure at the far end position that is away from the pulling points. The largest deformation was believed to occur in the green zone shown in figure 8, which surrounded the pulling points (yellow rectangular zone).

Figure 97

The final strain gauge layout plan

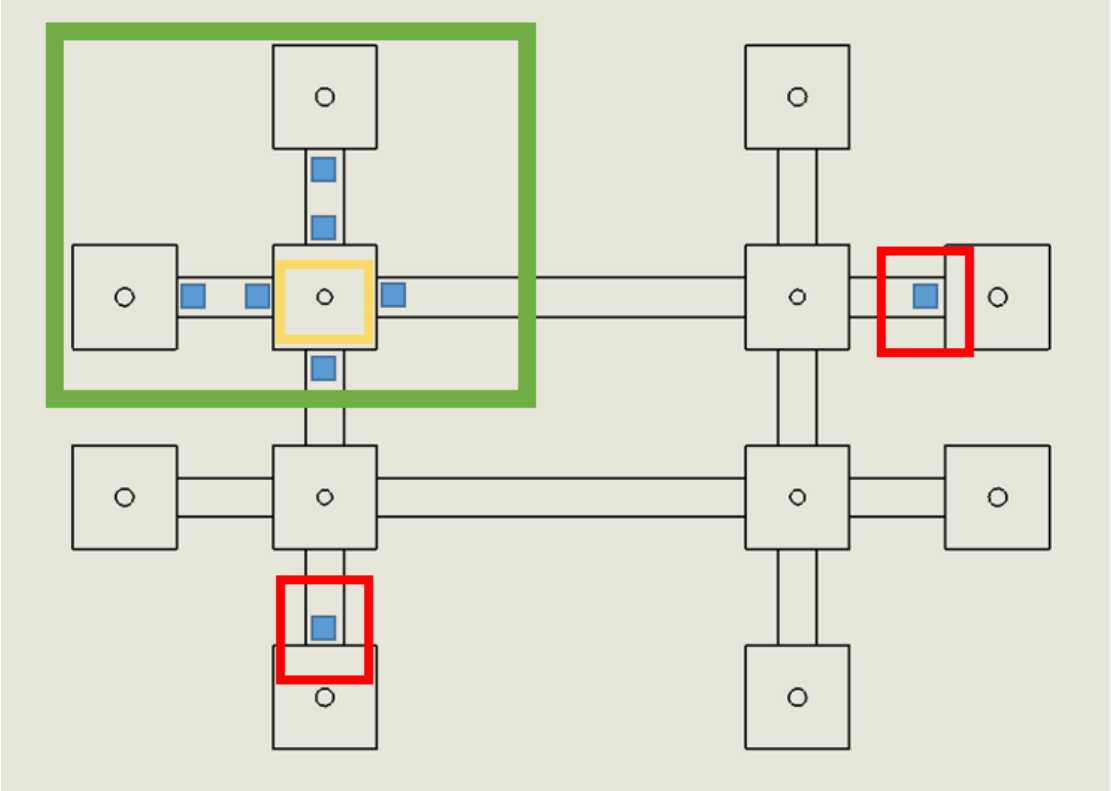

All the strain gauges need a Wheatstone bridge circuit to connect to the PC to provide signal feedback. Figure 98 displays the circuit board used to build a Wheatstone bridge connection to all the strain gauges. The circuit board is an RJ-50 PXIe strain gauge bridge interface. The R4, R3, R2 and R1 position connects with the strain gauges and the resistors.

Figure 98

RJ-50 PXIe strain gauge bridge interface

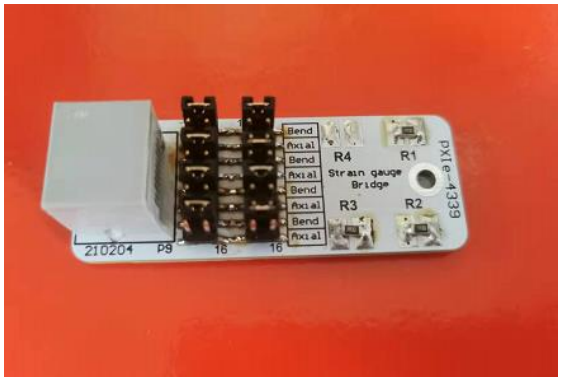

The Wheatstone bridge circuit needs active strain gauges and resistors. Only R4 will connect with one strain gauge to form a quarter bridge configuration, and the constant resistor will connect with R1, R2 and R3. R4 and R3 will connect with one strain gauge to form a half-bridge configuration, and the constant resistor will connect with R1 and R3. To make a balanced Wheatstone bridge circuit, the constant resistors' resistance must equal the strain gauges' resistance. The balanced Wheatstone bridge circuit's voltage output is 0 since there is no current flow (Bolton, 2015). The surface mount resistors were selected, but no 350 Ohms resistor is available. Two resistors can connect parallel to form a resistor close to 350 Ohms. The 390 Ohms and 3300 Ohms resistors were selected, and the equivalence resistance is 347.98 Ohms. The error is only 0.57% which is acceptable. See Appendix A8 for detailed calculations. Figure 99 shows the 3300 Ohms surface-mount resistors used in this experiment.

Figure 99

The 3300 Ohms surface mount resistors

Karuppasamy et al. (2019) state the strain gauge attaching steps as follows:

1. The surface of the target objects should be sanded and cleaned before attaching the strain gauge. The purpose is to remove the dirt that remains on the surface.
2. The clear tape can be used to assist in attaching strain gauges. Stick the surface of the strain gauge onto the clear tape and then locate the strain gauge onto the measuring point. After finding the right location, do not stick the clear tape and the strain gauge on the surface.
3. After locating the measuring points, apply a small amount of super glue to the back of the strain gauge. Super glue can bond the strain gauge to the object's surface.

4. Bond the strain gauge on the measuring point and apply pressure on the strain gauge for around two minutes.
5. Remove the clear tape carefully and slowly to prevent the clear tape damage the installed strain gauge.

Figure 100 displays the strain gauges installed on the CFRP tubes and the aluminium joints.

Figure 100

The installed strain gauges

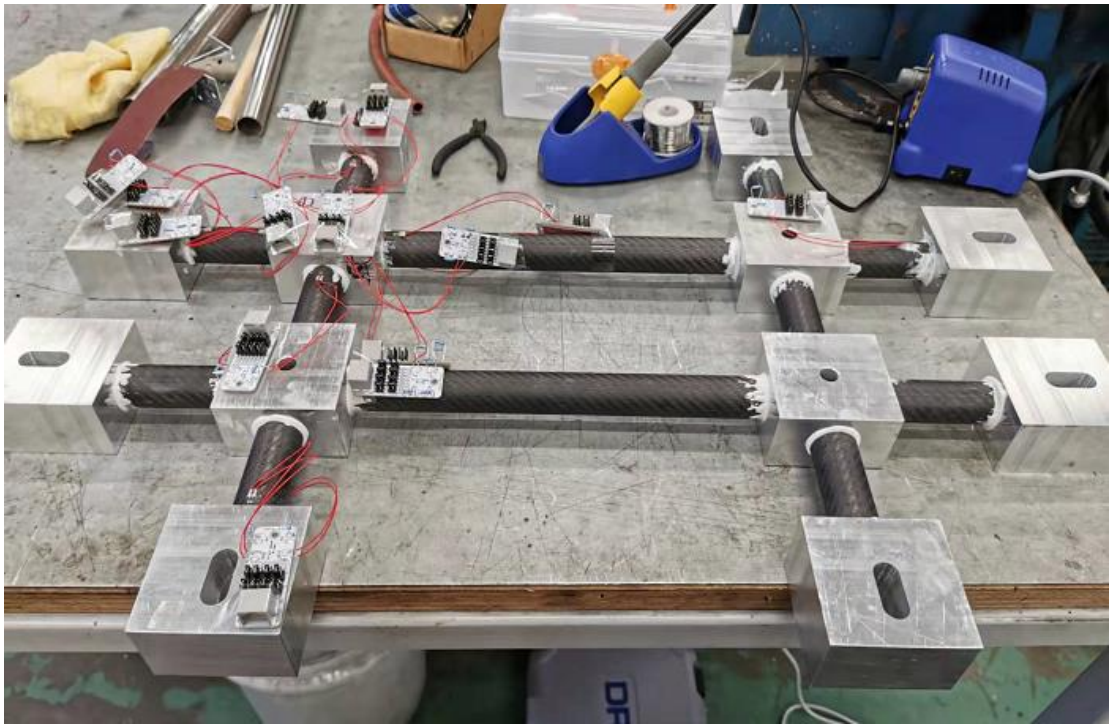

3.6 Experiments setup

This section introduces the test layout and setup. A total of three tests were conducted. The first experiment is a trial test. The purpose is to check the experiment setup and if there are any improvements to make. The second experiment will stop immediately after the first failure is detected. The detection method observes the significant strain change through the data acquisition system, and the joints break sound. Crack noise can be heard when the adhesively bonded joints were failed. The third test is a destruction test. The test demonstrator will be destroyed.

3.6.1 The test demonstrator and the test platform layout

Figure 101 shows the dimensions of the technical demonstrator. Figure 102 shows the actual test demonstrator. A total of three sets were built. Figure 103 shows the CAD drawing of the paper panel. The M12 eyebolt replaced the M10 eyebolt. The M12 eyebolt has better strength and could fit into the bolt hole of the aluminium joints. The bolt hole on the aluminium joints is 12 mm.

Figure 101

Technical demonstrator's general dimensions

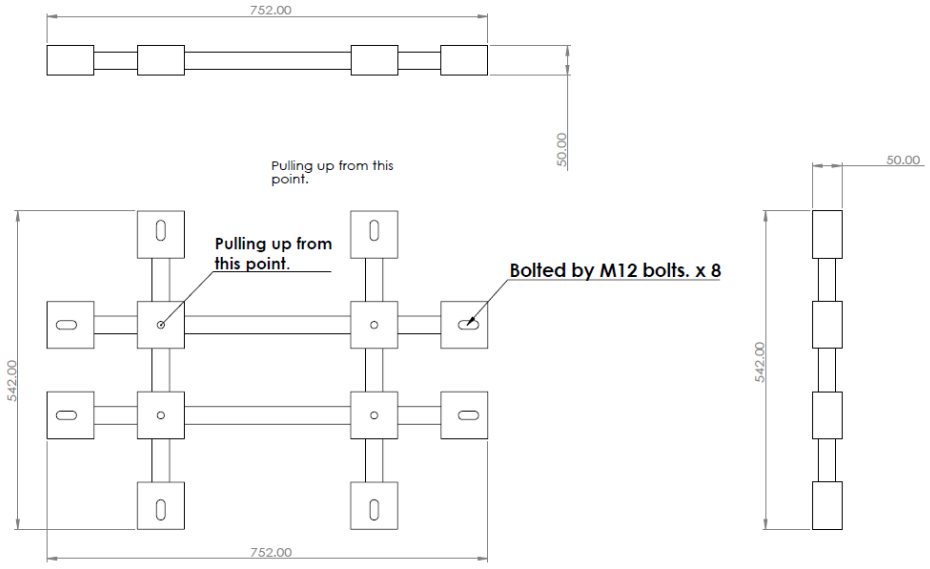

Figure 102

Photograph of the technical demonstrator test frame

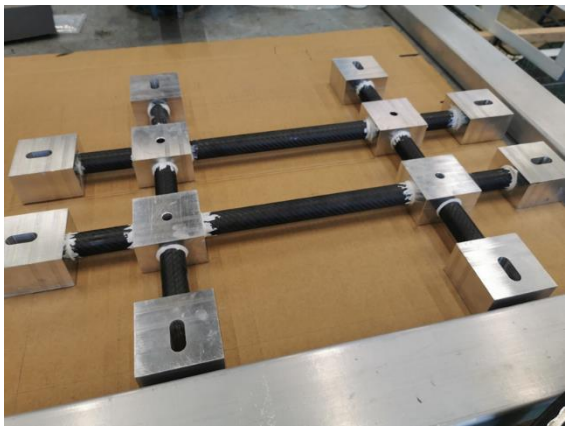

Figure 103

The drawing of the paper panel

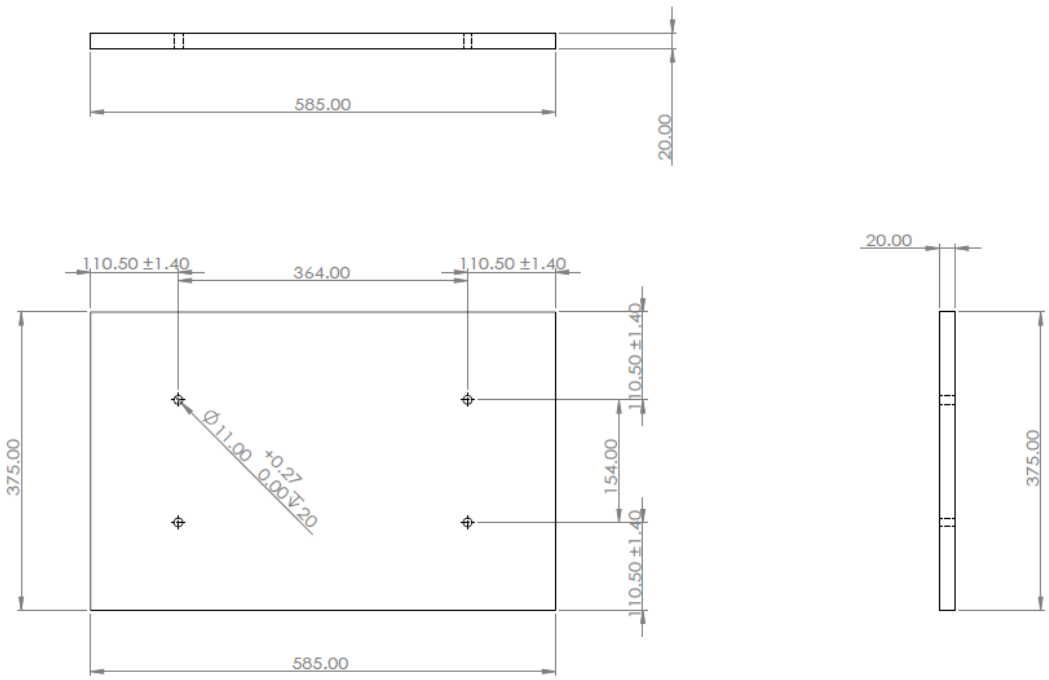

Figure 104 shows all three test demonstrators were stacked together. The paper panel was placed on the top, and three eye bolts joined the aluminium joints' bolt hole. The test demonstrators' dimensions and holes' positions were accurate.

Figure 104

Three test demonstrators were stacked together

Figure 105 shows the test demonstrator was placed on the steel adopter plates. All three test demonstrators can fit into the same position.

Figure 105

One test demonstrator was attached to the steel adopter plate

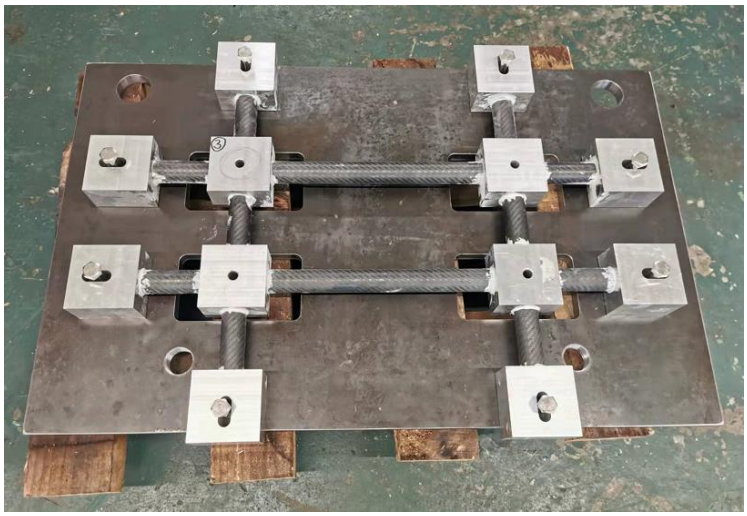

Figure 106 shows a half-bridge strain gauge configuration attached to a spare CFRP tube. The purpose was to check whether the strain gauges work on the tube parts. A simple hand bending test was conducted, and the data acquisition system captured readings. Therefore, the strain gauges can work on the CFRP tubes. Figure

Figure 106

The trial strain gauge test

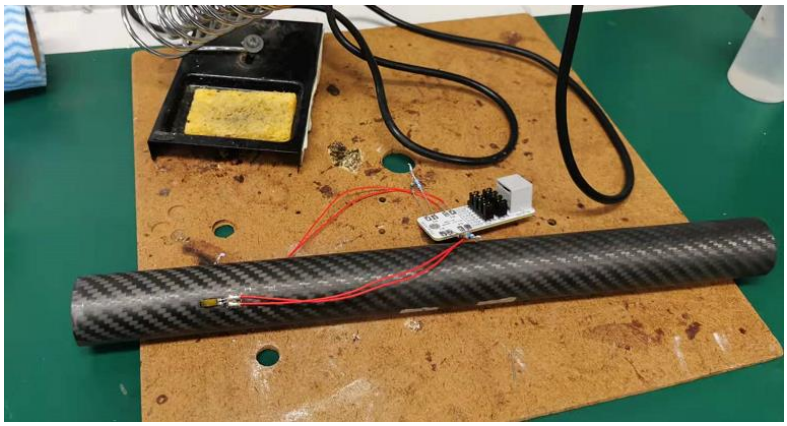

Figure 107 shows the strain gauges were under examination. All the strain gauge was checked; only one cable was used.

Figure 107

Strain gauges were under examination

Figure 108 shows how the test demonstrator was connected to the data acquisition system. Double-side sponge tapes attached the statin gauge circuit boards to the steel adopter plates.

Figure 108

Photograph of the technical demonstrator with attached strain gauges and controller connectors

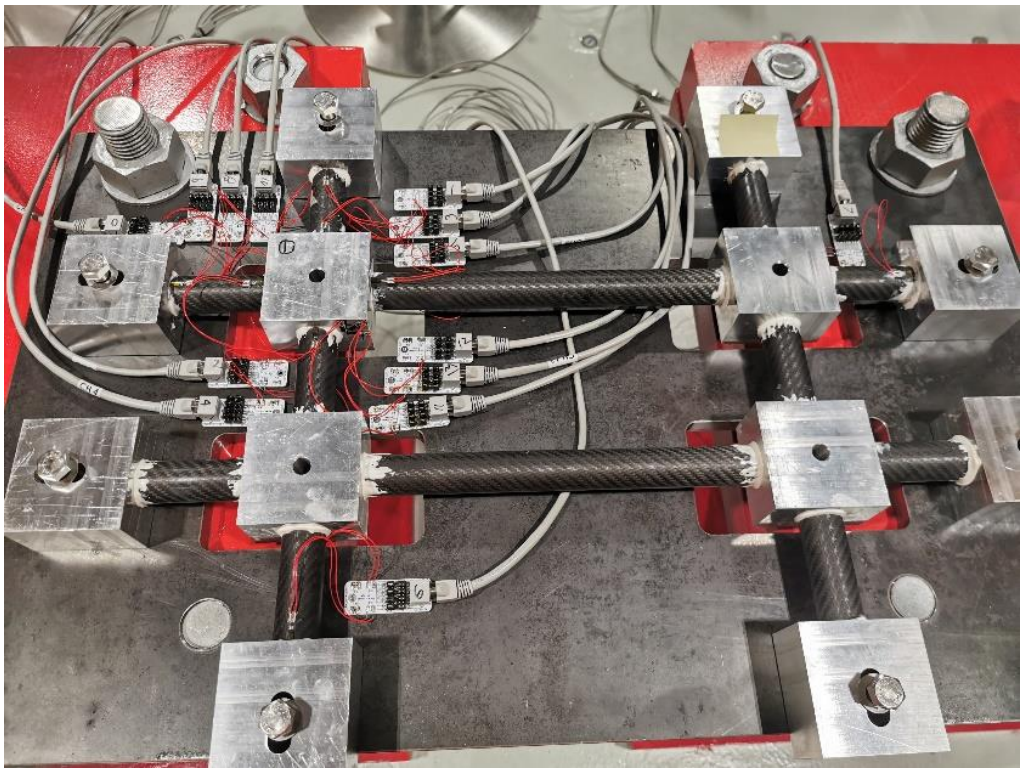

Figure 109 shows the test platform layout, including the test frame, actuator, and data acquisition setup (controller). Clear protectors were placed between the test platform and the controller.

Figure 109

Test platform layout and experiment setup

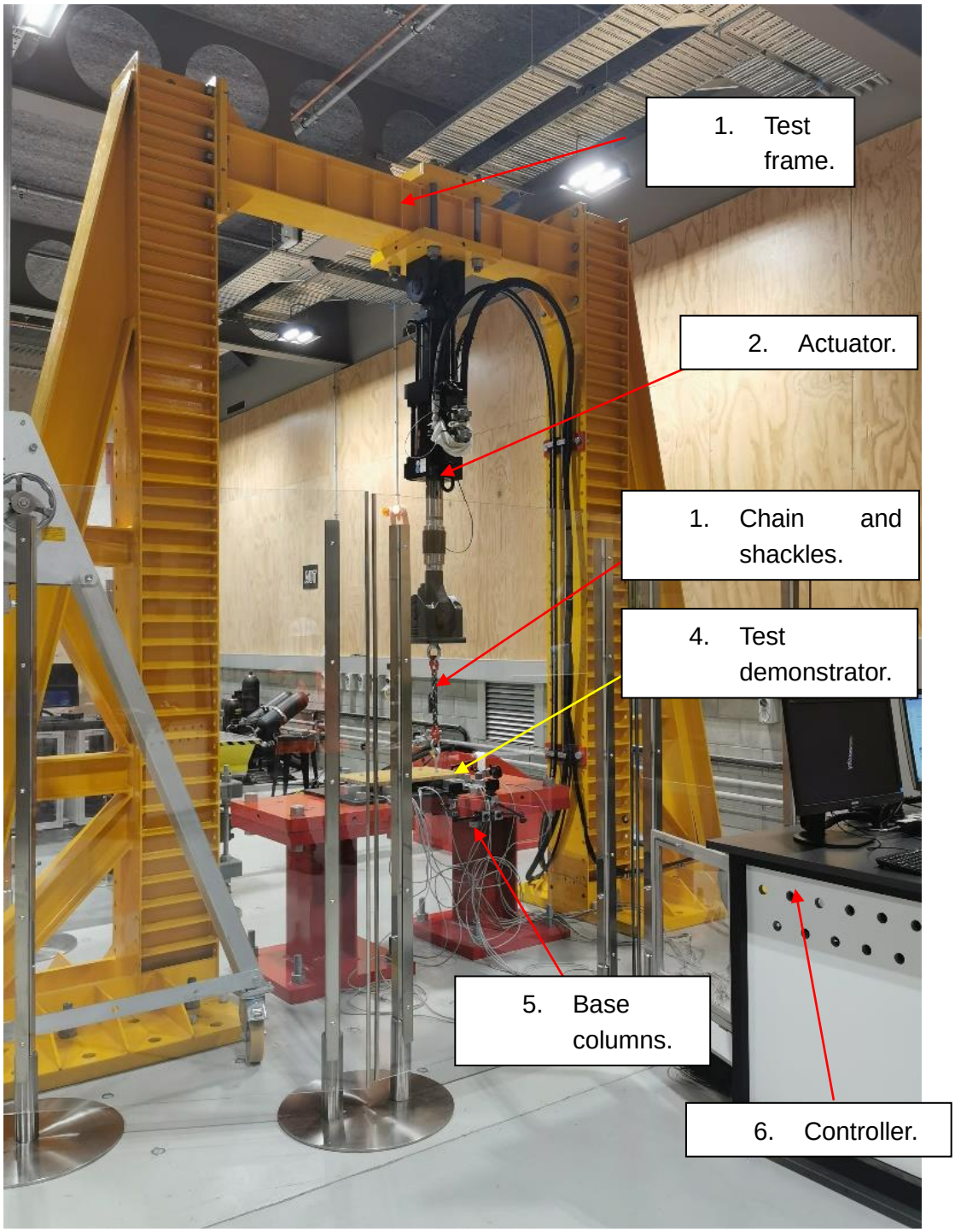

3.6.2 Three tests' details

Figure 110 displays the photo of the first test. The first test is a trial test. Three go pro cameras were set around the test demonstrator to record the CFRP tubes' deformation. The actuator test speed was 0.5 mm per minute. The slow speed was selected for the first trial. Figure 111 shows the data recording system. The recorded information included strain data, deformation, and applied force.

Figure 110

The first test's photo

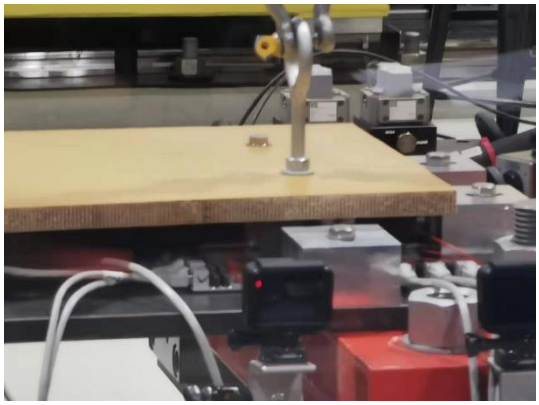

Figure 111

The control system

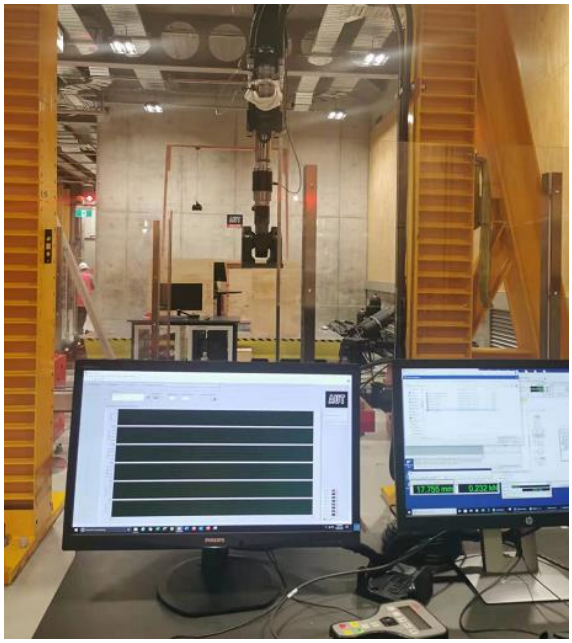

Figure 112 illustrates a level added to the second and the third test demonstrator for monitoring the structure deformation. The paper panel was removed for the second and third tests. Figure 113 shows the cameras were monitoring the level and shackle connection. The Go-pro cameras can have a better monitor angle after removing the paper panel. And the purpose of using one of the cameras to monitor the shackle connection was to record any movement that affected the strain gauge data.

Figure 112

A level was added to the second and the third test demonstrator for monitoring the structure deformation

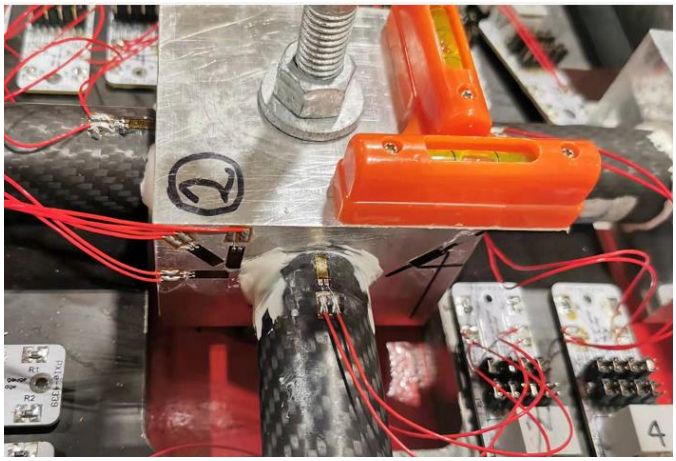

Figure 113

New camera monitoring plan for the second and the third trials

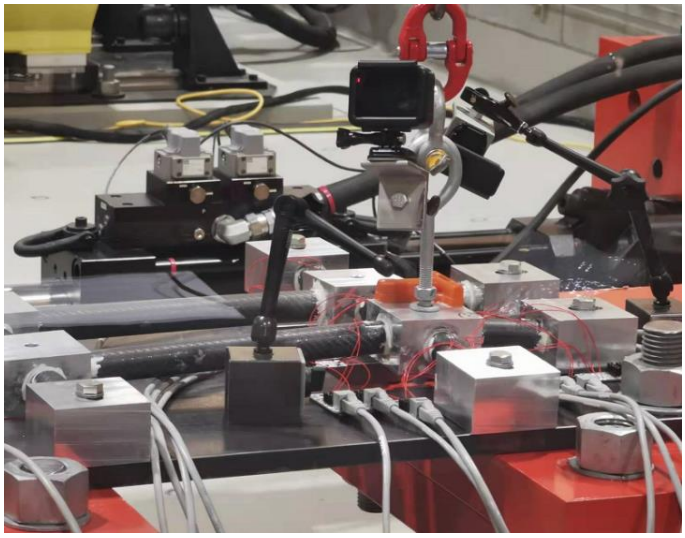

3.7 FEA analysis setup

This section introduced the FEA simulation process. The FEA analysis was conducted by SolidWorks. There are two methods to simulate the composite material. The first method simulates the CFRP tubes using the 'Shell Manager' function. This function could define the object into multiple composite material layers in different directions. Since the supplier only supplied the carbon fibres' properties and the CFRP tubes' data. This method cannot be used due to the lack of the composite laminator layer's data.

The CFRP tube will be treated as an isotropic material in the simulation process. The most important data for analysis of the strain change is the young's modulus.

As shown in figure 114, the FEA model only contains the test demonstrator itself. All the other parts were removed for simplified the simulation process.

Figure 114

The CAD models were used for the FEA study

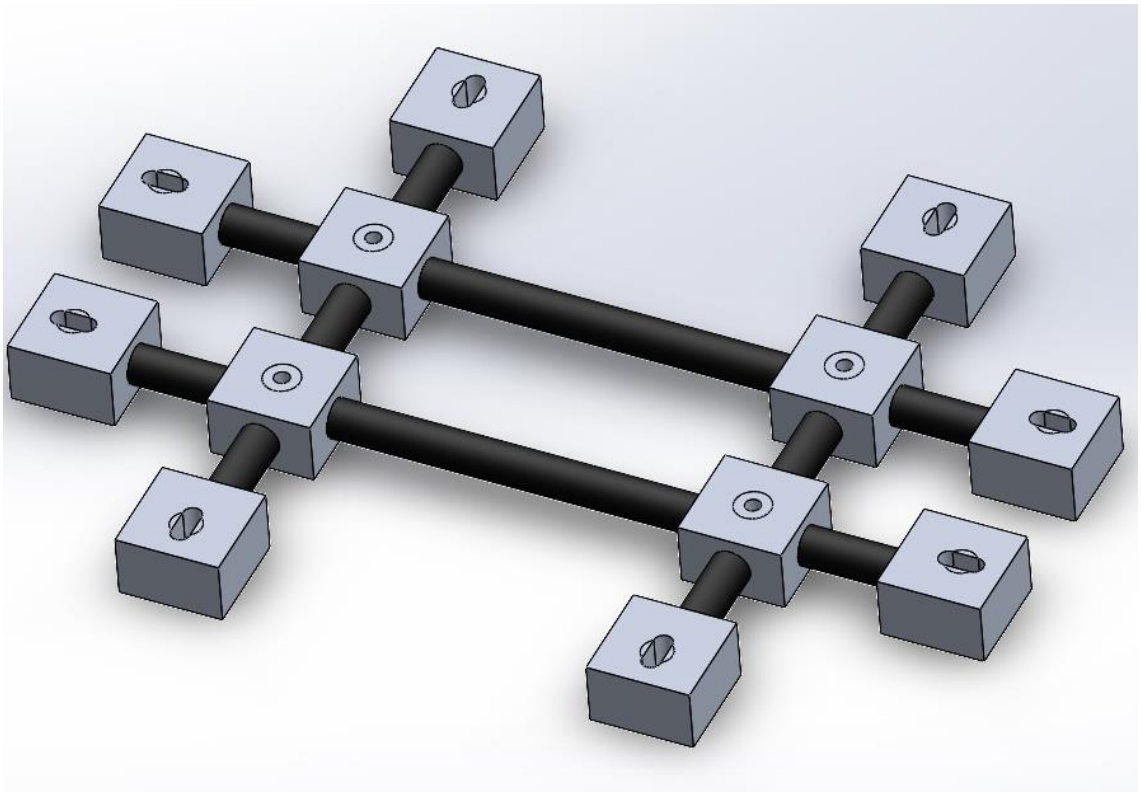

Figure 115 illustrates the force application area. All the load was applied to the washer under the pulling point's aluminium joint in the real experiment. The washer was removed to simplify the CAD models, and around an area with an identical area had been created. The force will apply to this area. 'Split line function' was used to create this area, so the load can only define in this area.

Figure 115

The force application area of the 3D model

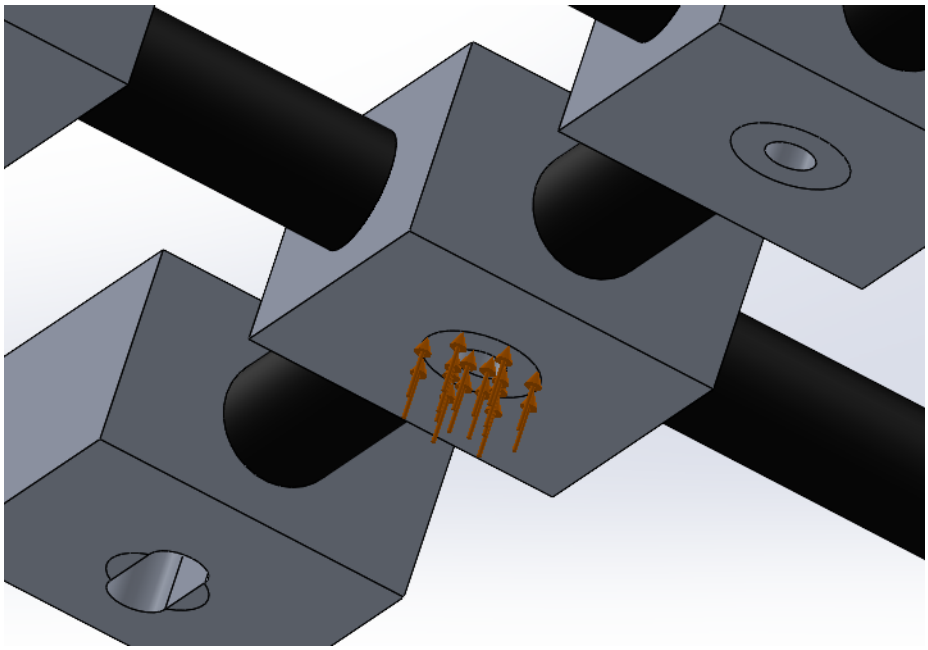

Figure 116 shows the fixtures of the CAD model. The bottom of the aluminium holding block was defined as the fixtures because these eight holding blocks were secured tightly during the experiments. The eight aluminium holding blocks were secured by screws and washers during the physical tests, as shown in figure 4. The actual fixing points should be around the bolt hole area. Defined the entire bottom surface eliminates all the deformation of the holding blocks, affecting the simulation results' strain behaviour. A refined fixture definition had been established. Figure 4 shows the fixture of the new CAD model fixture arrangement. The fixtures were defined on the eight holding blocks. Screws and washers secured the eight aluminium holding blocks during the physical tests. The' split line function' created the washer area around the bolt holes on each holding block.

Figure 116

The fixtures of the CAD model

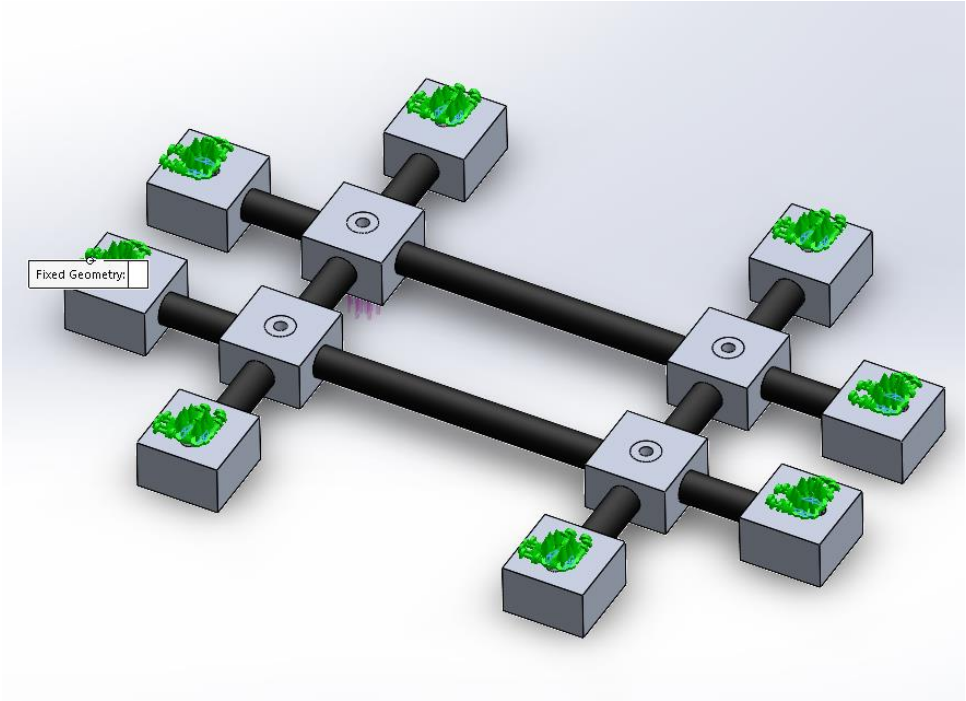

A mesh refinement process was conducted. The mesh size was simulated from 8 mm to 2 mm. And as shown in figure 117. The error was only 1.6 per cent, which was small. The 4 mm mesh option was selected for the simulation because the strain gauge's width was around 4 mm. The strain data point can be identified easily.

Figure 117

The mesh refinement results

Test 2	Force	Mesh	Strain
	7000N	8	1.01E-03
		7	1.00E-03
		6	1.02E-03
		5	1.01E-03
		4	1.02E-03
		3	1.02E-03
Error			1.60%

Seven simulations had been conducted, and the force was the only difference between each test. The forces used in the simulation started from 1000 N and then increased another 1000 N until the total loading reached 7000 N. Test 1 had an unexpected chain movement that caused the valid strain data to stop around 4000. Test 2 and test 3's adhesive layers started the first break after 7000 N loading.

The general simulation process:

1. Select static linear study.
2. Define the fixtures of the model.
3. Define the loading area and force.
4. Create mesh (4mm).
5. Run the study.
6.

The strain data was retrieved from the central location where the strain gauge was attached. The strain gauge's centre point coordinates were recorded before starting the simulation. Each data points have a unique element number, and the element on the recorded coordinates will be selected for data recording. The element number must be recorded, and the same element number will be used in the following simulations. The function used to retrieve strain data is the 'Probe' function, shown in figure 118. The strain recorded in the physical experiments were normal strains, so the simulation's strain data must be defined in the same direction. When selecting the strain data location, the simulation result must switch to the right normal strain result.

Figure 118

The 'Probe' function for retrieving the strain data

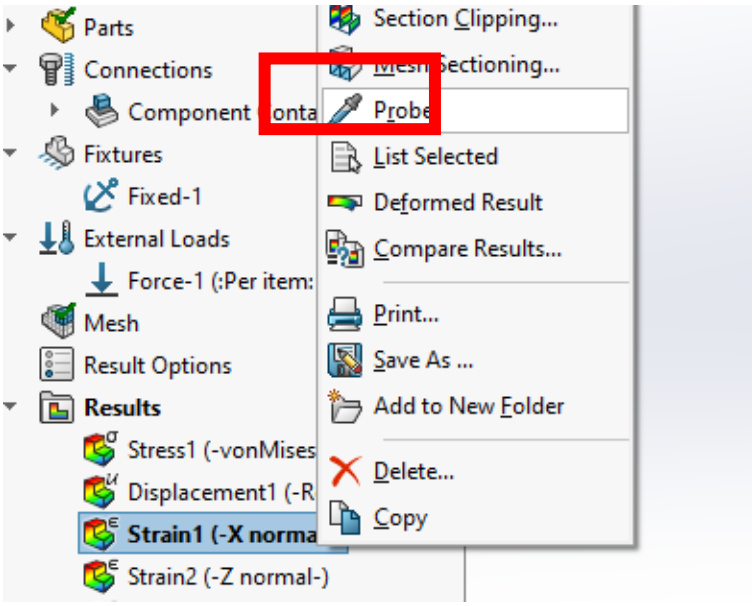

The strain recorded in the physical experiments were normal strains, and the strain data must be selected from the same direction in the simulation. When selecting the strain data location, the simulation result must switch to the right normal strain result. For example, strain gauge 9 measured the Y-axis's normal strain, and strain gauge 11 measured the Z-axis's normal strain. When the result function was set to Y-axis's normal strain (strain gauge 9), strain gauge 11's location's element number can not be recorded. The element number in SolidWorks' Y-axis's normal strain result group differed from the Z-axis's, and even the location shared the same coordinates.

Chapter 4 Results and discussion

This chapter summarized the results from the three tests and the FEA analysis. The first test demonstrator was cut for the failure mode evaluation. The strain data were recorded and compared with the SolidWorks FEA study.

4.1 Strain data

Figure 119 illustrates the strain gauge application layout. Strain gauges 1 to 8 were in half-bridge configurations (attached two active strain gauges, one on the top of the CFRP tube and another at the opposite position). They were placed where the CFRP tubes joined with the aluminium joints. The purpose was to monitor the bending from the CFRP tubes where the maximum displacement and a higher chance of a break may occur. Strain gauges 9 to 14 were quarter bridge configurations (only one active strain gauge) placed on the aluminium joints. Strain gauges 9 to 11 and 12 to 14 formed two rosette setups. The setups were made by three quarter-bridge configurations and placed in 0^o, 45^o and 90^o. The purpose was to monitor the small changes in the aluminium parts and any unexpected stress changes during the experiments.

Figure 119

Strain gauge application layout

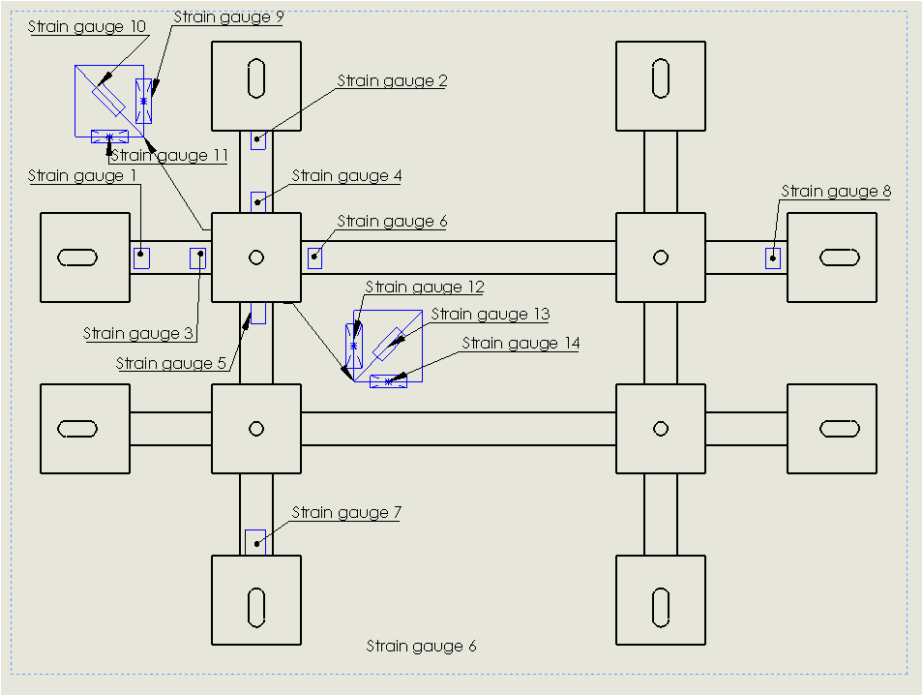

Figure 120 illustrates the load pattern recorded for 38 minutes by the load cell, and a total load of 30.8 kN was applied to the demonstrator in this test. The test speed of the actuator was 0.5 mm per minute. The total displacement of the demonstrator was 17.5 mm.

Figure 120

Test 1 actuator load data

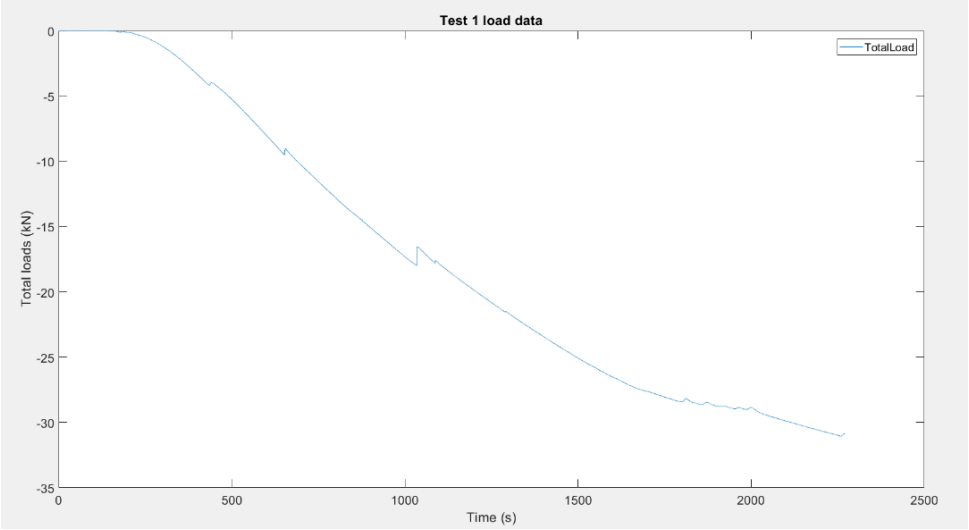

Strain gauges 1 to 8 were placed on the CFRP tubes. Strain gauges 3, 4, 5, and 6 were placed on the tubes close to the pulling points, and the results had an upward trend (tension), as shown in Figure 121. Strain gauges 1, 2, 7, and 8 were placed on the side away from the pulling points, and the results output had a downward trend (compression), as shown in figure 121. The bridge type was a half-bridge configuration, one strain gauge placed on the top of the CFRP tubes and another set at the opposite position.

Figure 121 illustrates three major changing trends before the load reached 20 kN. The first one was in the blue highlighted rectangular area, the second was in a red highlighted rectangular area, and the third was in the green highlighted rectangular area. The first one occurred at 436 seconds (7.26 minutes). There were some minor changes in the relative strain data. The applied force was 4162 N. The second one occurred around 652.5 seconds (10.875 minutes), and the applied force was 9149 N. The third one occurred around 1035 seconds (17.25 minutes), and the applied force was 17013.4 N. In the first blue rectangular area, all eight strain gauges indicated a similar change compared to the second and the third rectangular area. All the strain change was identical and small, and the reason caused this could be the physical position change of the chain and shackle connection. The chain and shackles at the top slightly moved and affected the whole structure.

In the second area, strain gauge two showed a significantly larger change than the other seven strain gauges. Strain gauge two's behaviour indicated that joints experienced a significant deformation, which might be the first significant crack of the test frame. The tube debonded from the joints after being sectioned (see chapter 4.2).

Figure 121

Test 1 strain gauge data of strain gauges 2 to 8

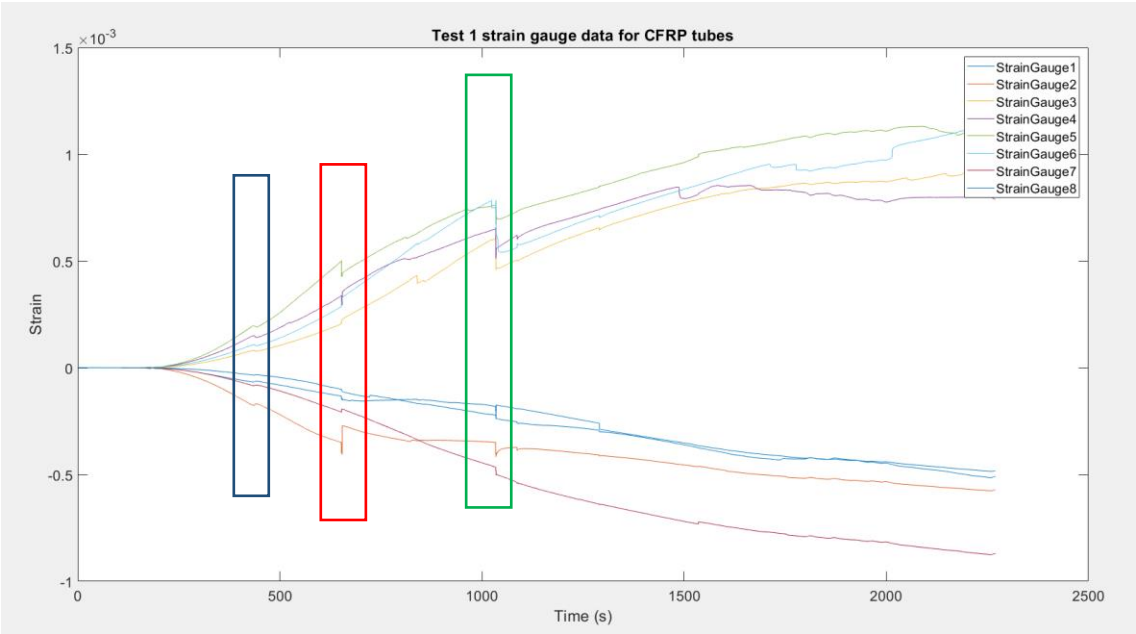

Note. Test 1 CFRP strain gauge data. Three rectangular shapes labelled the first three significant strain changes.

Strain gauge 9 to Strain gauge 14 were placed on the aluminium joints in a rosette configuration. Strain gauge 13 failed to give readings due to a connection error during this experiment. Figure 122 illustrates all the strain data from strain gauges placed on the aluminium joints. Three rectangular shapes had labelled the first three significant data changes. Strain gauge 10 suddenly changed (highlighted by the red arrow). Thus, the aluminium joint was still under load, and the adhesive was not yet broken. The second and third rectangular areas suddenly decreased due to the cracked adhesive layer. The strain gauge data explained that the first strain data change was caused by the movement of the structure or connection parts. The adhesive failure caused the second and third strain data changes, which indicated the failure started around 9 kN.

Figure 122

Test 1 strain gauge data of strain gauges 9 to 25 (aluminium joints)

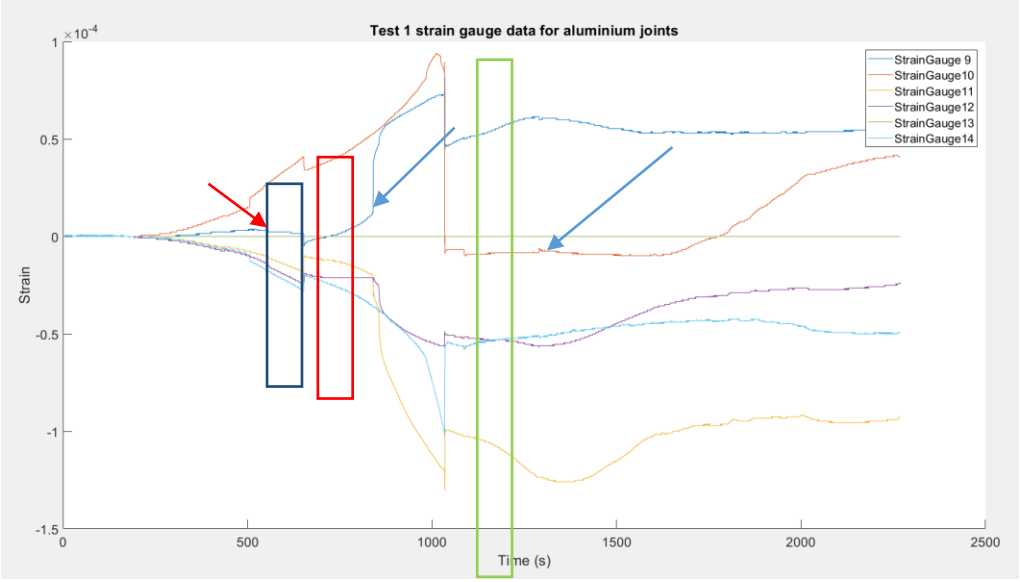

Note. Test 1 aluminium joints strain gauge data. Three rectangular shapes labelled the first three significant strain changes.

Figure 123 illustrates the total loads applied during the second test. The test speed increased to 2 mm per minute, and the load applied was around 12 kN. For the second test, the actuator was stopped after spotting the first joints cracked.

Figure 123

Test 2 load data

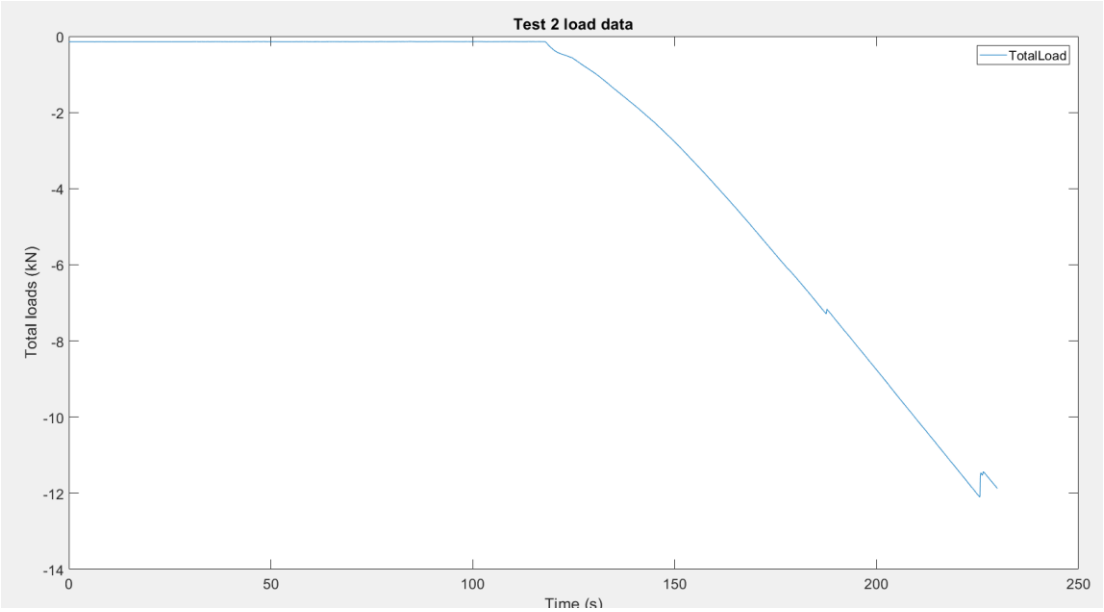

Figure 124 displays the second test's strain gauge data for the CFRP tubes. The green rectangular area indicates that the first joint break and load during the first break was around 7.1 kN. Strain gauge 2 shows the largest strain movement pattern, indicating that strain gauge 2 experienced the first joint break. This result matched the first test in which strain gauge 2's position experienced the first joint break.

Figure 124

Test 2 strain gauge data of strain gauges 1 to 8

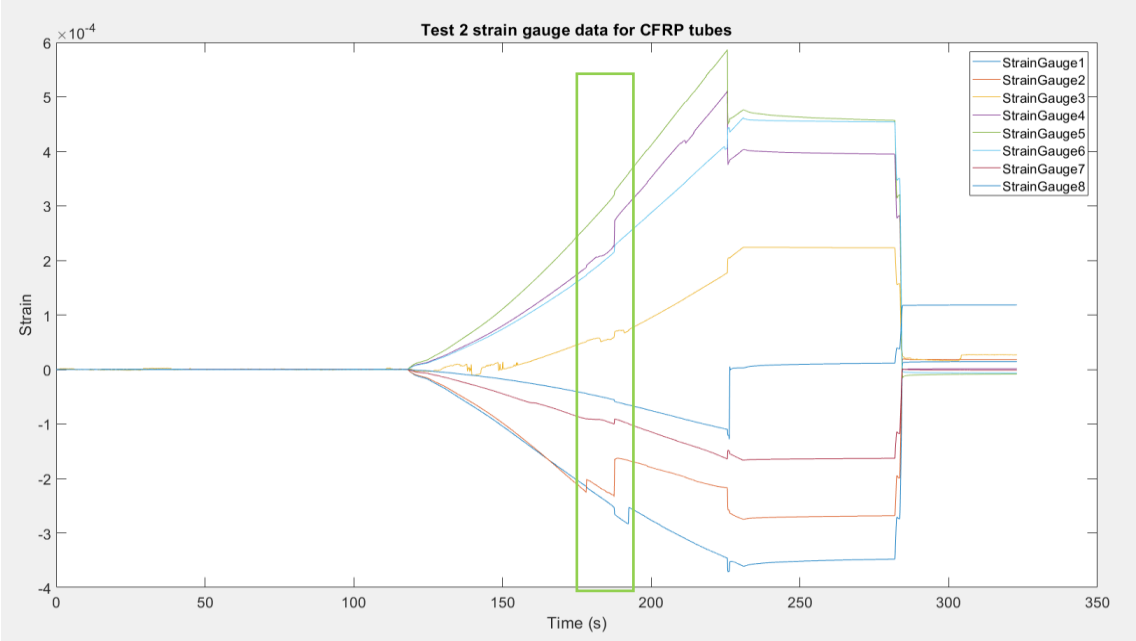

Figure 125 shows the data from the strain gauges 9 to 14 placed on the aluminium joint. The strain gauge data 12 is excluded from the figure since it had a very large strain change that makes all the other data look straight.

Figure 125

Test 2 strain gauge data of strain gauges 9 to 14 (aluminium joints)

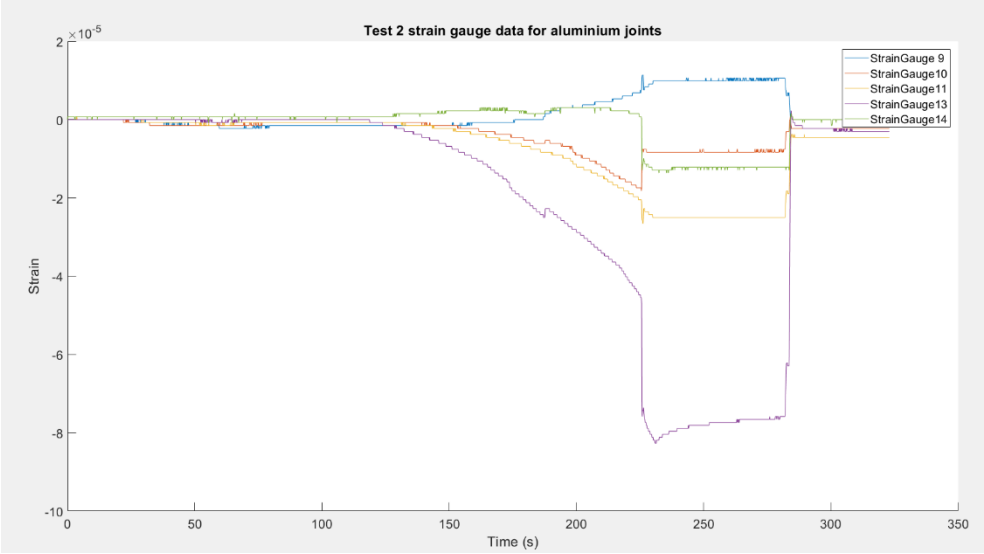

Figure 126 illustrates the total loads applied during the third test. The test speed is 2 mm per minute, and the load applied was around 40 kN. The third test was meant to destroy the third test demonstrator completely. But the load applied beyond the eye bolt's limit. The M12 eyebolt was broken during the third test. Figure 127 shows the broken eye bolts and the third test demonstrator. After the test, the test demonstrator looked fine, and none of the CFRP tubes was loosened from the aluminium joints.

Figure 126

Test 3 load data

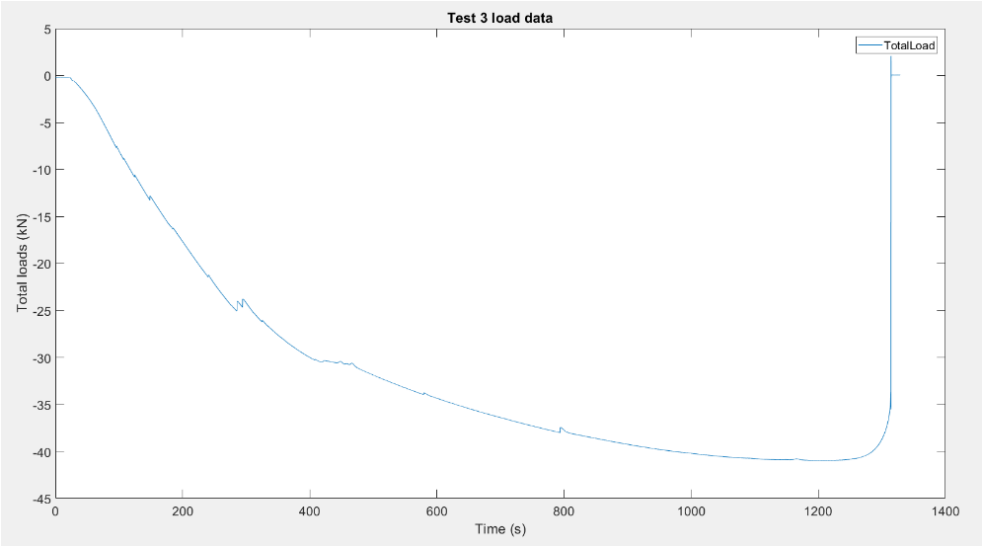

Figure 127

The broken M12 eyebolt and the third test demonstrator.

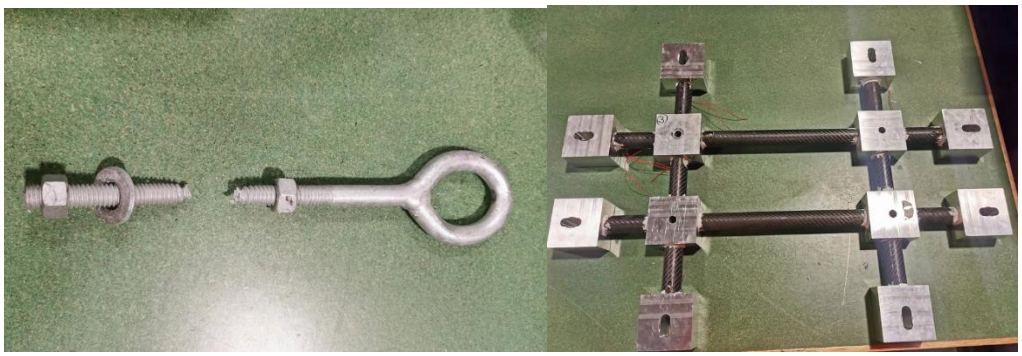

Figure 128 shows the third test's strain gauge data of the CFRP tubes. The figure only shows the first 150 seconds of data. The green rectangular area labelled the first joint break; the load was around 7.8 kN. Strain gauge two also had the largest strain change, matching the first and the second test.

Figure 128

Test 3 strain gauge data of strain gauges 1 to 8

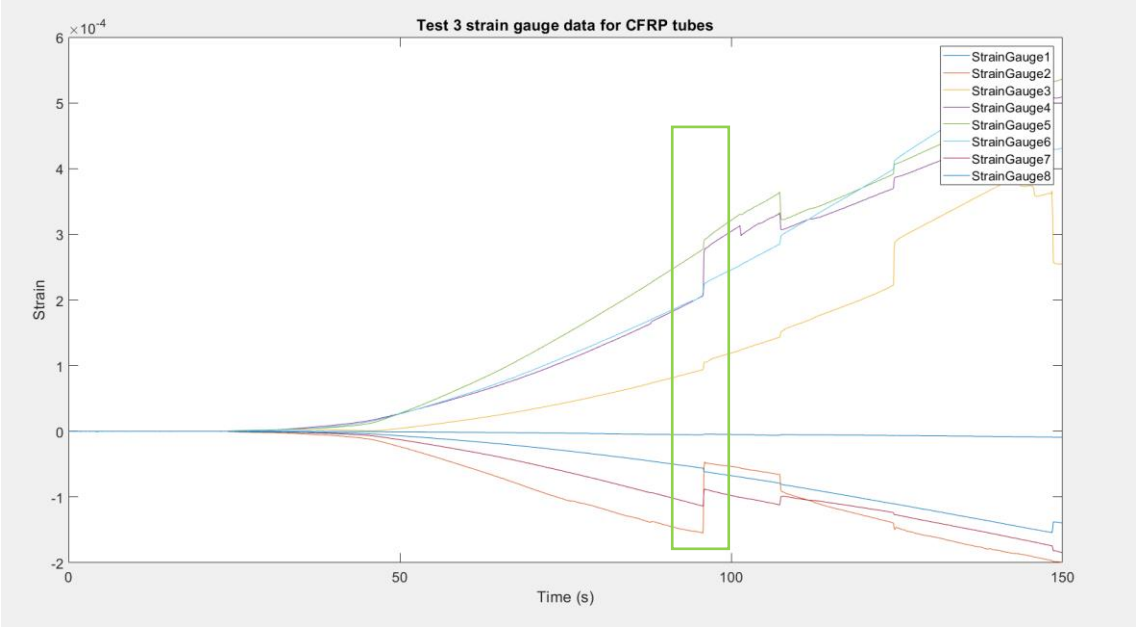

Figure 129 shows the third test's strain gauge data of the aluminium joints. Strain gauges 12 and 14 had the largest strain change.

Figure 129

Test 3 strain gauge data of strain gauges 9 to 14 (aluminium joints)

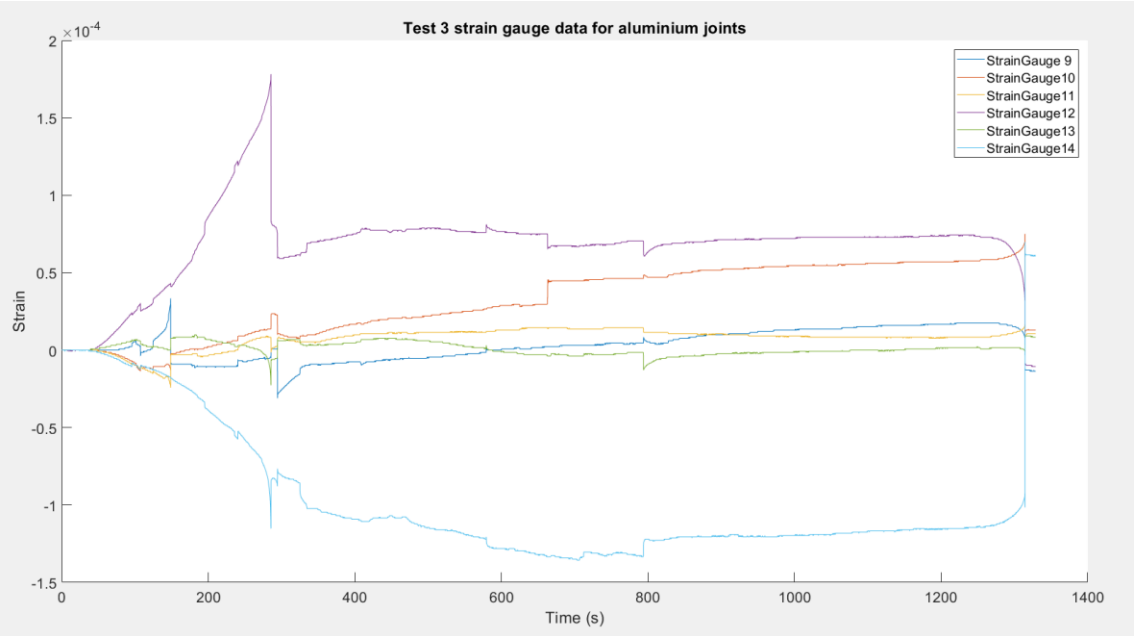

The strain gauge data indicates the adhesive joints' first major joint crack always happens at strain gauge two's position, and all three tests show the same results. The second large strain during the first crack usually happed at strain gauge 4. In the first test, strain gauge five also shows a large strain. All these three strain gauges are located at the short green axis, as shown in figure 130. The green axis is shorter than the orange axis. Therefore, the short the structure, the lower the joints' stability. The longer CFRP tubes allow more structure deformation before the adhesive layer starts to crack.

Figure 130

Axis indication of the structure

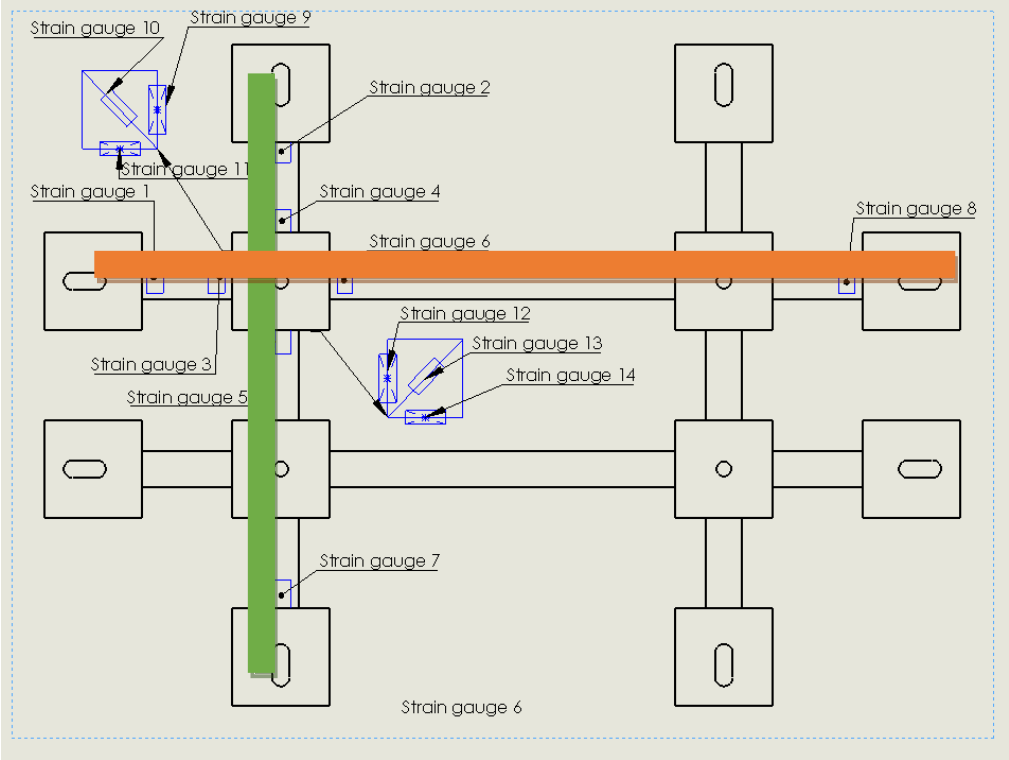

Figure 131 shows the status of three test demonstrators after finishing the tensile test. The first and the third test demonstrators were under 30.8 kN and 40 kN load. Figure 132 shows the CFRP tubes were under bending and had a large deformation. But none of the tubes was loosened from the joints after the experiments, and the test demonstrators did not show any significant deformation. From the strain gauge data, all three test demonstrators' first joint cracks happened before the minimum test load, but the structures were still bonded.

Figure 131

Three test demonstrator's status after the experiments

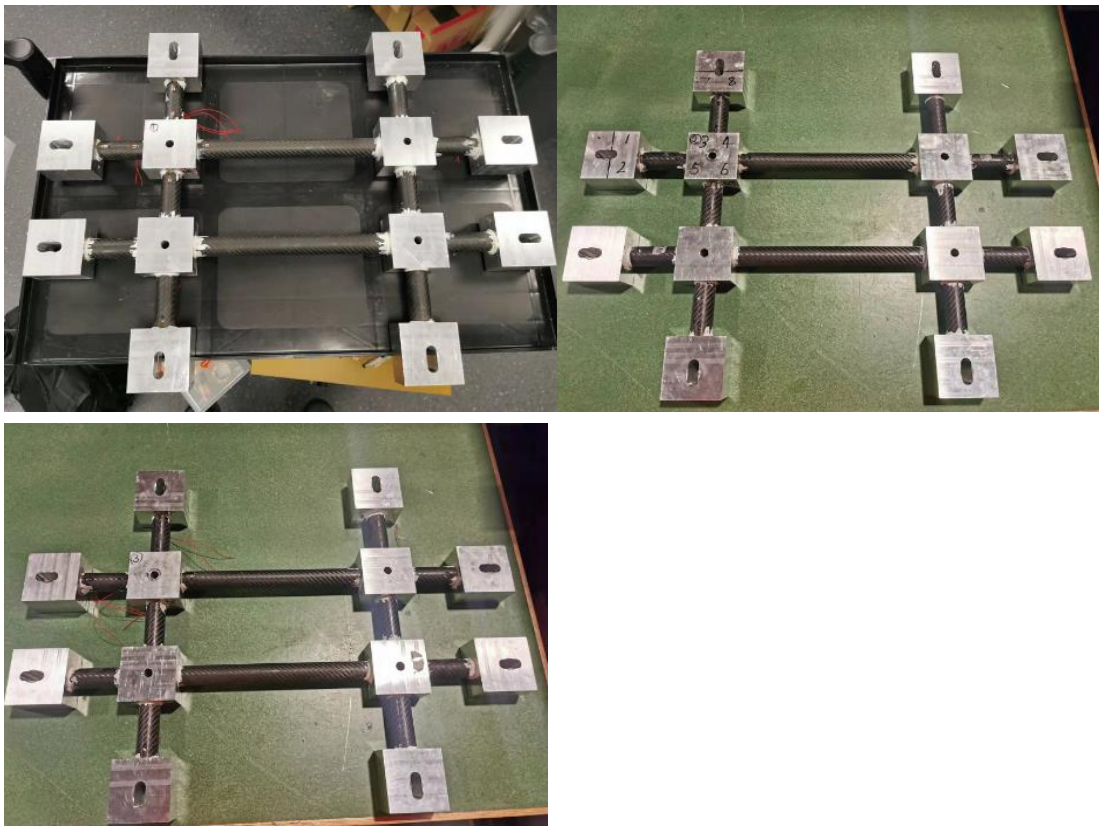

Figure 132

The CFRP tubes were under large bending force

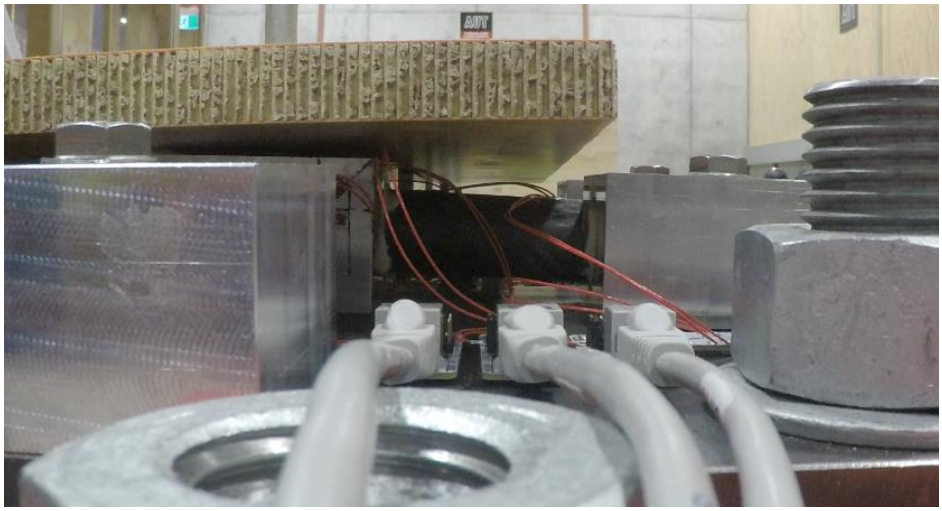

4.2 Failure mode analysis

Figure 133 describes an overview of the overall sample's cutting surfaces to determine the structure's failure modes.

Figure 133

The cut surfaces of the sample for failure mode determination

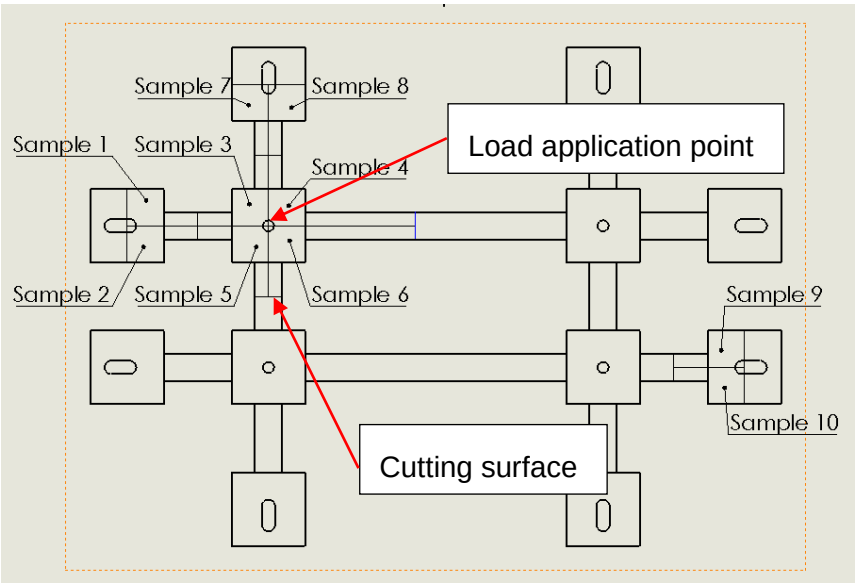

Samples 1 to 8 are the sections that surround the force application point. The samples' cross-sectional views are used to determine the failure mode. Sample 9 and Sample 10 were away from the load application point. Examining Samples 9 and 10 was to compare joints with lower load.

Figure 134 shows the technical demonstrator after the load test. The structure was exposed to a load well above the maximum target load. There was visible delamination of the adhesive from the aluminium joints at the interface.

Figure 134

The first test frame after finishing the first experiment

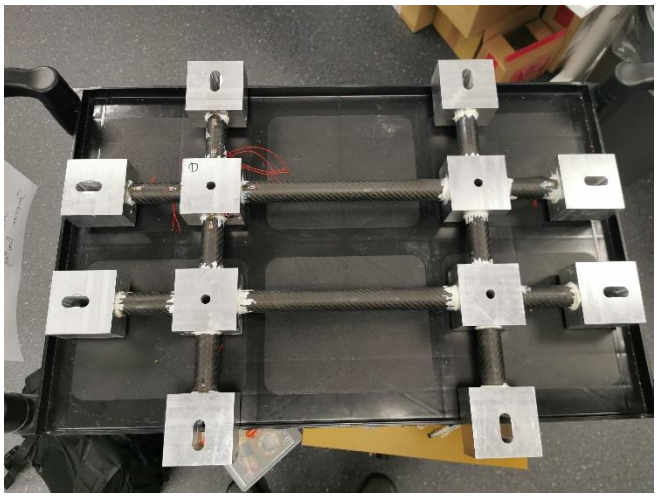

Figure 135 illustrates the delaminated adhesive from the aluminium joint surface. The tube bending caused a shearing force between the aluminium joint and the CFRP tubes.

Figure 135

Adhesive delamination from the aluminium joint surface

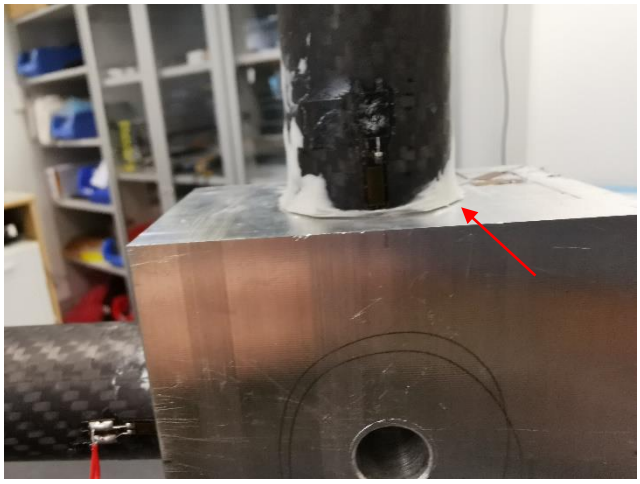

Figure 136 illustrates Samples 9 and 10 in cross-sections as a reference. There was no visible damage to the adhesive layer for these samples, and the CFRP tubes were still bonded with the aluminium joints.

Figure 136

Cross-section of Sample 9 and Sample 10

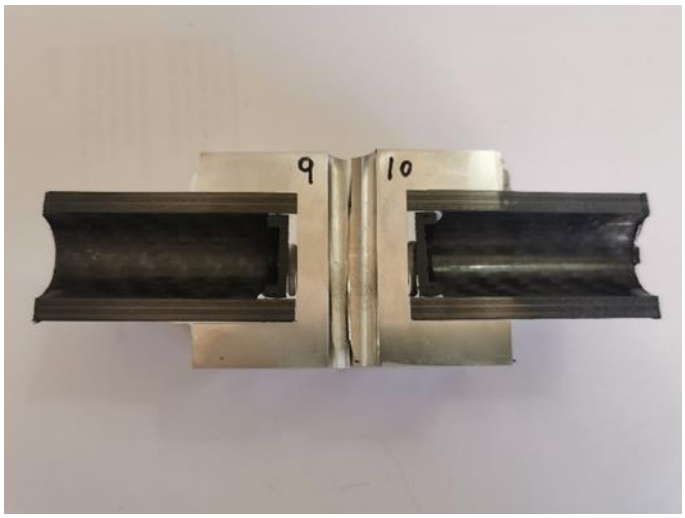

Figure 137 shows a fracture that appeared at the lower side of the joint from Samples 1 and 2 (see red arrows). The CFRP tubes were still bonded on the opposite side. The bottom part was loaded in tension, and the upper part was in compression.

Figure 137

Cross-section of Sample 1 and Sample 2

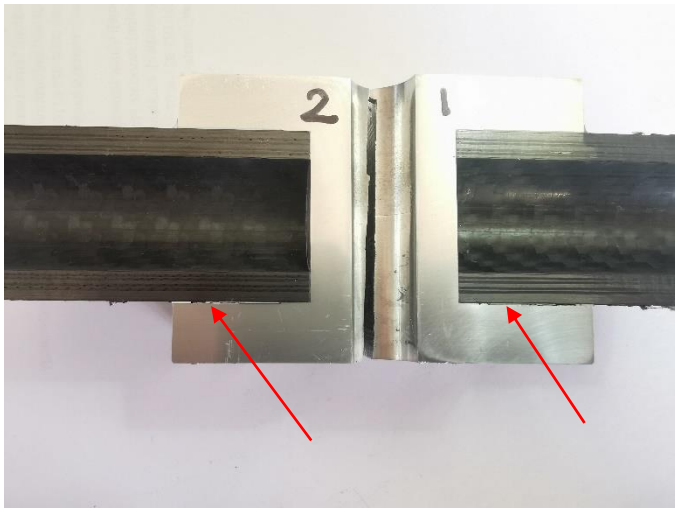

Figure 138 shows the sectioned aluminium joint where the load was applied. After sectioning the aluminium joint, the CFRP tubes did not adhere to the aluminium part

(Sample 3, Sample 4, and Sample 6). Therefore, the adhesive failed during the structural test for these bonds.

Figure 138

Samples 3, 4, 5, and 6

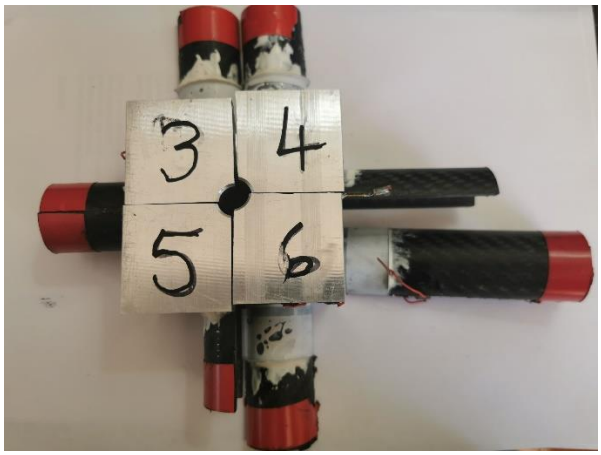

Figure 139 (a) shows tube one on Sample 3 failed to bond with the aluminium joint after sectioning. An estimated 3% of the adhesive remained on the aluminium joint (some small bubble-shaped adhesive). 97% of the adhesive remained on the CFRP tube. Therefore, the failure mode of Sample 3 was an adhesive failure, as described above in Figure 24 (a). The failure mainly occurred at the aluminium surface. Figure 139 (b) shows minor fractures that occurred at the adhesive layer of Tube two, but the CFRP tube was not debonded from the aluminium joints. Therefore, the adhesive did not fail.

Figure 139

Cross-section of sample 3

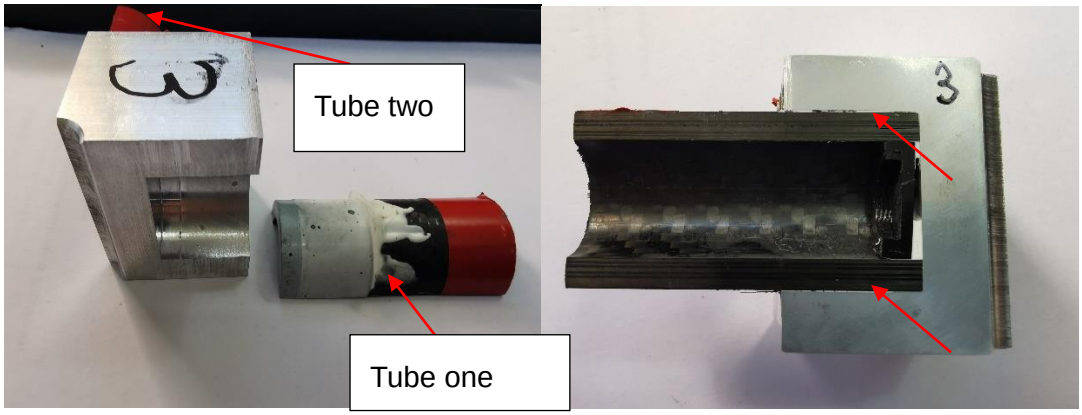

(a). (b).

Note. (a) Sample 3 with Tubes one and two. (b) Sample 3 with Tube two section.

Figure 140 (a) shows Sample 4's Tube one debonded from the joints. The failure mode was an adhesive failure, as described in figure 24 (a). The adhesive failed on the aluminium and the CFRP tube, similar to Sample 3. An estimated 20% of adhesive failure happened at the CFRP tube side, and 80% of adhesive failure occurred on the aluminium side. Figure 140 (b) illustrates that the sample appeared not to have any fractures, and the CFRP tube was still bonded with the aluminium joint.

Figure 140

The sample 4

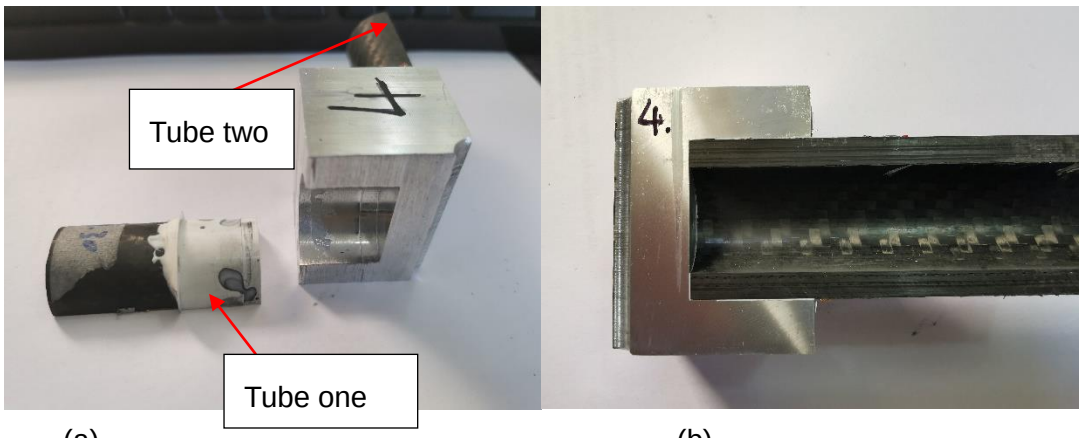

(a) (b)

Note. (a) Sample 4's Tube one and Tube two. (b) Sample 4's Tube two section.

Figure 141 (a) illustrates a fracture observed in the bottom adhesive layer of Sample 5's section one. Figure 141 (b) shows a fracture in the top adhesive layer. None of the joints failed in Sample 5.

Figure 141

The sample 5

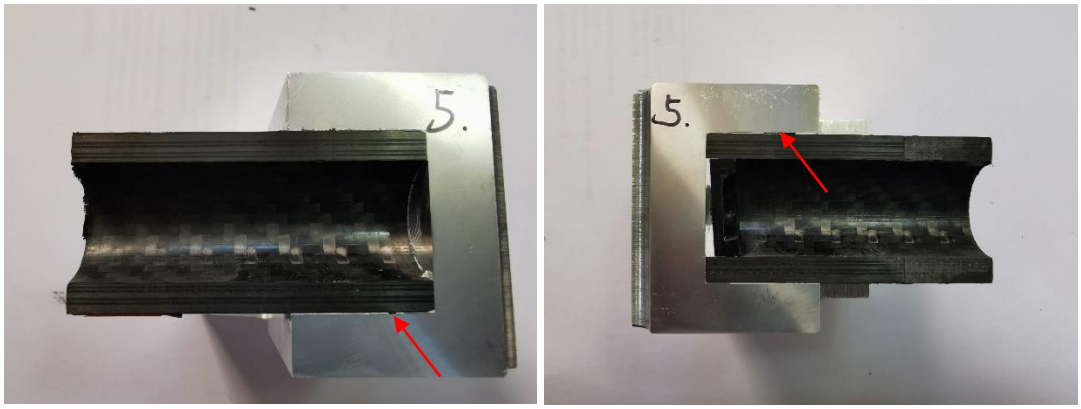

(a) (b)

Note. (a) Sample 5, section one. (b) Sample 5, section two.

Figure 142 (a) illustrates the CFRP tubes of Sample 6, both debonded from the joints. Figure 142 (b) illustrates that tube one's failure mode was an adhesive failure that mainly occurred on the aluminium side. An estimated 2% of the fracture surface appeared at the CFRP tube side of the bond. Figure 142 (c) shows that the failure mode of tube two is a mixed mode. The primary failure mode was an adhesive failure and occurred at the aluminium surface. An estimated 12% of failure was an adhesive failure at the CFRP tube surface. However, an estimate of 10% cohesive failure was found on tube two, as described in Figure 24 (b). Therefore, tube two showed a mixed failure mode of mixed adhesive failure and cohesive failure.

Figure 142

The sample 6

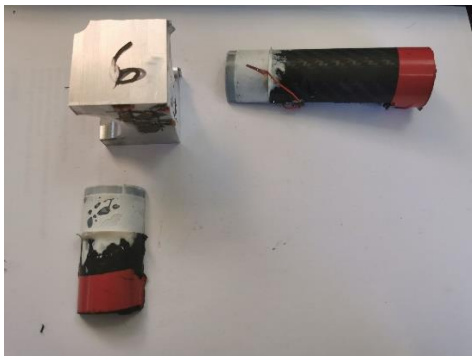

(a)

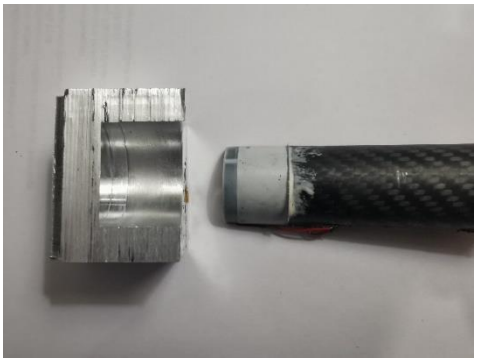

(b)

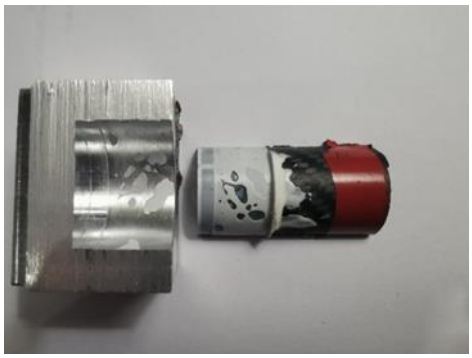

(c)

Note. (a) Sample 6. (b) Sample 6's tube one. (c) Sample 6's tube two.

Figure 143 illustrates Sample 7's CFRP tube debonded from the joint. The failure mode in this sample was a mixed adhesive failure similar to Sample 6's tube two. The adhesive failure on the aluminium side was estimated at 70%, and the adhesive failure on the CFRP tube side had an estimate of 28%. Only 2% of failure was cohesive failures in Sample 7. Sample 8 has no significant fracture, and the adhesive had not filled the gap during the assembly process, as shown by the red arrow, but the tube was still bonded with the aluminium joint.

Figure 143

Sample 7 and Sample 8 cross-sections

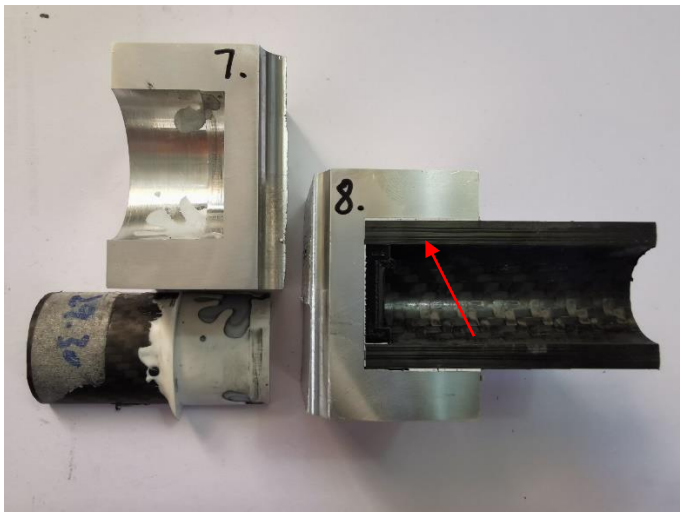

During this test, samples 3, 4, 6, and 7 had debonded CFRP tube parts. After the sectioning process, samples 3, 4, and 6's CFRP tube parts were debonded from the joints. Sample 7's CFRP tube was still bonded with the aluminium joint after the initial sectioning.

The CFRP tubes of Samples 3, 4, and 7 were expected to debond from the joints. However, the CFRP tube on Sample 6 was also debonded. This result went beyond the original hypothesis. The experiment applied 30 kN force to the demonstrator, twice the design load.

The failure modes of the debonded tubes were mainly adhesive failures on the aluminium surface; only a small fraction of the failure occurred in the CFRP tubes. The failure mode was mixed for two samples, combining a small percentage of cohesive failure and adhesive failure (10% on Sample 6's tube two and 2% on Sample 7). The failure mode of the test demonstrator joints is close to the description in the HPR 25 epoxy adhesive's property data, which is 80% of adhesive failure and 20% of cohesive failure (see table 7). The current failure mode pattern indicated that the adhesive did not bond with the aluminium surface well. For comparison, the surface treatments were the same as the CFRP tubes. Both surfaces had been cleaned with ethanol and

sanded with 240-grit sandpaper. The original hypothesis was that the failure mode would be mainly cohesive failures, which failed at the adhesive layer since the adhesive had a lower mechanical strength than aluminium alloy and CFRP tubes.

Two main reasons may cause the current adhesive failure mode (mainly adhesive failure occurred on the aluminium surface). The first reason was that the surface treatment process on the aluminium surface using grit 240 sandpaper was too fine for the aluminium surface. Moreover, the contact area was the 30 mm hole's inner surface of the aluminium joint, which is hard to conduct an evenly sanded surface by hand. The second reason is the aluminium oxidate very fast; the oxidation layer was formed before the adhesive was applied to the aluminium surface. The oxidation layer weakens the bonding with the aluminium surface. Therefore, a better surface treatment method was needed. The sample analysis identified a proper surface treatment method for aluminium was critical to this adhesively bonded hybrid structure. The sectioned samples illustrated the failure mode of the demonstrator was mainly an adhesive failure that occurred on the aluminium surface, as shown in figure 24 (a), which indicated bonding with the aluminium was harder than bonding with the CFRP tubes. Therefore, a better bonding method such as an improved surface treatment process and a better adhesive was critical for future adhesively bonded aluminium-CFRP hybrid structure applications.

Twice of the design load was applied, and the first test demonstrator was not destroyed, But the first adhesive joint failure that occurred during the load was 9 kN (design load was 14.33 kN, and the total load applied to the demonstrator was 30 kN). And the load applied to the third test demonstrator was around 40 kN, and the structure remained bonded. The sectioned samples showed the adhesive layer was damaged. The adhesive thickness was 0.2 mm. The literature study shows that is the optimal thickness for adhesive performance. But it is still weaker than the aluminium alloy and the CFRP. The adhesive is used to join the aluminium and the CFRP together but not to withstand high loads. Based on this experiment, the CFRP tubes and the aluminium

didn’t significantly damage after withstanding 40 kN loads. The structure performance can completely rely on the CFRP and the aluminium alloy’s strength.

The thickness of the adhesive layer can be reduced to as thin as possible as long as the two materials can be bonded together. And it also identified one major disadvantage of the structure, and the damaged adhesive layer is hard to be identified. The CFRP tubes remained bonded after the experiments and showed no significant damage from their appearance. A suitable non-destruction test method should be investigated for examination. The adhesive bonded method is a permanent joint method. It is hard for the damaged parts to be replaced and repaired. An adhesive that could be easily replaced should be considered. Such as the adhesive that could be easily dissolved by other chemicals or methods to allow the structure to replace parts or re-apply adhesive easily (such as hot-melt adhesive).

This experiment proved the reliable mechanical performance of the CFRP tubes and the aluminium joints. The parts size could be further reduced in the future application to save weight and cost.

4.3 FEA analysis

This section discovered the strain relationship between the SolidWorks FEA simulation and all three physical test results. This process investigates the behaviour difference between the actual demonstrators and the SolidWorks models. The analysis results can be used as a reference for future development. Strain gauges 1 to strain gauge eight were placed on the CFRP tubes, and strain gauges 9 to 14 were placed on the aluminium joints, as shown in figure 144. The strain gauges 1, 3, 6, 8, and 14 were on the X-axis in the SolidWorks model. And the strain gauges 2, 4, 6, 7 and 11 were on the Z-axis. The strain gauges 9 and 12 were on the Y-axis. Since SolidWorks simulation cannot simulate the strain on the 45-degree axis, strain gauges 10 and 13 are ignored for this comparison process.

Figure 144

Strain gauge layout of the structure

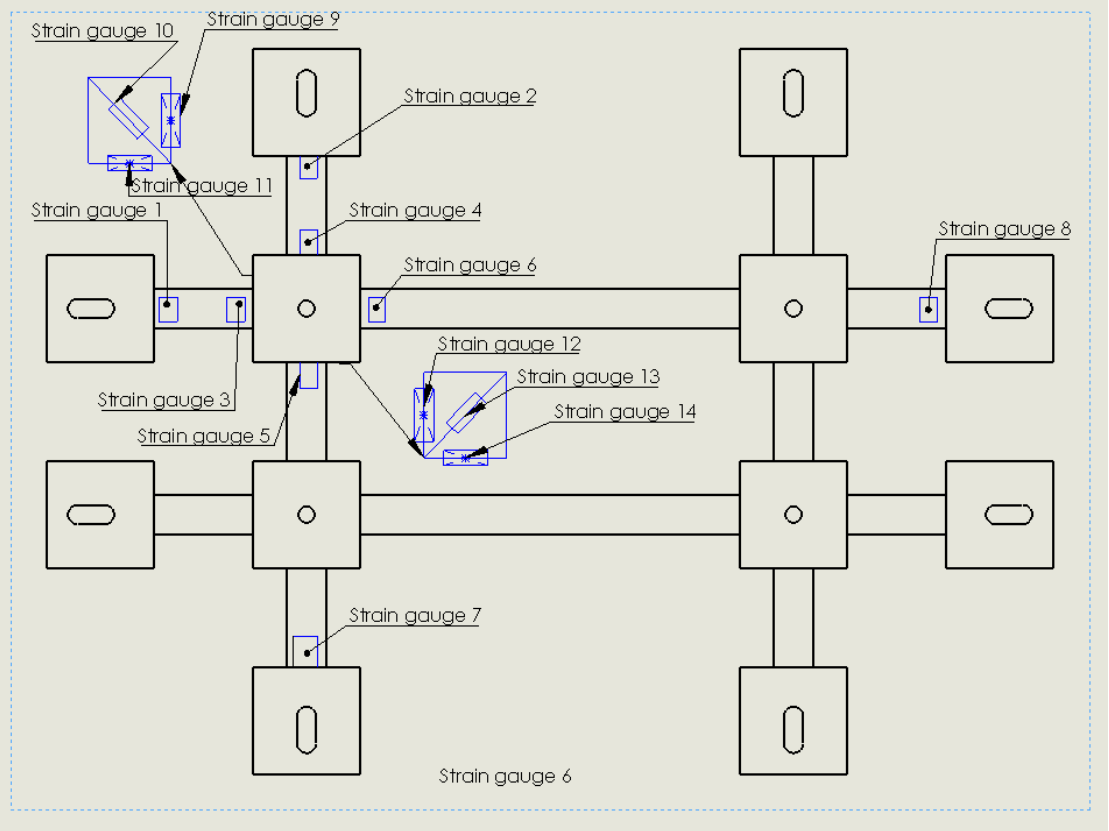

Figure 145 displays the SolidWorks FEA strain results and the strain gauge data retrieved from strain gauge 1. The strain data are all in a decreasing trend. Test two has a closer trend when compared to the FEA simulation result. Test 3 has a strange trend; its strain changes were smaller than the other three data sets.

Figure 145

Strain gauge 1 data and the FEA result

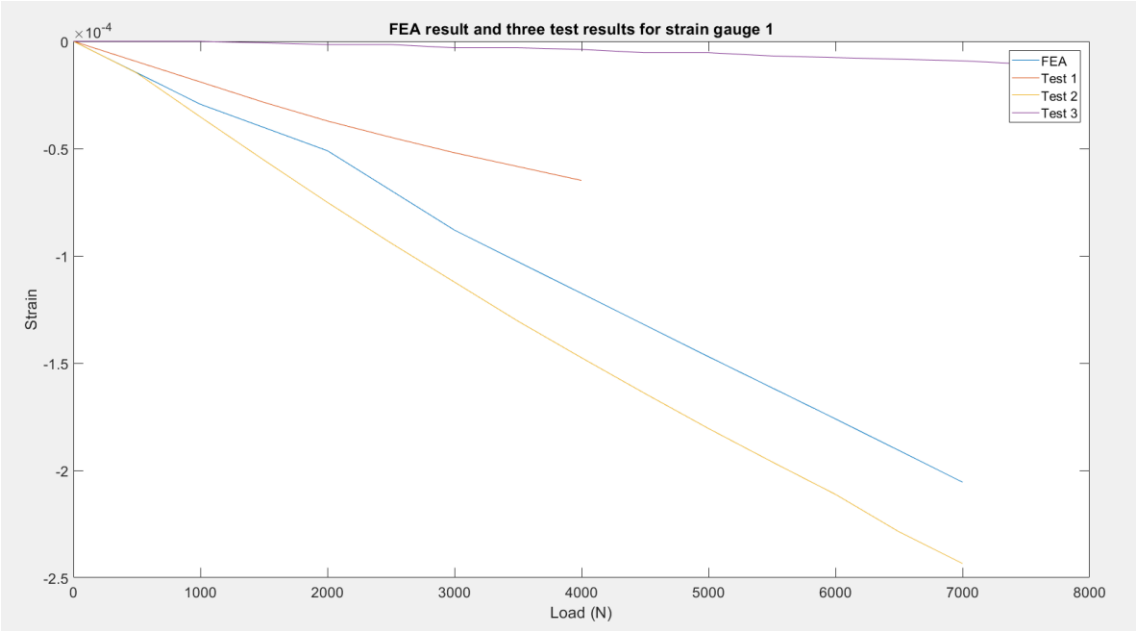

Figure 146 displays the SolidWorks FEA strain results and the strain gauge data retrieved from strain gauge 2. The strain data are all in a decreasing trend. Test two has the closest trend when compared to the FEA simulation result. Test 3 has the largest difference compared to the other three data sets.

Figure 146

Strain gauge 2 data and the FEA result

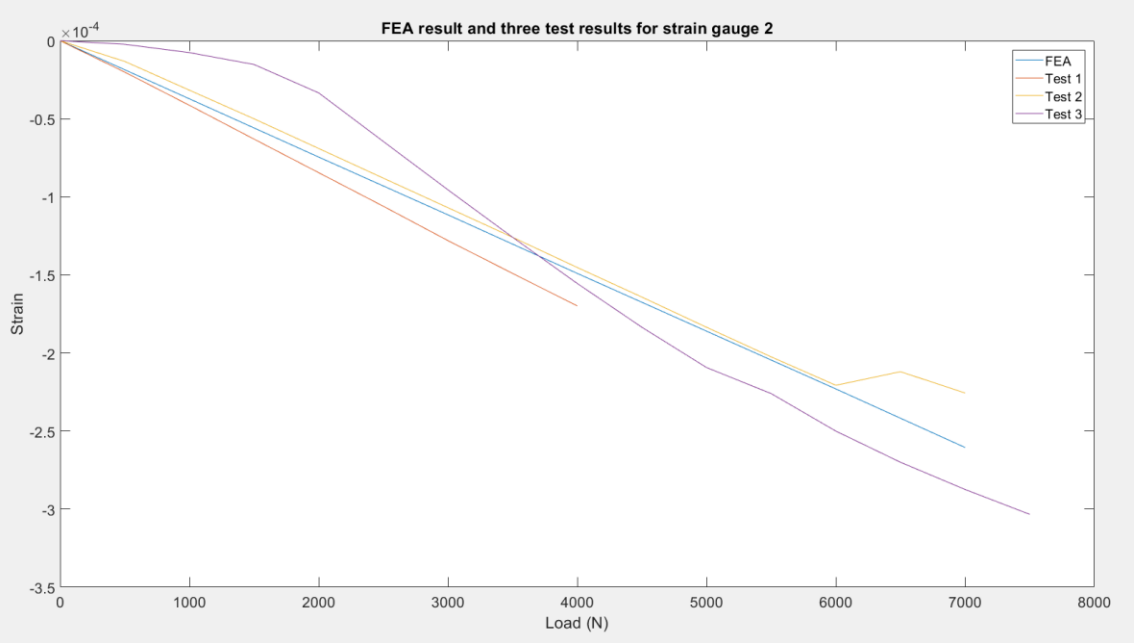

Figure 147 displays the SolidWorks FEA strain results and the strain gauge data retrieved from strain gauge 3. The strain data are all in an increasing trend. Test one has the closest trend when compared to the FEA simulation result. Test one and test three's trends are closer.

Figure 147

Strain gauge 3 data and the FEA result

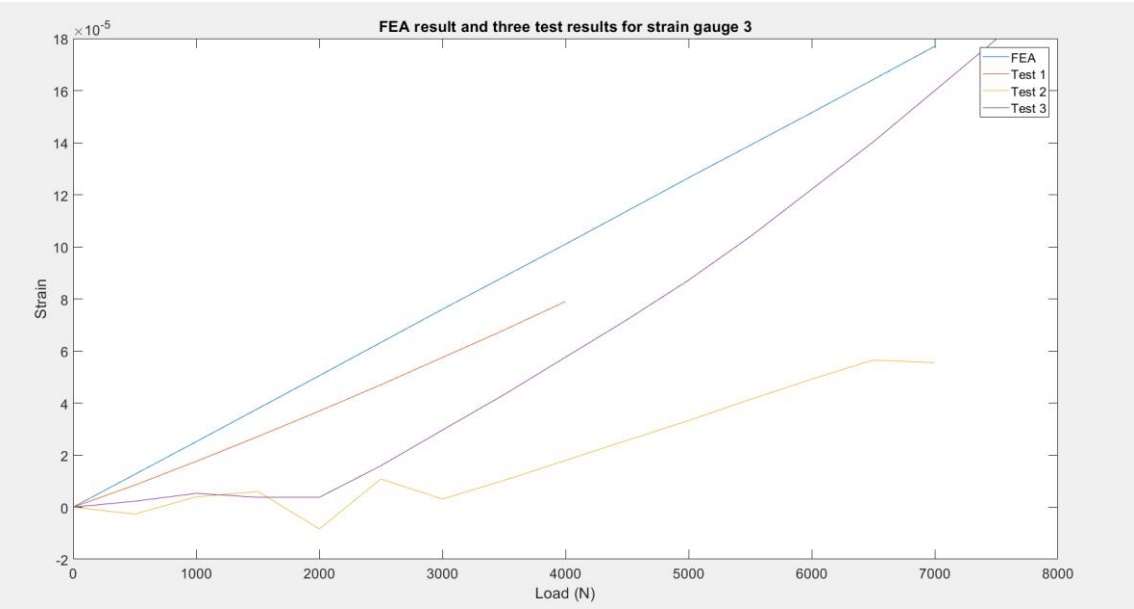

Figure 148 displays the SolidWorks FEA strain results and the strain gauge data retrieved from strain gauge 4. The strain data are all in an increasing trend. Test one has the closest trend to the FEA simulation result.

Figure 148

Strain gauge 4 data and the FEA result

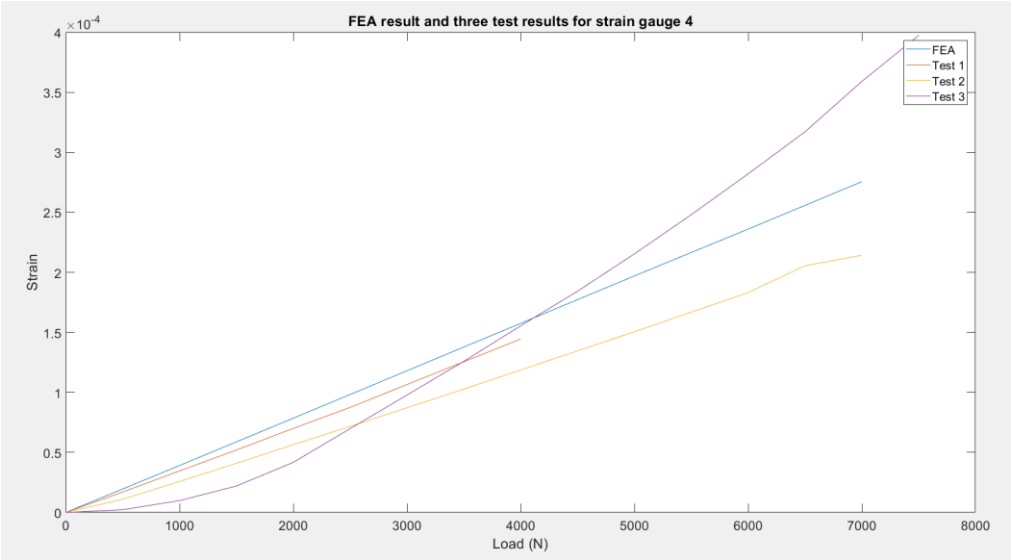

Figure 149 displays the SolidWorks FEA strain results and the strain gauge data retrieved from strain gauge five. The strain data are all in an increasing trend.

Figure 149

Strain gauge 5 data and the FEA result

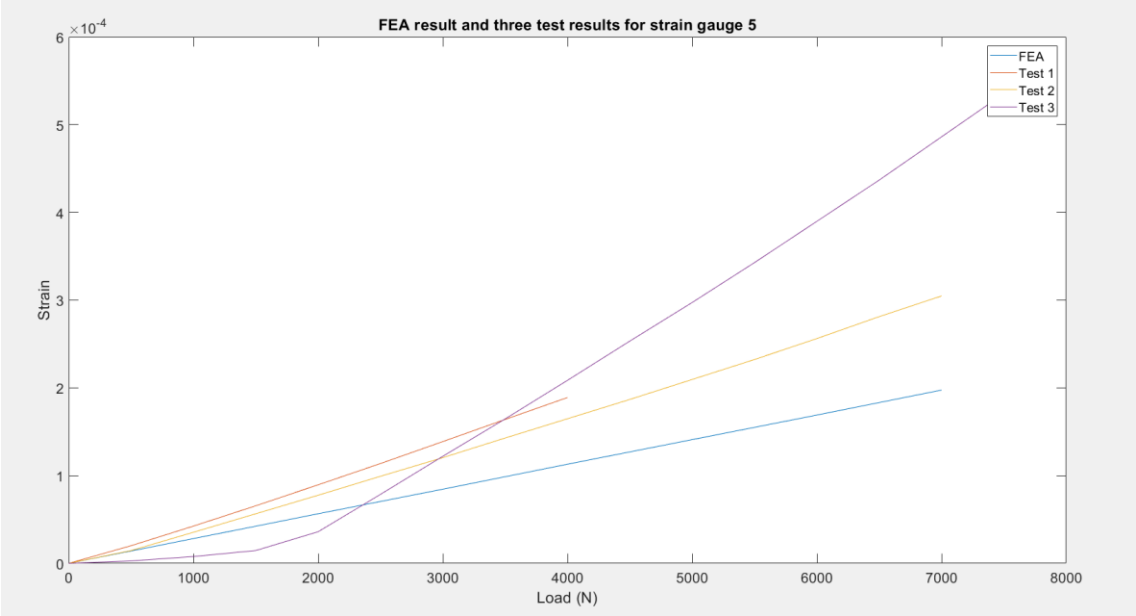

Figure 150 displays the SolidWorks FEA strain results and the strain gauge data retrieved from strain gauge 6. The strain data are all in an increasing trend.

Figure 150

Strain gauge 6 data and the FEA result

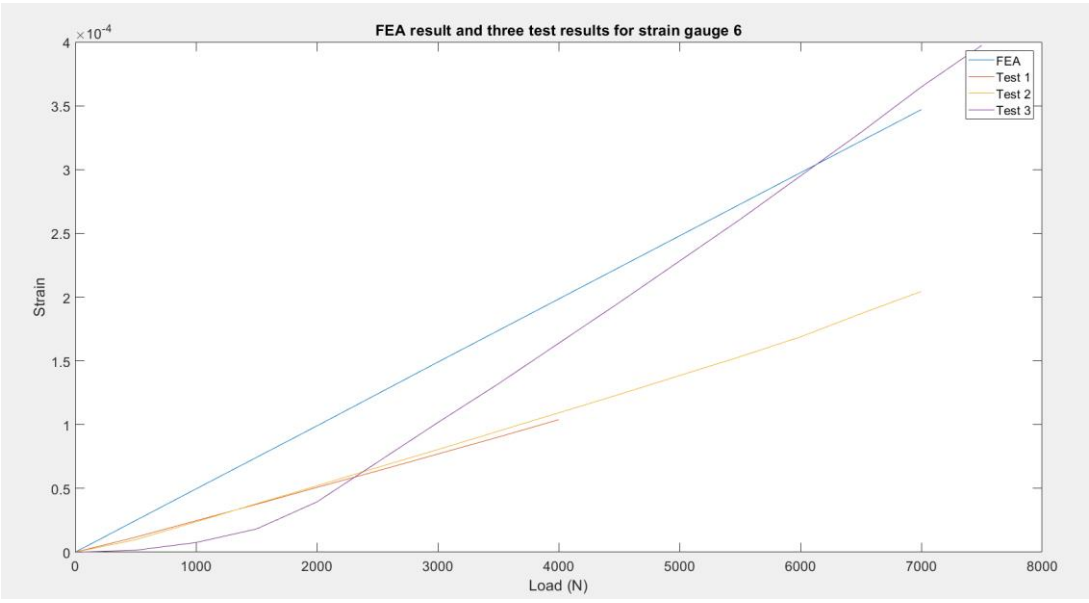

Figure 151 displays the SolidWorks FEA strain results and the strain gauge data retrieved from the strain gauge 7. The strain data are all in a decreasing trend.

Figure 151

Strain gauge 7 data and the FEA result

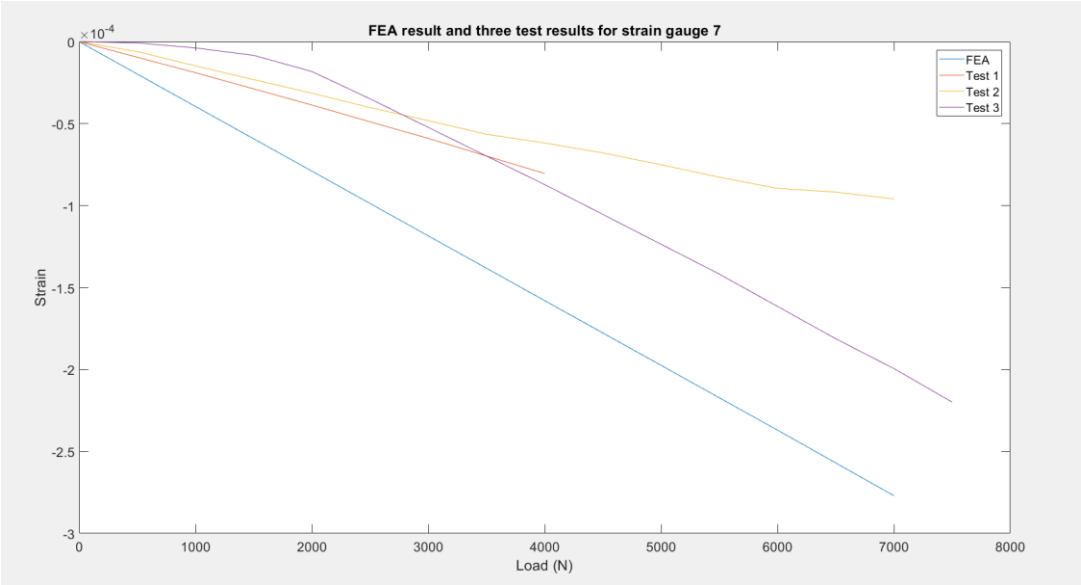

Figure 152 displays the SolidWorks FEA strain results and the strain gauge data retrieved from strain gauge 8. The strain data are all in an increasing trend.

Figure 152

Strain gauge 8 data and the FEA result

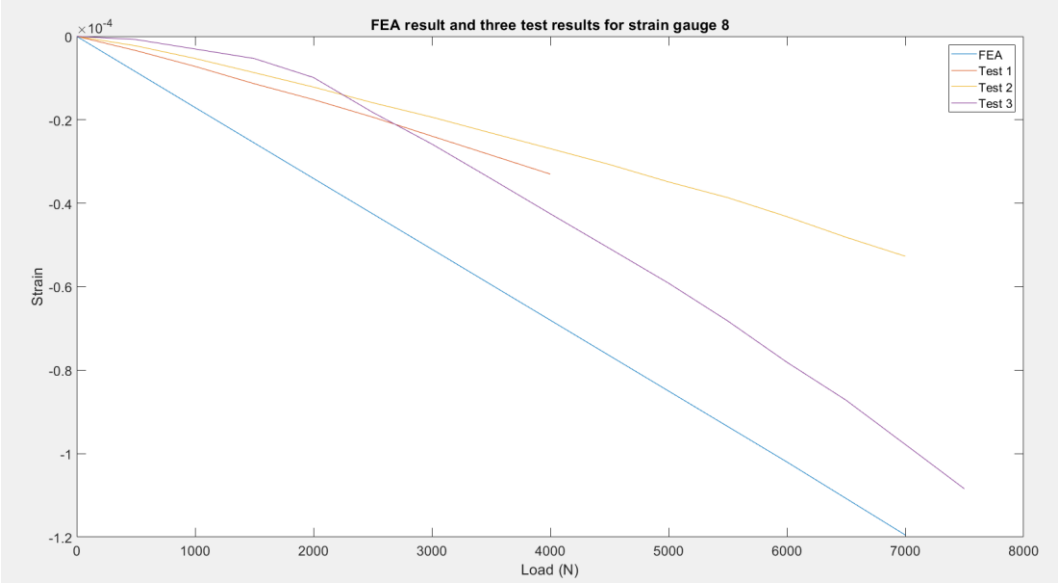

All the FEA results on the CFRP tubes illustrated a consistent changing behaviour in the three experimental results. The strain gauges 3, 4, 5 and 4 were attached around the pulling point, and the measurement gauge was under the tensile influence. Therefore, the recorded data shows an increasing trend since the tubes close to the measuring points had been pulling downwards. And the SolidWorks FEA simulation had the same behaviour. The strain gauges 1, 2, 7 and 8 were attached to positions close to the holding blocks and under compression force. So, the recorded data shows a decreasing trend since the CFRP tubes close to the measuring points had been pulling upward. The SolidWorks FEA simulation had the same behaviour. The comparison results show that the SolidWorks simulation has a more consistent behaviour than the physical tests on the CFRP tube parts.

But the SolidWorks simulation shows an inconsistent behaviour compared to the aluminium results. Figure 153 displays strain gauge 9's FEA simulation, which indicates an increasing trend. The three tests show an increasing trend, but the gradient is smaller than the FEA results.

Figure 153

Strain gauge 9 data and the FEA result

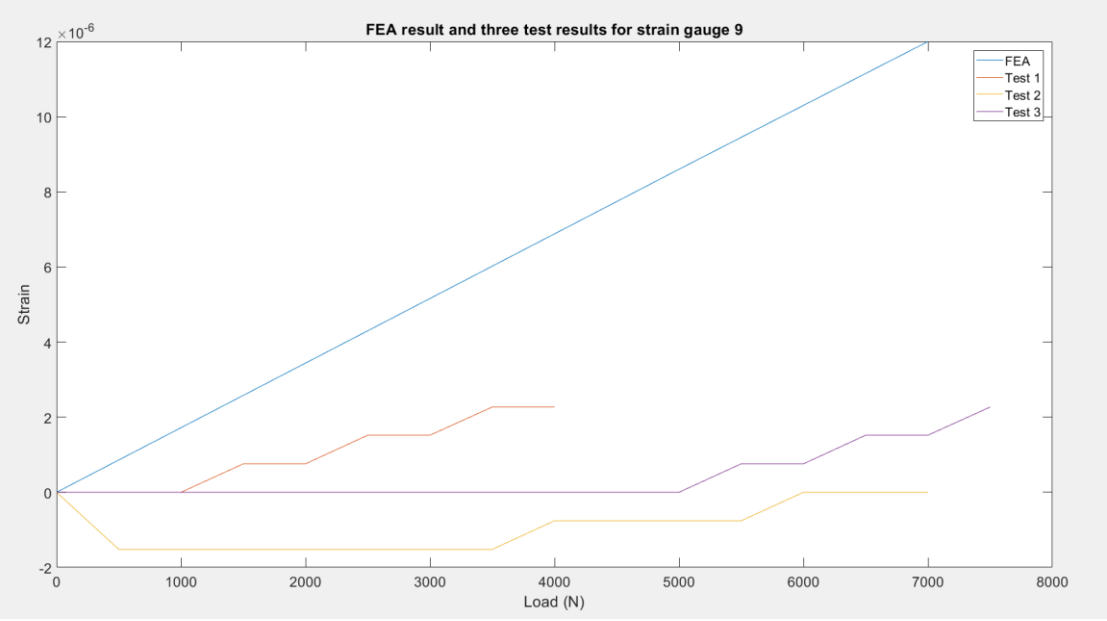

Figure 154 illustrates a completely different trend between the FER simulation and the physical tests for strain gauge 11. The FEA simulation indicated an increasing strain, but all the physical tests suggested a decreasing strain behaviour.

Figure 154

Strain gauge 11 data and the FEA result

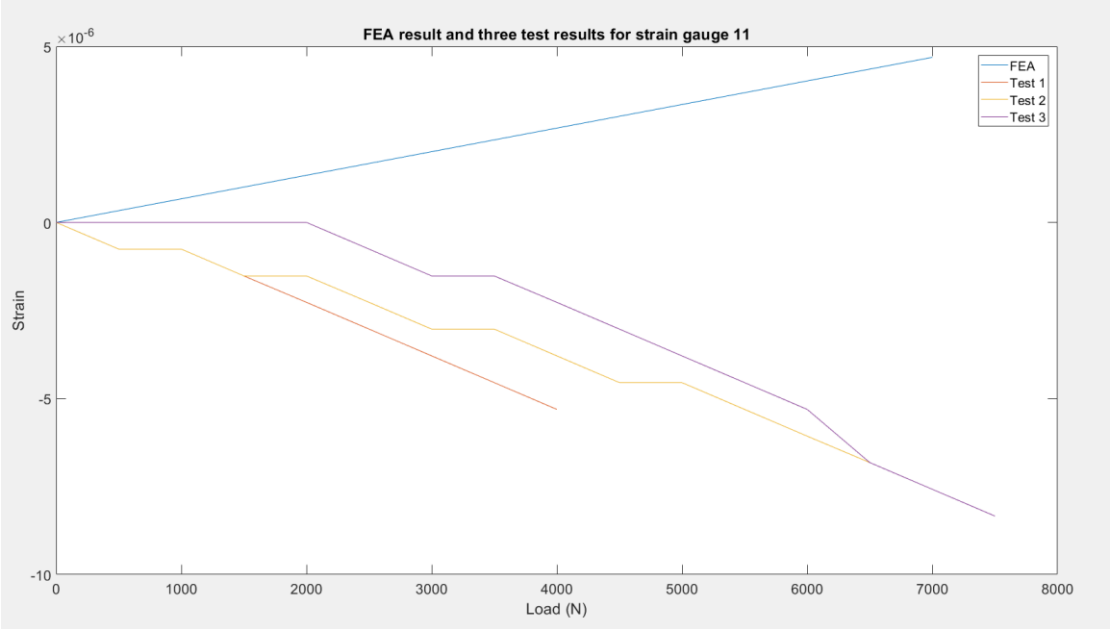

Figure 155 shows the Strain gauge 12 data and the FEA result. Only test 1 resulted in the opposite behaviour compared to the FEA simulation results. Test 2 and test 3 all show an increasing trend.

Figure 155

Strain gauge 12 data and the FEA result

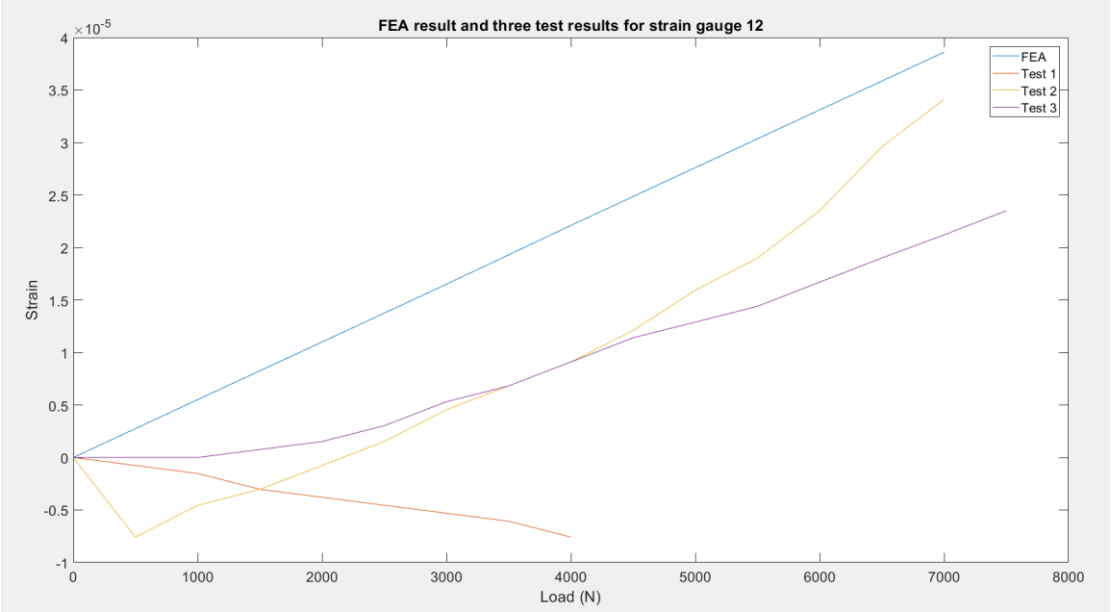

Figure 156 shows test 2 has the opposite behaviour compared to the FEA simulation. Test 1 and test 3 are all decreasing but with a smaller gradient.

Figure 156.

Strain gauge 14 data and the FEA result

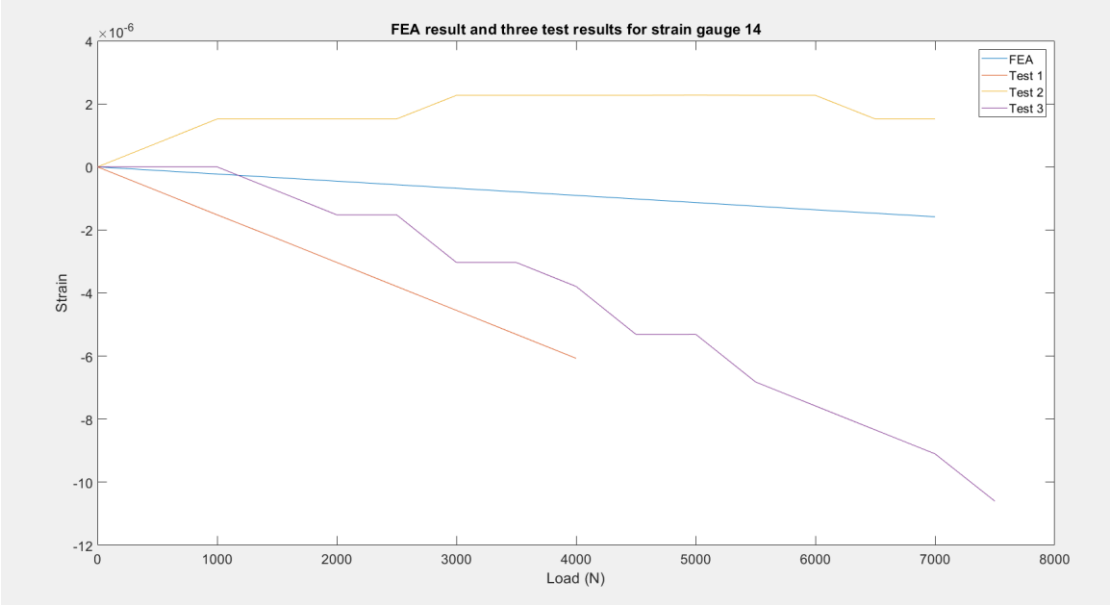

Figures 153 to figure 156 illustrated an inconsistent strain pattern. The simulation on the aluminium joints was unsuccessful. Several possible reasons can cause this unsuccessful simulation.

1. The aluminium joints were made by a thick aluminium bar, and it is quite hard for the strain gauge to detect some very small changes.
2. The simulation results differed from the physical tests, and the physical tests also behaved differently. The un-standard surface treatment process and the strain gauge installation may also negatively influence the experimental results.
3. The FEA simulation did not simulate the complete test layout. One main difference between the CAD models and the real test configuration. As shown in figure 157, a nut is placed on the top of the aluminium joints to secure the eyebolt. The nuts in the experiment set-up provide an additional compression force to the aluminium joints. The tightening force was not measured, so it cannot be added to the simulation. Therefore, this could be the main reason that caused a successful simulation of the aluminium joints. The nut secured on the top can be removed if there are more similar experiments. The nut on the top will not make too much difference to the test. When the eyebolt is under a lot of loading, its body will stretch, and the nut will move away from the joints, as shown in figure 158. It can only increase the difficulty level of the FEA simulation. The nut secured on the top can be removed if there are more similar experiments.

Figure 157

A nut was secured on the aluminium joints

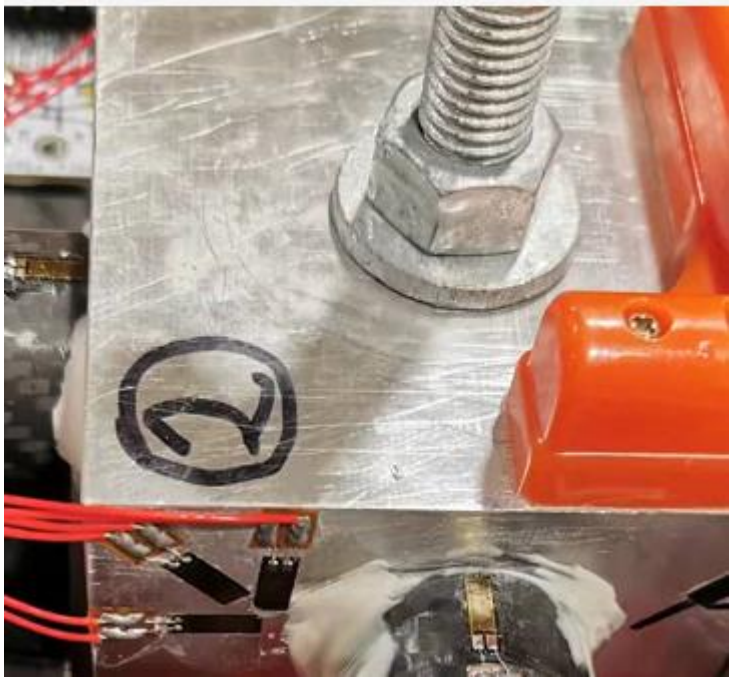

Figure 158

The eyebolt was being stretched

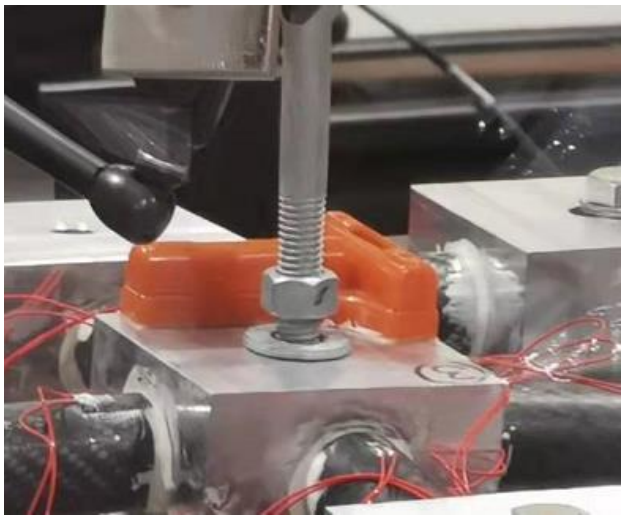

Figure 159 demonstrates the largest deformation location in the FEA analysis. Sample 6's position had been lifted higher than other parts (see figure 133 for sample 6's position). Figure 160 shows the actual position change during the experiments. The position change was monitored by the level and recorded by the camera. The video shows the actual position change is the same as the FEA analysis. But unfortunately, the deformation recorded by the actuator cannot be used since the eye bolt, chain, and shackles were also deformed during the tests. Therefore, the recorded deformation is the sum of the structure deformation and the connection parts' deformation. But the deformation pattern is the same as the FEA analysis.

Figure 159

The largest deformation area in the FEA analysis

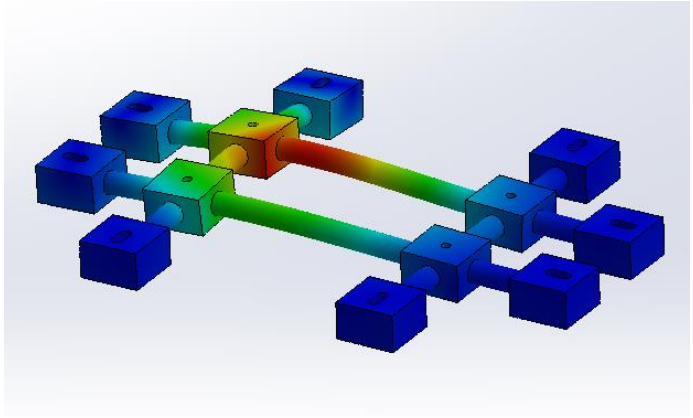

Figure 160

The level installed on the demonstrators shows the structure deformation behaviour is the same as the FEA result

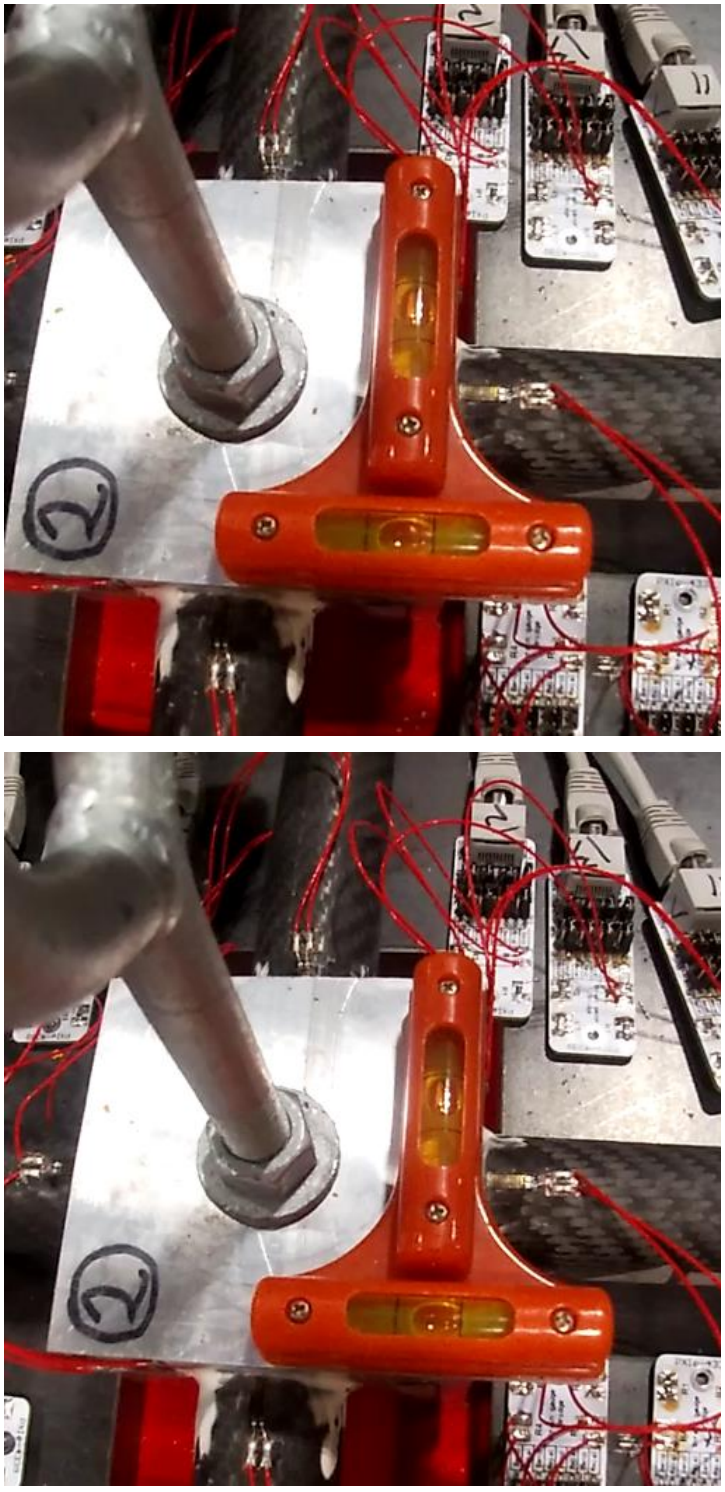

Chapter 5 Conclusion and future development

The experiments were successful. The load withstood by the test demonstrators was 40 kN loads, and the structure remains bonded without significant large deformation. The hybrid structure shows its superior performance, and it exceeds the requirements of the minimum test loads. The structure was designed to withstand large shearing force, but the shearing force was not the main issue since the load was mainly applied to the aluminium joints. Therefore, the size of the parts can be further reduced to save cost and weight in a future application. The experiment results prove the concept of using adhesive hybrid joints' performance is reliable and outperforms the original structure.

The adhesive layer cracks before reaching the minimum design loads, but the whole structure can continue to undertake loads almost three times larger than the original design load. The experiment result indicates the structure mainly relies on the CFRP tubes and the aluminium joints' strength rather than the adhesive layer. The 0.2 mm epoxy optimal layer thickness is unnecessary to the structure since the adhesive strength will always be lower than the CFRP and the aluminium alloy. Therefore, the adhesive thickness can be reduced to as thin as possible as long as the CFRP tubes and aluminium joints maintain a stable connection. The major cracks always occur at the short CFRP tube axis. The longer CFRP tubes can reduce the stress on the adhesive layer. Therefore, short CFRP tubes can increase their length to gain better performance. Further research on the optimal tube length ratio can be conducted.

The sectioned samples identified the test demonstrator's most common failure mode, the adhesive failure at the aluminium surface. The failure mode indicates bonding with aluminium alloy is harder than bonding with CFRP material. The surface treatment process applied to the aluminium alloy and the CFRP material is the same. Therefore, a proper surface treatment method is critical for the aluminium surface. A new surface treatment method is the key to the reliability of the adhesive joints.

The SolidWorks FEA study proves the strain analysis pattern for the CFRP tubes, and the overall structure deformation can be used as a reference. The aluminium strain analysis failed since the simplified structure cannot simulate the actual situation since all the bolts and nuts (on the top of the aluminium joints) provided additional effects to the aluminium joints.

Therefore, this experiment proves that the adhesive-bonded metal-composite hybrid structure concept is worth further research and development.

In the future study, the following aspects can be further researched:

1. Research the suitable surface treatment process for the aluminium surface. The failure mode analysis shows the surface treatment procedure for aluminium parts is critical to the adhesive joint strength.
2. Reduce the adhesive layer thickness. The experiment's result indicates the thick adhesive layer is not necessary for the joints. Only a thin layer to bond the structure is enough.
3. Conduct research to test the suitable joint depth for CFRP tubes. The joint depth for the CFRP connection is mainly the best to use the space in the design of the original part. Further study of the joint’s depth effect can enhance the structural performance or reduce the parts' size.
4. Find a suitable NDT exam method to examine the adhesive joints. The adhesive layer cracks, and the CFRP tubes’ damage cannot be spotted. Therefore, a suitable NDT exam method is important for the structure check.

5. Develop suitable parts replacement and maintenance methods. Adhesive bonding is a permanent joint method. Parts replacement and repair process is important to the actual maintenance application.

Appendix

Appendix A Calculation Summary

Appendix A1 Minimum experiment load

The A attachment load capacity: 2300 lbs.

The C attachment load capacity: 2800 lbs

For Type A attachment testing, the total test load, including a 1.15 MVF, is calculated as follows, 1.15 x 2300 = 2645lbs

The test load for Type C attachments can be calculated as 1.15 x 2,800 lbs = 3,220 lbs.

Force (Fi): 2800 lbs = 1270 kg (each joint) = 12460 N

Testing load (F) = 12460 x 1.15 = 14330 N.

Appendix A2 CFRP tube strength

Force (F) = 14330 N.

CFRP tube outer diameter (do) = 30 mm.

CFRP tube inner diameter (di) = 20 mm.

Tube side area: $Ac = 0.25\pi(do2 - di2)$

$= 0.25\pi (0.032 - 0.022) = 3.9 \times 10^{-4}\ m^2$

Tensile stress: $б_{cfrp} = F/Ac = 14330 / 3.9 \times 10^{-4} = 36.5$ MPa.

Shear stress: $\tau_{cfrp} = F/Ac = 14330 / 3.9 \times 10^{-4} = 36.5$ MPa.

Appendix A3 Bolt selection

M8 eyebolt breaking load: 1800 kg

FOS for M8 bolt = M8 breaking load / Minimum required load = 1800 / 1461 = 1.23

Minimum required load = F = 14330 N.

Bolt length: L = 106 mm = 0.106 m.

Load =F / g = 14330 / 9.81 = 1460 kg.

M10 eyebolt breaking load: 2400 kg.

The breaking load of the structure is higher than the load required.

2400 kg > 1460 kg.

FOS = 2400 / 1460 = 1.64

Tensile strength of the bolt = 500MPa.

Cross-section area of the M10 bolts = A_{M10} = 58 mm^2

Tensile stress = F / A_{M10} = 14330 / 58 = 247 MPa < 500 MPa.

Deformation: d_{M10} = (PL)/(AE) = (14330 x 0.106) / (5.8 x 10^{-5} x 190 x 10^9) = 0.138 mm

Appendix A4 Bolt hole ASME B18.2.8.

Metric Clearance Holes Chart									
Nominal Screw Size	Fit Class - Normal			Fit Class - Close			Fit Class - Loose		
	Nominal Drill Size	Hole Diameter		Nominal Drill Size	Hole Diameter		Nominal Drill Size	Hole Diameter	
		Min.	Max.		Min.	Max.		Min.	Max.
M1.6	1.8	1.8	1.94	1.7	1.7	1.8	2	2	2.25
M2	2.4	2.4	2.54	2.2	2.2	2.3	2.6	2.6	2.85
M2.5	2.9	2.9	3.04	2.7	2.7	2.8	3.1	3.1	3.4
M3	3.4	3.4	3.58	3.2	3.2	3.32	3.6	3.6	3.9
M4	4.5	4.5	4.68	4.3	4.3	4.42	4.8	4.8	5.1
M5	5.5	5.5	5.68	5.3	5.3	5.42	5.8	5.8	6.1
M6	6.6	6.6	6.82	6.4	6.4	6.55	7	7	7.36
M8	9	9	9.22	8.4	8.4	8.55	10	10	10.36
M10	11	11	11.27	10.5	10.5	10.68	12	12	12.43

Nominal Screw Size	Fit Class - Normal			Fit Class - Close			Fit Class - Loose		
	Nominal Drill Size	Hole Diameter		Nominal Drill Size	Hole Diameter		Nominal Drill Size	Hole Diameter	
		Min.	Max.		Min.	Max.		Min.	Max.
M12	13.5	13.5	13.77	13	13	13.18	14.5	14.5	14.93
M14	15.5	15.5	15.77	15	15	15.18	16.5	16.5	16.93
M16	17.5	17.5	17.77	17	17	17.18	18.5	18.5	19.02
M20	22	22	22.33	21	21	21.21	24	24	24.52
M24	26	26	26.33	25	25	25.21	28	28	28.52
M30	33	33	33.39	31	31	31.25	35	35	35.62
M36	39	39	39.39	37	37	37.25	42	42	42.62
M42	45	45	45.39	43	43	43.25	48	48	48.62
M48	52	52	52.46	50	50	50.25	56	56	56.74

Appendix A5 Aluminium joints calculations

Force (F) = 14330 N.

M10 washer outer diameter (do_{M10}) = 21 mm.

M10 washer inner diameter (di_{M10}) = 10 mm.

L_{Al} = 60 mm.

Tube side area: $Ac_{Al} = 0.25\pi(do_{M10}^2 – di_{M10}^2)$

$= 0.25\pi (0.021 – 0.01) = 267.82\ mm^2$

Tensile stress: $б_{Al} = F / Ac_{Al} = 14330 / 3.9 \times 10^{-4} = 53.5$ MPa.

Shearing area of the aluminium joints (AS_{Al}) = 7920 mm^2 ($7.92 \times 10^{-3}\ m^2$)

Shear stress: $\tau_{Al} = F / As_{Al} = 14330 / 7.92 \times 10^{-3} = 1.8$ MPa.

Deformation: $d_{Al} = (FL_{Al})/(AE) = (14330 \times 0.06) / (2.6782 \times 10\text{-}4 \times 75.6 \times 103) = 0.0424$ mm

Appendix A6 CFRP tubes deformation

Force (F) = 14330 N.

CFRP tube outer diameter (do) = 30 mm

CFRP tube inner diameter (di) = 20 mm

$I = (\pi/64) \times (do^2 - di^2) = 3191 \times 10^{-8}$

E = 86 GPa

Tube side area: $Ac = 0.25\pi(do^2 - di^2)$

$= 0.25\pi\ (0.03^2 - 0.02^2) = 3.9 \times 10^{-4}\ m^2$

Load applied to the long CFRP tube = F2 = 149 N

Load applied to the short CFRP tubes = F1 = (F – F2) / 3 = 4727 N

L1 = 307 mm.

L2 = 307 mm.

Long CFRP tube deformation = $F2 \times (L1^3) / (3 \times E \times I) = 0.524$ mm

Short CFRP tube deformation = $F1 \times (L2^3) / (3 \times E \times I) = 0.524$ mm

Appendix A7 steel adopter plates

The base plate thread length for M12 screws: $l = 1.5d = 1.5 \times 12 = 18$ mm

Appendix A8 Strain gauge resistance

The equivalence resistance of the 3300 Ohms and 390 Ohms surface mount resistance

$R_{eq} = (R1 \times R2) / (R1 + R2) = (3300 \times 390) / (3300 + 390) = 348.78$ Ohms

Reference

Alner, D. J. (Ed.). (1965). Aspects of adhesion (Vol. 6). University of London Press.

American National Standards Institute. (2017). Clearance Holes for Bolts, Screws, and Studs. American Society of Mechanical Engineers.

A.R. Abdullah, M. Afendi, M.S. Abdul Majid. (2013). Effect of adhesive thickness on adhesively bonded T-joint. IOP Conference Series Materials Science and Engineering.

Arenas, J. M., Narbón, J. J., & Alía, C. (2010). Optimum adhesive thickness in structural adhesives joints using statistical techniques based on Weibull distribution. International Journal of Adhesion and Adhesives, 30(3), 160-165.

Balle, F., Huxhold, S., Wagner, G., & Eifler, D. (2011). Damage monitoring of ultrasonically welded aluminum/CFRP-joints by electrical resistance measurements. Procedia Engineering, 10, 433-438.

Beer, F. P., Johnston, E. R., DeWolf, J. T., & Mazurek, D. F. (2015). Mechanics of materials. New York.

B.Mikhail. (2009). Adhesive Bonding: Materials, Applications and Technology Wiley-VCH Verlag GmbH & Company KgaA.

Bolton, W. C. (2015). *Mechatronics: Electronic Control Systems in Mechanical and Electrical Engineering*. Pearson UK.

Boyd, S. W., Blake, J. I. R., Shenoi, R. A., & Kapadia, A. (2004). Integrity of hybrid steel-to-composite joints for marine application. Proceedings of the Institution of

Mechanical Engineers, Part M: Journal of Engineering for the Maritime Environment, 218(4), 235-246.

Brandtner-Hafner, M. H. (2019). Fracture analysis of structural adhesives: introducing a new benchmark for adhesive performance. In *Proceedings: 5th International Conference on Structural Adhesive Bonding, Porto* (pp. 52-70).

Carlberger, T., & Stigh, U. (2010). Influence of layer thickness on cohesive properties of an epoxy-based adhesive—an experimental study. The Journal of Adhesion, 86(8), 816-835.

Callister, W. D., & Rethwisch, D. G. (2018). Materials science and engineering: an introduction (Vol. 9). New York: Wiley.

Davis, Joseph R. (2004). Tensile testing (2nd ed.). ASM International. ISBN 978-0-87170-806-9.

David Schnerch, Mina Dawood, Dr Sami Rizkalla (June 2007), STRENGTHENING OF STEEL CONCRETE COMPOSITE BRIDGES WITH HIGH MODULUS CARBON FIBER REINFORCED POLYMER (CFRP) STRPS, Constructed Facilities Laboratory, Department of Civil, Construction, and Environmental Engineering.

Dawei, Z., Qi, Z., Xiaoguang, F., & Shengdun, Z. (2018). Review on joining process of carbon fibre-reinforced polymer and metal: Methods and joining process. Rare Metal Materials and Engineering, 47(12), 3686-3696.

Ebnesajjad, S., & Landrock, A. H. (2014). *Adhesives technology handbook*. William Andrew.

Edward M. Petrie. (2007). Handbook of adhesives and sealants. McGraw-Hill, ISBN 0-07-147916-3.

Galvez, P., Quesada, A., Martinez, M. A., Abenojar, J., Boada, M. J. L., & Diaz, V. (2017). Study of the behaviour of adhesive joints of steel with CFRP for its application in bus structures. Composites Part B: Engineering, 129, 41-46.

Hsu, C. Y., Liang, C. C., Teng, T. L., & Nguyen, H. A. (2016). The dynamic responses of the submersible vehicle mast with different cross-sectional shapes subjected to underwater explosion. In MATEC Web of Conferences (Vol. 54, p. 11006). EDP Sciences.

Hsu Hnin Wai, Dr. Ehab Hamed. (2014). Simulation of Stress Distribution at a Single Lap-joint. International Journal of Adhesion and Adhesives.

Imanaka, M., Ishii, K., Hara, K., Ikeda, T., & Kouno, Y. (2018). Fatigue crack propagation rate of CFRP/aluminum adhesively bonded DCB joints with acrylic and epoxy adhesives. *International Journal of Adhesion and Adhesives*, *85*, 149-156.

Industrial Heating. (2002). Watch Out for Tensile-Testing Pitfalls. Industrial Heating. https://www.industrialheating.com/articles/84063-watch-out-for-tensile-testing-pitfalls

James Bakewell (2019). Creating strong bonds. Automotive Manufacturing Solutions, AMS.), 235-246.

Kalpakjian, S. (2001). Manufacturing engineering and technology. Pearson Education India.

Karuppasamy, Karthik Selva Kumar, P.S., Balaji. (2019). Applications and Techniques for Experimental Stress Analysis. IGI Global, ISBN 9781799816911.

Kahraman, R., Sunar, M., & Yilbas, B. (2008). Influence of adhesive thickness and filler content on the mechanical performance of aluminum single-lap joints bonded with aluminum powder filled epoxy adhesive. Journal of materials processing technology, 205(1-3), 183-189.

Khan, A. S., & Wang, X. (2001). *Strain measurements and stress analysis*.

Ling, S. J., Sanny, J., & Moebs, W. (2021). University Physics, Volume 1 (OpenStax).

Loutas, T., Adamos, L., Tsokanas, P., de la Escalera, F. M., & Essa, Y. (2019). FATIGUE FRACTURE BEHAVIOR OF DISSIMILAR METAL-COMPOSITE ADHESIVE JOINTS FOR AEROSPACE APPLICATIONS: AN EXPERIMENTAL STUDY. Laboratory of Applied Mechanics and Vibrations, Department of Mechanical Engineering and Aeronautics, University of Patras, Patras University Campus.

Maxime Beaufeu. (2019). Metal Composite Joints for Aerospace Applications. AUT.

M. H. Khan, O. A. Gali, A. Edrisy & A. R. Riahi. (2016). Effect of oxidation and surface roughness on the shear strength of single-lap-joint adhesively bonded metal specimens by tension loading

Mittal, K. L. (2012). Adhesive joints: Formation, characteristics, and testing. Springer Science & Business Media.

Nguyen, V. N., Nguyen, Q. M., Thao, H., Thi, D., & Huang, S. C. (2017). An Investigation of Dissimilar Welding Aluminum Alloys to Stainless Steel by the Tungsten Inert Gas (TIG) Welding Process. In Materials Science Forum (Vol. 904, pp. 19-23). Trans Tech Publications Ltd.

NI. (2020). Measuring Strain with Strain Gages. NATIONAL INSTRUMENTS CORP. https://www.ni.com/en-nz/innovations/white-papers/07/measuring-strain-with-strain-gages.html

Petrie, E. M. (2007). Handbook of adhesives and sealants. McGraw-Hill Education.

Pisharody, A. P., Blandford, B., Smith, D. E., & Jack, D. A. (2019). An experimental investigation on the effect of adhesive distribution on strength of bonded joints. Applied Adhesion Science, 7(1), 1-12.

Popwil. (n.d.). Large-scale Multi-function Dynamic-static Structure Testing System. opwil Instrument Co., Ltd. http://popwilglobal.com/case-studies/case-studies-structural_engineering_test_system/cases1-6/

R.F. Wegmanand, J. Van Twisk. (2012) Surface Preparation Techniques for Adhesive Bonding: Second Edition.

Sanders, R. E. (2001). Technology innovation in aluminum products. *JOM*, *53*(2), 21-25.

Schwartz, M. M. (1997). Composite materials. Volume 1: Properties, non-destructive testing, and repair.

Shukur A. Hassan (2018). The Potential of Biomimetics Design in the Development of Impact Resistant Material. Faculty of Mechanical Engineering, University Technology Malaysia.

Stout, M. B. (1960). Basic electrical measurements. Englewood Cliffs, NJ: Prentice-Hall.

Stephen F. Pollard. (1993). *Boatbuilding with Aluminum*.

Vishay Precision Group. (2014). Stress Analysis Strain Gages. Micro Measurement.

Wei, W., Rongjin, H., Chuanjun, H., Zhao, Y., Li, S., & Laifeng, L. (2015). Cryogenic performances of T700 and T800 carbon fibre-epoxy laminates. In IOP Conference Series: Materials Science and Engineering (Vol. 102, No. 1, p. 012016). IOP Publishing.

Window, A. L., & Holister, G. S. Strain gauge technology. (1982). Appl. Science Publishers, London.

Woizeschke, P., & Wottschel, V. (2013). Recent developments for laser beam joining of CFRP-aluminum structures. Procedia Materials Science, 2, 250-258.